Measurement of the Structure Function $F_2(x, Q^2)$ of the Proton at Low Q^2 with the H1 Detector at HERA Using the New Detector Components Spacal and BDC

DISSERTATION

zur Erlangung des Doktorgrades
des Fachbereichs Physik
der Universität Hamburg

vorgelegt von

Andreas Meyer

aus Bielefeld

Hamburg
1997

Gutachter der Dissertation :	Prof. Dr. Beate Naroska Prof. Dr. Ulrich Straumann
Gutachter der Disputation :	Prof. Dr. Beate Naroska Prof. Dr. Albrecht Wagner
Datum der Disputation :	10. Oktober 1997
Vorsitzender des Promotionsausschusses :	Prof. Dr. Bernhard Kramer

Abstract

A measurement of the structure function $F_2(x, Q^2)$ of the proton is presented in the kinematic range of Q^2 between 0.85 and 25 GeV^2 and Bjorken-x between $1.3 \cdot 10^{-5}$ and $5 \cdot 10^{-3}$. The measurement is performed using data recorded with the H1 detector at the ep storage ring HERA in 1995. In the winter shutdown 1994/95 the H1 detector was upgraded with a new calorimeter 'Spacal' and a new drift chamber 'BDC'. These components are used in this analysis for the first time. One of the main topics of this thesis is the energy calibration of the Spacal calorimeter. With the help of the new detector components the precision of the measurement of F_2 is improved compared to previous results by roughly a factor of 2 in the Q^2-range between 2.5 and 6.5 GeV^2.

Kurzfassung

Die Arbeit beschreibt eine Messung der Strukturfunktion F_2 des Protons im kinematischen Bereich von $0.85 \leq Q^2 \leq 25$ GeV^2 und $1.3 \cdot 10^{-5} \leq x \leq 5 \cdot 10^{-3}$. Die Messung beruht auf Daten, die im Betriebsjahr 1995 mit dem H1 Detektor am HERA Speicherring aufgenommen wurden. Im Winter 1994/95 waren ein neues Kalorimeter 'Spacal' und eine Driftkammer 'BDC' im H1 Detektor installiert worden. Diese Detektorkomponenten werden in dieser Arbeit erstmals verwendet. Ein Schwerpunkt dieser Arbeit liegt auf der Energiekalibration des Spacal Kalorimeters. Mithilfe der neuen Detektorkomponenten wird die Präzision der Messung von F_2 im Vergleich zu früheren Ergebnissen im Bereich von $2.5 \leq Q^2 \leq 6.5$ GeV^2 um einen Faktor 2 verbessert.

Contents

Abstract i

Introduction 1

1 Deep Inelastic Scattering 3
- 1.1 Event Kinematics . . . 4
- 1.2 Inclusive Cross Section and Structure Functions . . . 6
- 1.3 Outline of QCD . . . 7
- 1.4 Recent Results . . . 11
- 1.5 Objective of the Present Analysis . . . 14

2 The H1 Experiment at HERA 15
- 2.1 The ep Storage Ring HERA . . . 15
- 2.2 The H1 Detector . . . 16
- 2.3 The Backward Calorimeter Spacal . . . 22
  - 2.3.1 Spacal Detector Design . . . 23
  - 2.3.2 Spacal Electronics . . . 26
  - 2.3.3 The Inclusive Electron Trigger . . . 28
  - 2.3.4 Reconstruction of the Scattered Electron . . . 29
- 2.4 Reconstruction of the Event Kinematics . . . 30
- 2.5 Event and Detector Simulation . . . 33

3 Energy Calibration 36
- 3.1 The Kinematic Peak . . . 37
- 3.2 Relative Calibration of the Calorimeter Cells . . . 38
- 3.3 Calibration Procedure . . . 40
  - 3.3.1 Event Selection . . . 40
  - 3.3.2 Understanding the y_{JB} Distribution . . . 42
  - 3.3.3 Calibration Procedure and Results . . . 44
- 3.4 Double Angle Method . . . 50
- 3.5 Homogeneity and Linearity . . . 53
- 3.6 Energy Calibration of the Spacal for Hadrons . . . 55
- 3.7 Summary . . . 59

4 Data Selection **60**
4.1 Extraction Method of F_2 . . . 60
4.2 Outline of the Event Selection . . . 63
4.3 Run Selection . . . 64
4.4 DIS Trigger Selection . . . 65
4.4.1 Trigger Efficiencies . . . 66
4.4.2 Trigger Selection and Efficiency Correction . . . 68
4.5 Vertex Reconstruction . . . 68
4.5.1 Position of the Reconstructed Vertex . . . 69
4.5.2 Vertex Reconstruction Efficiency . . . 70
4.6 Event Selection Using the Spacal . . . 72
4.7 Measurement of the Electron Scattering Angle . . . 77
4.7.1 Electron Track Selection . . . 78
4.7.2 Resolution and Systematic Shift of the Electron Angle . . . 79
4.7.3 BDC Event Selection Criteria . . . 79
4.7.4 Investigation of the Measured Radial Dependence of Rate . . . 82
4.8 Photoproduction Background . . . 85
4.8.1 Tagged Electron Events . . . 86
4.8.2 Corrections to the PHOJET simulation . . . 89
4.8.3 Consistency Check with Rejected Events . . . 92
4.9 Radiative Corrections . . . 93
4.9.1 Outline of QED Radiation . . . 93
4.9.2 Investigation of QED Final State Radiation . . . 96
4.10 Kinematic Distributions . . . 98
4.11 Summary . . . 101

5 The Structure Function F_2 **102**
5.1 Defining the Analysis Bins . . . 102
5.2 Systematic Errors . . . 107
5.3 Results . . . 110
5.4 Comparison with Models . . . 115

Summary **122**

Bibliography **124**

Introduction

The scattering of leptons off nuclei, and later nucleons, has been for many decades one of the key measurements in the exploration of the structure of matter. As early as in the late sixties, measurements at SLAC led to the discovery of the spin-$\frac{1}{2}$ constituents of the proton which came to be identified as quarks. In the Quark Parton Model the sum of the momentum distributions of the quarks in the proton is directly related to the structure function F_2.

In the following years Quantum Chromodynamics (QCD) was developed as the field theory of strong interactions. In QCD the quarks interact via exchanged gauge bosons called gluons which, together with sea quarks, carry about half of the proton momentum. At sufficiently large momentum transfer, Q^2, the coupling between quarks and gluons is small, allowing the description of the scattering processes in perturbation theory. Perturbative QCD is able to describe the relative behavior of the parton momentum distributions under variations of Q^2 by virtue of evolution equations. Throughout the seventies and eighties the predictions of QCD have successfully been tested in a series of experiments continuously extending the kinematic range. Since, with increasing beam energy, the electron beams used in the early experiments at SLAC and Fermilab, became more and more difficult to produce, muon beams became a natural choice. Furthermore, neutrino nucleon scattering experiments have been pursued. Until 1992, data with excellent precision, covering a wide kinematic range down to values of Bjorken-$x \sim 10^{-4}$ and up to $Q^2 \sim 200$ GeV^2, have been produced in particular at SLAC (eN) and by the BCDMS, NMC and E665 (μN) as well as CCFR and CDHS (νN) Collaborations at CERN and at Fermilab. These data have been and continue to be the basis for deep insights into the structure of the proton and for improvements in the understanding of QCD.

The electron proton collider HERA at DESY, Hamburg, follows this long tradition of Deep Inelastic Scattering experiments. At HERA both, electrons and protons are accelerated and collide at a center of mass energy of 300 GeV allowing to resolve the structure of the proton down to distances of $\sim 10^{-18}$ m. Compared to former 'fixed target' experiments, where the nucleons probed by the leptons were at rest (in the laboratory frame) the center of mass energy is larger by more than one order of magnitude. HERA therefore provides a unique facility for the study of the structure of the proton in a new kinematic regime allowing measurements of the structure function down to values of Bjorken-$x \gtrsim 10^{-6}$ at values of $Q^2 \gtrsim 0.1$ GeV^2.

Experimentally, the structure function is extracted from the double differential ep cross section measured as a function of x and Q^2. At the two colliding beam experiments ZEUS and H1 not only the scattered lepton but also the hadronic final state is measured giving rise to alternative methods to reconstruct the event kinematics and to

control possible systematic effects. Being fully inclusive the measurement of F_2 makes use of the full event statistics and is thus least affected by statistical uncertainties. Furthermore, the results of the inclusive measurement can be interpreted in QCD without theoretical assumptions on the exact behavior of the hadronic final state. As early as in the first year of HERA operation, 1992, a significant rise of the structure function towards small values of x was discovered. The dynamical behavior of the data was found to be well described by the DGLAP evolution equations which are based on perturbative QCD. However, the discrimination of different theoretical models and the precise determination of the parton distributions requires high precision. In the small x regime at HERA in particular the distribution of gluons in the proton can be determined. The continuous increase of the HERA luminosity has reduced the statistical uncertainties. In order to gain further precision it is necessary to optimize the detector performance and to control and minimize the systematic uncertainties of the measurement.

In the winter shutdown 1994/95 the H1 detector was upgraded. The detector components which cover the region of small electron scattering angles ($\lesssim 25°$ relative to the electron beam) were replaced by a new lead / scintillating-fiber calorimeter of spaghetti-type 'Spacal' and a Backward Drift Chamber 'BDC'. The new components improve the detector performance in particular for events with $Q^2 \lesssim 100$ GeV^2 and extend the accessible[1] kinematic range to Q^2-values of ~ 0.85 GeV^2 and $x \sim 10^{-5}$. In addition to a better energy and angular resolution the main improvements lie in the possibility to measure the hadronic final state and in the suppression of beam background on the first trigger level with the help of an excellent time resolution.

For the measurement presented here data are used which were recorded with the H1 detector in 1995, the commissioning year of the Spacal and the BDC. In the context of this analysis the behavior of the new detector components is explored in detail for the first time.

This thesis is organized as follows: Chapter 1 provides an introduction to the theory of Deep Inelastic Scattering and QCD. The physics objective of the analysis is motivated by relating theoretical developments to recent experimental results. The experimental environment of the H1 Detector is covered in chapter 2. A description of the most crucial detector components and the data acquisition is given. Special focus is put on the technical features of the new Spacal Calorimeter. Chapter 3 contains a detailed description of the energy calibration of the Spacal. In chapter 4 the measurement of the structure function is described. Besides a detailed discussion of the event selection based on the identification of the scattered electron in the Spacal a main topic of this chapter is the determination of the photoproduction background. Furthermore, a first investigation of QED final state radiation is performed. Finally, in chapter 5, the result of the measurement is presented. The structure function F_2 and the total virtual photon proton cross section are compared to model predictions currently available to describe the HERA data in the small-Q^2-region.

[1] with data of nominal interaction point position.

Chapter 1

Deep Inelastic Scattering

Inclusive cross section measurements have proven extremely fruitful for the understanding of the structure of matter. The relation of experimental results to theoretical concepts is most direct in the case of inclusive measurements where only the scattered lepton is measured and all possible hadronic final state configurations are summed over. Historically, by the time of the sixties, measurements of elastic electron proton scattering had led to the determination of the nucleon form factors which in the non-relativistic limit describe the charge distributions and the magnetic moments of protons and neutrons.

The notion of 'Deep Inelastic Scattering' (DIS) was coined with the advent of high energy data recorded at the *Stanford Linear Accelerator Center* (SLAC), as of 1967, when events with a very large energy loss of the scattered electron were observed. The famous result of these data was that the deep inelastic structure function F_2 showed very little dependence on the transferred four-momentum squared, Q^2, between the electron and the target, but depended only on the variable x which in the parton model can be interpreted as the fractional momentum of the struck proton constituent. Such a scale invariant behavior, simply called 'scaling', had been predicted by Bjorken already in 1966 [1]. The simplest explanation for scaling was given by the parton model, assuming the proton constituents to be free and point-like partons. Almost immediately, in 1969, the 'Quark Parton Model' (QPM) was established identifying the partons with the spin-$\frac{1}{2}$ quarks [2]. In the Quark Parton Model the structure function F_2 is related to the sum of the parton momentum distributions $x \cdot q_i(x)$ weighted with the square of their electric charge e_i,

$$F_2(x) = \sum_i e_i^2 x q_i(x). \tag{1.1}$$

In the years to follow Quantum Chromodynamics (QCD) was developed as the field theory of strong interactions between quarks and gluons. QCD solves the conceptual puzzle of the partons which, on the one hand are permanently bound in the proton and, on the other hand behave like free particles, introducing a scale dependent ('running') coupling constant which is large at small Q^2 ('confinement') and logarithmically vanishes towards large Q^2 ('asymptotic freedom').

Until the late eighties various fixed target experiments were performed at center of mass energies up to 30 GeV providing a wealth of data by which the structure of the proton could be constrained very precisely for values of $x \gtrsim 10^{-3}$ and $Q^2 \lesssim 200$ GeV^2.

At the ep storage ring HERA the center of mass energy is increased by one order of magnitude to a value of ~ 300 GeV. An entirely new kinematic regime of Deep Inelastic Scattering is thus opened up, extending down to values of $x \gtrsim 10^{-6}$ and Q^2 values of up to 90000 GeV^2. At HERA, besides the scattered electron, the hadronic final state is also measured allowing the use of different independent methods to reconstruct the event kinematics. The HERA research program also covers detailed studies of the properties of the hadronic final state. A concise review of HERA physics can be found in [3].

In this chapter the variables describing the event kinematics of inclusive deep inelastic scattering processes are explained (section 1.1) and the relations between the measured double differential ep cross section and the structure functions are defined (section 1.2). A brief outline of the interpretation of the structure function F_2 in the framework of QCD is given (section 1.3). The present theoretical understanding of ep scattering is confronted with recent experimental results in section 1.4. In this context, the objective of the presented measurement is discussed (section 1.5).

1.1 Event Kinematics

The process of inclusive electron proton scattering, $ep \to lX$ is visualized in fig.1.1(a). The interaction between the electron and the proton, to lowest order in the single boson exchange approximation, takes place via an exchanged gauge boson. The exchanged boson carries the four-momentum q, and p stands for the four-momentum of the incoming proton. The four-momenta of the incoming and the scattered lepton are denoted by k and k', respectively. The system X with the four-momentum p' represents the hadronic final state, i.e. the particles produced in the break-up of the proton.

A distinction is made between two classes of events, namely Neutral Current (NC) events, $e^{\pm}p \to e^{\pm}X$, with a neutral virtual photon or Z^0 exchange; and Charged Current (CC) reactions, $e^{\pm}p \to \overset{(-)}{\nu} X$, with a $W^{\pm}$ exchange and a neutrino as outgoing lepton.

At fixed beam energy the event kinematics is unambiguously defined by two of the three Lorentz invariant variables,

$$Q^2 = -q^2 = -(k - k')^2 \tag{1.2}$$

$$x = \frac{Q^2}{2p \cdot q} \tag{1.3}$$

$$y = \frac{p \cdot q}{p \cdot k} \tag{1.4}$$

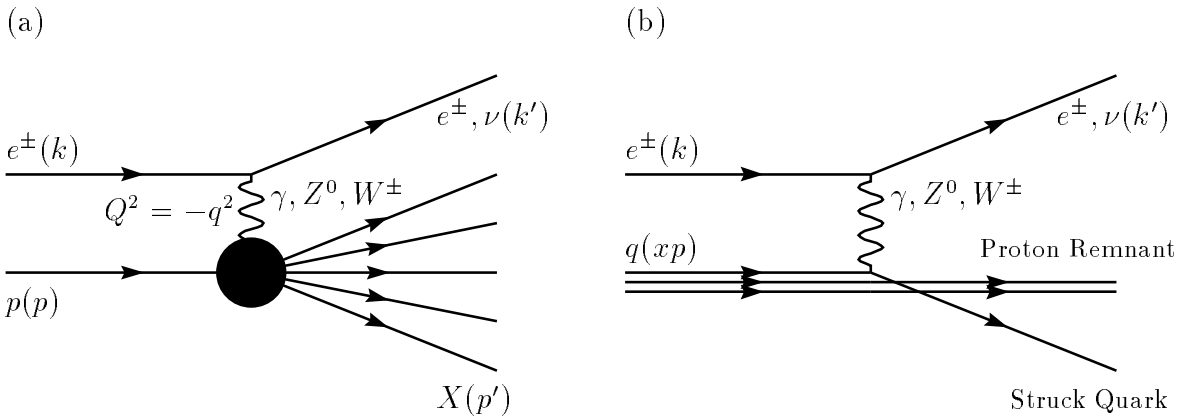

Figure 1.1: (a) Schematic representation of inclusive electron proton scattering $ep \to lX$ in the single boson exchange approximation. The four-momenta of the incoming and scattered lepton are k and k', respectively. The incident proton four-momentum is p; p' denotes the four-momentum of the hadronic final state X. The exchanged boson carries the four-momentum q. (b) Representation of ep scattering in the Quark Parton Model. Here the virtual photon interacts with a free pointlike (quark-)parton and the remaining partons ('spectators') do not undergo any interaction. In the infinite momentum frame the incident momentum of the 'Struck Quark' is given by xp.

Q^2, x and y offer the following suggestive interpretations: Q^2 denotes the negative four-momentum squared of the exchanged boson, i.e. its virtuality. In the limit of $Q^2 = 0$ the exchanged photon is called real and its life time becomes large. At a given Q^2 the distance d resolved at fixed x can be estimated following the Heisenberg uncertainty relation $d \cdot |\vec{q}| \sim 1$ yielding $d \sim 2M_p x/Q^2$. Thus, with increasing Q^2 the virtual boson probes smaller and smaller distances d within the proton. For the maximum Q^2 kinematically possible at HERA a value of $\sim 10^{-18}$ m is obtained. In the infinite momentum frame, i.e. in a frame where the incident proton energy is very large compared to the proton mass M_p, x is interpreted as the fraction of proton momentum carried by the struck quark (see fig. 1.1(b)). y gives the fraction of the incident electron energy transferred from the electron to the proton in the proton rest frame, i.e the fractional electron energy carried by the virtual photon. Since the transferred energy is absorbed in the final state of the proton, y quantifies the inelasticity of the event.

It is convenient to define two further quantities:

$$s = (k+p)^2 \tag{1.5}$$

$$W^2 = (q+p)^2. \tag{1.6}$$

s denotes the square of the ep center of mass energy. W gives the center of mass energy of the photon proton system which is equal to the invariant mass of the hadronic final state. At the HERA beam energies, $E_e = 27.5$ GeV for electrons and $E_p = 820$ GeV for protons, the masses of the incident particles can be neglected, yielding the following

relations:

$$s = 4 \cdot E_e \cdot E_p \tag{1.7}$$

$$W^2 = \frac{1-x}{x} \cdot Q^2. \tag{1.8}$$

In this approximation the kinematic variables x, y and Q^2 are related via the center of mass energy s:

$$Q^2 = sxy. \tag{1.9}$$

1.2 Inclusive Cross Section and Structure Functions

The cross section of the NC process $ep \to eX$ is written as

$$\sigma \propto L_{\mu\nu} W^{\mu\nu}. \tag{1.10}$$

In this equation the leptonic tensor $L_{\mu\nu}$ describes the interaction between the electron and the exchanged virtual boson. The hadronic tensor $W_{\mu\nu}$ accounts for the scattering of the exchanged boson with the proton. For single photon exchange $L_{\mu\nu}$ is precisely calculable in QED, $W_{\mu\nu}$ is unknown because it contains the internal structure of the proton which is as yet not calculable and must therefore be determined from experiments.

Using Lorentz invariance and current conservation one can, reduce $W_{\mu\nu}$ into three structure functions $F_i(x, Q^2)$, obtaining

$$\frac{\mathrm{d}^2\sigma^{e^\pm p}}{\mathrm{d}x\mathrm{d}Q^2} = \frac{4\pi\alpha^2}{xQ^4}\left[y^2 x F_1(x,Q^2) + (1-y)F_2(x,Q^2) \mp (y - \frac{y^2}{2})xF_3(x,Q^2)\right]. \tag{1.11}$$

A detailed derivation of this formula can be found in [4]. The term xF_3 describes the parity violating contribution from Z^0 exchange and interference terms between γ and Z^0 exchange. It is negligible at low and moderate Q^2 due to the large mass of the Z^0 ($M^2_{Z^0} \sim 10^4$ GeV^2) and becomes measurably large at large values of Q^2. At $Q^2 \lesssim 100$ GeV^2 the contribution is smaller than 0.1%. Consequently, neglecting the term xF_3 for low and moderate Q^2, the equation (1.11) can be reformulated as

$$\frac{\mathrm{d}^2\sigma^{e^\pm p}}{\mathrm{d}x\mathrm{d}Q^2} = \frac{2\pi\alpha^2}{xQ^4}\left[(2(1-y)+y^2)F_2(x,Q^2) - y^2 F_L(x,Q^2)\right] \tag{1.12}$$

$$\text{where} \qquad F_L = F_2 - 2xF_1. \tag{1.13}$$

This expression is called Born cross section.

The ep scattering processes can be viewed as interaction of a flux of virtual photons with the proton[1]. Virtual photons, having an effective mass, may have transverse

[1]The concept of a virtual photon flux is suggestive in particular at small x ($x \ll 10^{-2}$) where the life time, $t = 1/(2M_p x)$, of the exchanged virtual photon in the proton rest frame is large compared to the interaction time with the proton [3].

as well as longitudinal polarization. The double differential ep cross section can be decomposed accordingly,

$$\frac{\mathrm{d}^2\sigma^{e^\pm p}}{\mathrm{d}x\mathrm{d}Q^2} = \Gamma(y)\left(\sigma_T(x,Q^2)+\epsilon(y)\sigma_L(x,Q^2)\right) \quad (1.14)$$

$$= \Gamma(y)\sigma^{\mathrm{eff}}_{\gamma^* p}(x,y,Q^2) \quad (1.15)$$

where $\Gamma(y) = \frac{\alpha(2-2y+y^2)}{2\pi Q^2 x}$ describes the photon flux[2] and $\epsilon(y) = \frac{2(1-y)}{2-2y+y^2}$ is the photon polarization.

σ_T and σ_L respectively correspond to the cross sections of transversely and longitudinally polarized photons with the proton. They add to the total virtual photon cross section

$$\sigma^{\mathrm{tot}}_{\gamma^* p} = \sigma_T + \sigma_L. \quad (1.16)$$

At small x, in the HERA regime, σ_T and σ_L are related to the structure functions as

$$\sigma_T + \sigma_L = \frac{4\pi^2\alpha}{Q^2}F_2 \quad (1.17)$$

$$\sigma_L = \frac{4\pi^2\alpha}{Q^2}F_L. \quad (1.18)$$

The ratio R of σ_L and σ_T is defined as

$$R = \frac{\sigma_L}{\sigma_T} = \frac{F_L}{F_2 - F_L}. \quad (1.19)$$

Due to its relation to longitudinally polarized photons, given in equation (1.18), F_L is called Longitudinal Structure Function. Equation (1.12) shows that the sensitivity of the cross section on F_L is kinematically suppressed with y^2. At low $y \lesssim 0.4$ the effect of F_L on the extracted value of F_2 is therefore negligible ($\lesssim$ 2%).

1.3 Outline of QCD

Quantum Chromodynamics (QCD) is the field theory of the strong interactions between quarks and gluons. A detailed discussion of QCD can be found in [6]. In QCD each quark can appear in three different states called colors (red, green, blue). The strong interaction between quarks is mediated by gluons which carry both a color and an anticolor at the same time. Due to this property gluons are able to couple to gluons (self-coupling). This is in contrast to QED where photon self-coupling does not occur.

[2] It should be emphasized that the definition of a virtual photon flux is somewhat arbitrary since the definition is only constrained in the photoproduction limit ($Q^2 \to 0$) in which the real photon flux must be described, i.e. $\lim_{Q^2\to 0}\sigma^{\mathrm{tot}}_{\gamma^* p}(Q^2,W^2) = \sigma^{\mathrm{tot}}_{\gamma p}(W^2)$ must be satisfied. In this thesis the so-called Hand convention [5] is used.

In QED, due to screening effects from vacuum polarizations, the coupling constant α increases slowly with increasing Q^2. In QCD the self coupling of gluons works in the opposite direction producing antiscreening which leads to a logarithmic decrease of $\alpha_S(Q^2)$ with increasing Q^2 called 'running of $\alpha_S(Q^2)$'. The behavior of α_S is described by the renormalization group equation and the QCD β-function

$$\mu\frac{\delta\alpha_S(\mu)}{\delta\mu} = \alpha_s \cdot \beta(\alpha_S) = -\frac{\beta_0}{2\pi}\alpha_S^2 - \frac{\beta_1}{4\pi^2}\alpha_S^3 - \frac{\beta_2}{64\pi^3}\alpha_S^4 - ... \tag{1.20}$$

$$\text{with} \quad \beta_0 = 11 - \frac{2}{3}N_f; \quad \beta_1 = 51 - \frac{19}{3}N_f; \quad \beta_2 = 2857 - \frac{5033}{9}N_f + \frac{325}{27}N_f^2.$$

N_f is the number of quark flavors with mass less than the energy scale μ. A solution to equation (1.20) is given as an expansion in inverse powers of $\ln(Q^2)$ as

$$\alpha_S(Q^2) = \frac{4\pi}{\beta_0 \ln\frac{Q^2}{\Lambda^2}} \times \left[1 + \text{terms of higher order in } \ln(\mathrm{Q}^2/\Lambda^2)\right]. \tag{1.21}$$

Λ defines the strength of the coupling and must be determined experimentally. It is of the order[3] of 200 MeV [7]. Equation (1.21) is valid where Q^2 is large compared to Λ^2. It accommodates the running properties of α_S with Q^2 between the region of asymptotic freedom $\alpha_S \to 0$ as $Q^2 \to \infty$ and confinement where α_S is large and the partons are tightly bound in the proton.

The QCD factorization theorem states that the interaction can be split into two independent regions, a perturbative ('short distance') part with sufficiently large momentum scale and a non-perturbative ('long distance') part. In the perturbative part the relative smallness of $\alpha_S(Q^2)$ allows the expansion of solutions of QCD in a perturbation series of powers of $\alpha_S(Q^2)$. The non-perturbative part can in general only be determined experimentally. Formally, factorization means that the structure function F_2 can be expressed as a convolution of a coefficient function C_2^i calculable in QCD and the parton distribution functions f_i which are specific to the probed hadron but universal as regards the probing particle,

$$F_2(x,Q^2) \propto \sum_{f_i=q,\bar{q},g} \int_x^1 dy\ C_2^i\left(\frac{x}{y}, \frac{Q^2}{\mu^2}, \frac{\mu_F^2}{\mu^2}, \alpha_S(\mu^2)\right) f_i(y,\mu_F,\mu). \tag{1.22}$$

The factorization scale parameter μ_F defines the boundary between the perturbative and non-perturbative regions and μ is the renormalization scale parameter used to absorb divergent parts of the perturbation series.
In a physical interpretation factorization means that the structure function F_2 is composed of two contributions, namely a probability density $f_i(y)$ of finding a parton with fractional proton momentum y in the proton and a coefficient term $C_2^i(\frac{x}{y})$ [8]. $C_2^i(\frac{x}{y})$ describes how a parton with fractional momentum x evolves from radiative processes

[3]The exact measured value depends on the renormalization scheme, i.e. the chosen convention.

off the initial parton and subsequently interacts with the exchanged virtual boson. Since the longitudinal momentum of the radiated parton is always smaller or equal to that of the parent parton, the integration in equation (1.22) is restricted to the interval $x \leq y \leq 1$. In this picture F_2 at a given value of x can be viewed as receiving contributions from all partons with a fractional momentum $y \geq x$ in the proton.

Since F_2 is a measurable quantity it should be independent of scale parameters. This means that the parton distribution functions f_i must depend on the choice of μ_F and μ, i.e. the choice of the renormalization scheme. A frequently used scheme is the DIS scheme which is defined by the Quark Parton Model relation between F_2 and the parton momentum distributions $f_i(x)$, given in equation (1.1),

$$F_2(x) = \sum_{i=q,\bar{q}} e_i^2 x f_i(x), \tag{1.23}$$

is satisfied to all orders, i.e. $C_2^{\mathrm{DIS}}(x) = e_i^2 \delta(1-x)$. The DIS scheme can be understood as defining perfect freedom of the partons in the proton as conceptualized in the Quark Parton Model. In this scheme all higher order processes are absorbed in the long range parton distribution functions constituting the structure of the proton. Another scheme, more useful for theoretical calculations, is the $\overline{MS}$ scheme where the above equation holds to leading order (LO) only. In NLO in the $\overline{MS}$ scheme, F_2 is also directly connected with the distribution of gluons in the proton.

The change of the parton distributions as a function of Q^2, i.e. their dynamical behavior or evolution, is described by the DGLAP evolution equations[4][9, 10] given in leading order as:

$$\begin{aligned}
\frac{\mathrm{d}q_i(x,Q^2)}{\mathrm{d}\ln Q^2} &= \frac{\alpha_S(Q^2)}{2\pi}\int_x^1 \frac{\mathrm{d}y}{y}\left[\sum_j q_j(y,Q^2)P_{ij}^{(0)}\left(\frac{x}{y}\right) + g(y,Q^2)P_{ig}^{(0)}\left(\frac{x}{y}\right)\right] \qquad (1.24)\\
\frac{\mathrm{d}g(x,Q^2)}{\mathrm{d}\ln Q^2} &= \frac{\alpha_S(Q^2)}{2\pi}\int_x^1 \frac{\mathrm{d}y}{y}\left[\sum_j q_j(y,Q^2)P_{gj}^{(0)}\left(\frac{x}{y}\right) + g(y,Q^2)P_{gg}^{(0)}\left(\frac{x}{y}\right)\right].
\end{aligned}$$

The splitting functions $P_{ij}(x/y)$ give the probability that a parton j with fractional proton momentum y radiates a parton i with fractional parton momentum x/y. The integration is restricted to $x \leq y \leq 1$ for the same reason as in equation (1.22). The splitting functions are calculable by perturbative expansion,

$$P_{ij}(z,\alpha_S(Q^2)) = \frac{\alpha_S}{2\pi}P_{ij}^{(0)}(z) + \left(\frac{\alpha_S}{2\pi}\right)^2 P_{ij}^{(1)}(z) + \ldots \tag{1.25}$$

In leading order the splitting functions read:

$$P_{qq}^{(0)}(z) = \frac{4}{3}\left[\frac{1+z^2}{1-z}\right]_+ + 2\delta(1-z) \tag{1.26}$$

[4]DGLAP stands for Dokshitzer, Gribov, Lipatov, Altarelli, Parisi.

$$
\begin{aligned}
P_{qg}^{(0)}(z) &= \frac{1}{2}\left[z^2 + (1-z)^2\right] \\
P_{gq}^{(0)}(z) &= \frac{4}{3}\frac{1+(1-z)^2}{z} \\
P_{gg}^{(0)}(z) &= 6\left[\left(\frac{z}{1-z}\right)_+ + \frac{1-z}{z} + z(1-z) + \frac{11}{12}\delta(1-z)\right] - \frac{N_f}{3}\delta(1-z).
\end{aligned}
$$

Here the definition $\int_0^1 dx \frac{f(x)}{(1-x)_+} = \int_0^1 dx \frac{f(x)-f(1)}{(1-x)}$ is used [7]. To date the splitting functions have been calculated to next to leading order (NLO) [4].

The formal derivation of the DGLAP equations involves the Leading Log Approximation (LLA) where terms of the form $\alpha_S^n \cdot (\ln Q^2)^n$ are summed to all orders. These terms are leading because Q^2 is large by construction of the perturbative ansatz. It has been shown [11] that the LLA summation is equivalent to a sum of gluon ladder diagrams with decreasing fractional proton momentum x and strongly ordered transverse momentum,

$$x < x_n < ... < x_0 \tag{1.27}$$

$$Q^2 \gg k_{T,n}^2 \gg ... \gg k_{T,0}^2. \tag{1.28}$$

In the DGLAP approach x must be sufficiently large to ensure that terms of the type $\ln(1/x)$ of the splitting functions remain negligible. At low x it seems appropriate to include leading powers of $\ln(1/x)$ when accompanied by leading $\ln Q^2$ terms. This approach is called double leading logarithmic approximation (DLLA). The summation of $\ln(1/x)$ terms independent of Q^2 and at fixed $\alpha_S(Q^2)$ has been developed by BFKL[5] [12]. In leading order BFKL predict a behavior of F_2 proportional to $x^{-\lambda}$ with $\lambda \approx 0.5$. NLO calculations are still being pursued. In the limit of $s \to \infty$, i.e. $x \to 0$, a power behavior can not persist physically since the cross section must rise slower than $\ln^2 s$ (Froissart bound [13]).

Theory leaves as yet a number of questions to be answered by the experiments. Here, only the aspects most relevant to the present analysis are mentioned: The double differential ep cross section and the structure function $F_2(x, Q^2)$ is presently not calculable but can only be determined experimentally. Once the cross section is known as a function of x and Q^2 in a given kinematic region the evolution equations can be used for predictions of the cross section dependence outside the measured region. Furthermore, the experimental results can be used to extract the parton distribution functions f_i which describe the structure of the proton as a function of x and Q^2. High precision F_2 data at HERA provide a means of determining in particular the gluon density $g(x, Q^2)$ and the strong coupling constant $\alpha_S(Q^2)$ [14]. As described above, towards low x and low Q^2 the perturbative approach will reach its limit of applicability and non-perturbative effects start to dominate. To date this region of transition, in particular in the low-x regime, has not yet been explored in detail.

[5] BFKL stands for Balitski, Fadin, Kuraev and Lipatov.

1.4 Recent Results

Measurements of F_2 using the HERA data recorded in 1994 [15, 16] showed that the next to leading order (NLO) DGLAP equations describe the data in the wide range from $Q^2 = 5000$ GeV^2 down to the lowest measured values of $Q^2 = 1.5$ GeV^2 within the achieved level of precision. This is illustrated in fig. 1.2 where data from HERA (here the H1 Experiment [15]) are presented together with results from earlier fixed target experiments [17, 18]. F_2 is shown as a function of x in different bins of Q^2. A strong rise of F_2 is seen towards the lowest values of x in all bins of Q^2. The solid line shows the result of the global H1 QCD fit [15, 19] based on the DGLAP evolution equation. QCD fits are performed parametrizing the parton distributions as functions of x at a given starting scale Q_0^2. The parameters are fit to the data such that the DGLAP equations and a set of additional constraints (e.g. QCD momentum sum rules) are obeyed. In the H1 fit [15] the data from H1 and from fixed target experiments are combined in order to achieve maximum possible precision.

The same results are presented in fig. 1.3 showing the total virtual photon proton cross section $\sigma^{\rm tot}_{\gamma^* p}$ as a function of W^2 in bins of Q^2. The strong rise of F_2 towards low x is reflected here in the increase of the cross section with W^2. Note that at low x the relation $W^2 = Q^2/x$ holds (see equation (1.8)). The perturbative model by Glück, Reya and Vogt (GRV) [20], based on the NLO DGLAP evolution equation, succeeds in describing the behavior for all values of $Q^2 \geq 1.5$ GeV^2 (see also section 5.4).

In addition to the previous figure the plot contains the total cross section $\sigma^{\rm tot}_{\gamma p}$ of photoproduction events at $Q^2 = 0$. In this region perturbation theory is not applicable. The line through the data points at $Q^2 = 0$ represents a phenomenological model by Donnachie and Landshoff (DOLA) [21] following a Regge theory type ansatz. An introduction to Regge theory can be found in [22]. DOLA parametrize the energy dependence of the cross section as

$$\sigma^{\rm tot}(W^2) = A \cdot W^{2\epsilon} + B \cdot W^{2\lambda}. \tag{1.29}$$

They predict $\epsilon = -0.4524$ and $\lambda = 0.0808$ from a fit to experimental data of hadron-hadron collisions. It turns out that the γp cross section measured at HERA [23, 24] obeys the same description[6]. At high energies W the 'pomeron' term $B \cdot W^{2\lambda}$ dominates and describes the slow increase of the total photoproduction cross section with the center of mass energy (see also section 5.4).

It is obvious from fig. 1.3 that the energy dependence of the photoproduction data and the data at $Q^2 \geq 1.5$ GeV^2 (DIS) is strikingly different. A measurement of the slope of the ep DIS cross section as $W^{2\lambda}$ at fixed Q^2 yields values of $\lambda \sim 0.2...0.4$ continuously rising towards larger Q^2 [15] in contrast to ~ 0.08 in the case of the photoproduction data with $Q^2 = 0$.

[6] The fact that the energy dependences of hadron-hadron and γp (as well as $\gamma\gamma$) cross sections follow the same exponential behavior is often referred to as 'pomeron universality'.

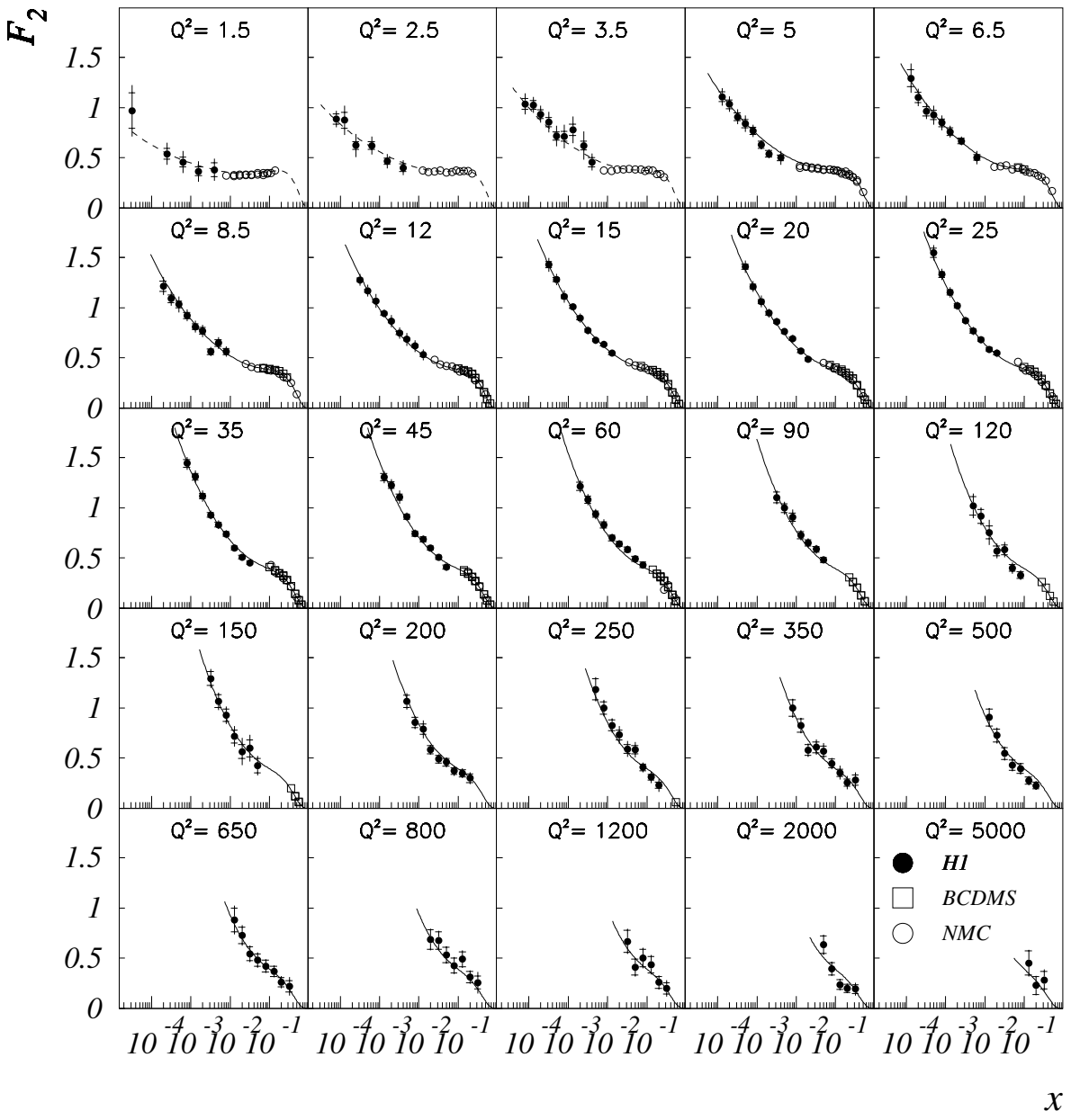

Figure 1.2: The structure function F_2 as a function of x in bins of Q^2. The results of the H1 Collaboration obtained from data recorded in 1994 [15] are shown by the full points. The fixed target experiments NMC [18] (BCDMS [17]) are represented by open points (squares), respectively. The curves show the results of a NLO QCD fit which includes data for $Q^2 \geq 5$ GeV^2. The dashed lines show the extrapolation of the fit to lower values of Q^2.

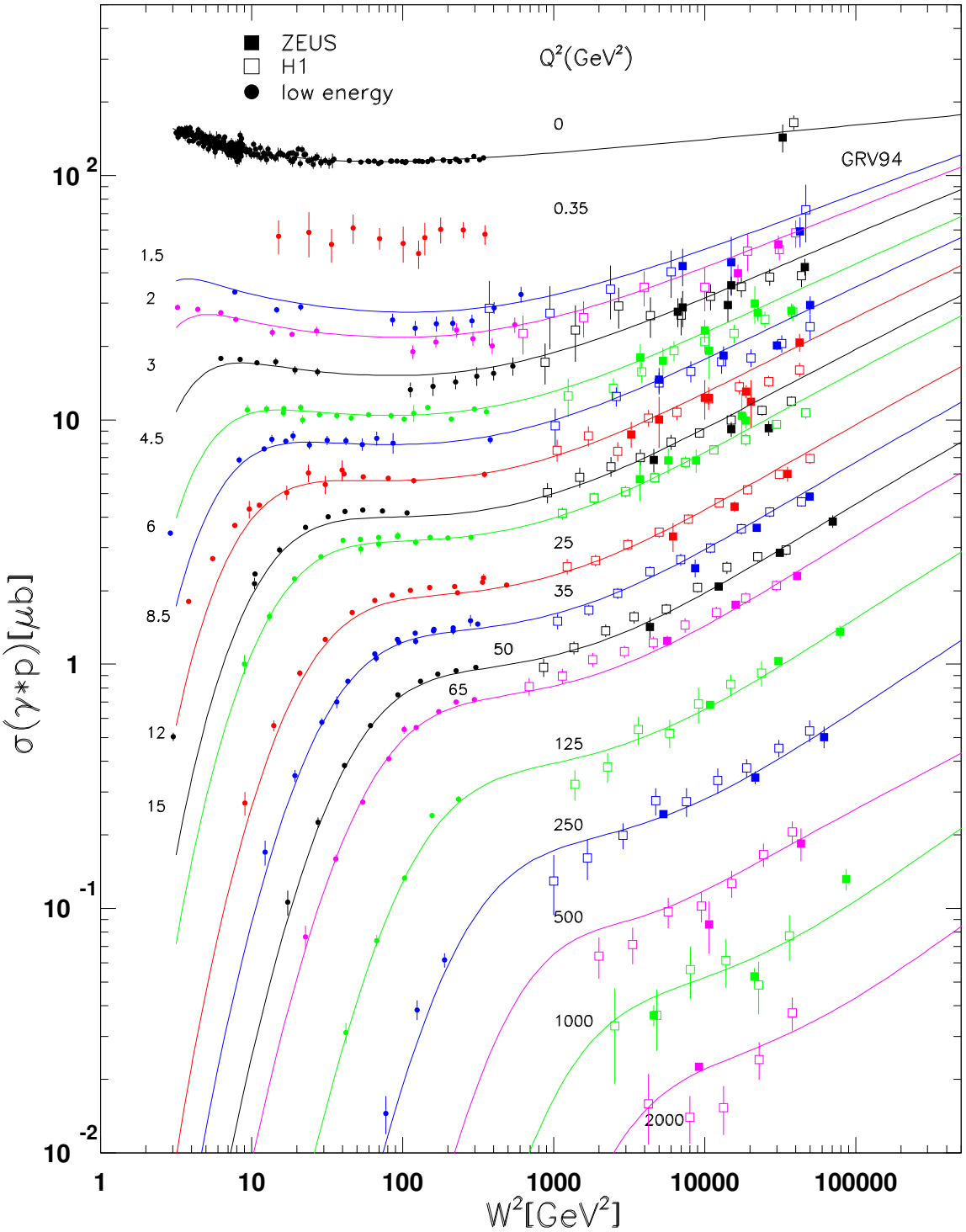

Figure 1.3: The total virtual photon proton cross section as a function of W^2 for different bins in Q^2. Open (full) squares denote results from the H1 (ZEUS) Collaboration [23, 24]. At $Q^2 \geq 1.5$ GeV^2 the curves describe the model by GRV [20]. At $Q^2 = 0$ results from total photoproduction cross section measurements are shown. The curve through these points represents the parametrization by DOLA [21].

How does the transition between DIS and photoproduction take place? How can phenomenological cross section models be related to perturbative QCD? These questions are subject of much theoretical debate at present. Various model predictions have been developed to predict the structure function in the region of small Q^2 and small x. A measurement of the structure function F_2 and the energy behavior of the cross section in the transition region at very low values of Q^2 may help to discriminate between the models and to give constraints for further theoretical developments.

1.5 Objective of the Present Analysis

In the winter shutdown 94/95 at the H1 Detector at HERA a substantial increase in the detector acceptance for smaller scattering angles, and hence for smaller values of Q^2, was achieved with the installation of the new detector components 'Spacal' and 'BDC' (see chapter 2).

In the commissioning year 1995 two data sets were recorded. In addition to a sample of data with standard ep beam positions ('nominal vertex data'), a run dedicated to the measurement of the transition region at low Q^2 was performed. Here, the position of the main ep interaction region was shifted by the HERA machine by +70 cm along the proton direction ('shifted vertex data'). This way an acceptance in Q^2 down to $Q^2 \geq 0.35$ GeV^2 was achieved allowing to explore the transition region at very small values of x ($x \geq 5 \cdot 10^{-6}$)[7]. Both data sets have been used to measure the structure function F_2. The results of the shifted vertex data analysis have been published in [25]. Details of the analysis can also be found in [26, 27].

This thesis concentrates on the analysis of the nominal vertex data. Although these data extend the kinematic region compared to results from earlier years, the main objective of the measurement is not centered on the kinematic reach but rather on the precise understanding of the new detector components. In the region of Q^2 between 2 GeV^2 and 6.5 GeV^2 the experimental uncertainty of the results is improved compared to former measurements by roughly a factor of 2.

[7] The ZEUS Collaboration has presented results from 1995 data measured with the new beam pipe calorimeter (BPC) reaching down to Q^2 values of 0.11 GeV^2 covering a slightly different range in x [28].

Chapter 2

The H1 Experiment at HERA

In this chapter the experimental steps of the acquisition and reconstruction of deep inelastic ep scattering events with the H1 Detector at HERA are described. The electron proton storage ring HERA is introduced in section 2.1. The detector components of the H1 Detector and the basic steps of the data acquisition are covered in section 2.2. Special focus is put on the new backward calorimeter Spacal which together with the Backward Drift Chamber (BDC) plays a central role in this analysis (section 2.3). The standard methods used to reconstruct the event kinematics are explained (section 2.4) and the event simulation using Monte Carlo programs is sketched (section 2.5).

2.1 The *ep* Storage Ring HERA

The *Hadron-Elektron-Ring-Anlage* HERA [29] was commissioned in 1992. A schematic view of the HERA ring is shown in fig. 2.1. HERA has a circumference of 6.3 km and collides protons of 820 GeV with 27.5 GeV electrons or positrons. During the first years HERA operated with electrons until in 1994 the operation with positrons was established[1]. The lifetime of the positron beams is longer than that of electrons since the positron beam repels the remaining (positively charged) beam gas ions reducing the beam gas interactions and thus the loss of particles. The HERA particle beams are segmented in 220 bunch positions resulting in bunch crossing intervals of 96 ns corresponding to a rate of 10.4 MHz. In a typical run about 190 bunches are filled with about 10^{10} colliding particles each. The remaining ('pilot' and 'empty') bunches are used for control purposes. The average longitudinal size of the proton bunches is about 60 cm leading to a Gaussian distribution of the interaction points along the beam axis with a spread of 10 cm.

HERA accommodates four high energy physics experiments, namely H1, ZEUS, HERMES and HERA–B. H1 (a in fig. 2.1) and ZEUS (b) are taking data of ep collisions since 1992. HERMES (c) is operated since 1995 and uses the electron beam only.

[1] In the following and throughout this thesis the incident and scattered lepton is referred to as electron.

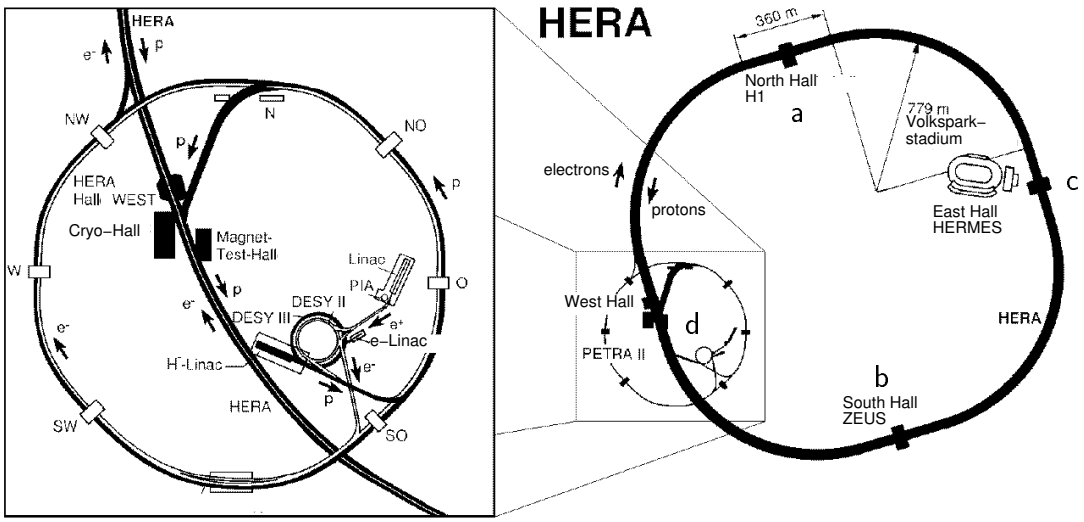

Figure 2.1: Sketch of the *ep* storage ring HERA (right picture) at DESY, Hamburg. HERA accommodates four experiments, H1 (a), ZEUS (b), HERMES (c) and HERA-B (d). The left sketch shows a zoom with the preaccelerator storage ring PETRA and linear preaccelerators.

Polarized electrons are collided with a polarized gas target (H_2, deuterium, ^{3}He or ^{4}He). The experiment HERA-B (d) is a fixed target experiment which uses the halo of the proton beam for collisions with tungsten wires. HERA-B is presently being commissioned and plans to measure CP violation in the decays of B^0 and $\overline{B^0}$ as of 1999.

2.2 The H1 Detector

The H1 Detector [30] was optimized to measure the energies and momenta of the particles produced in deep inelastic scattering and to allow efficient particle identification. A 3-dimensional sketch of the H1 Detector is given in fig. 2.2. The detector is nearly hermetic, its acceptance for scattered particles is limited only by the forward and backward beam pipe holes (near 12 and 13)[2]. Due to the difference between the beam energies of protons and electrons the momenta of most scattered particles have a large component in proton beam (forward) direction. The geometry of the detector, consequently, is asymmetric. The graph 16 shows the coordinate convention used by the H1 collaboration and in this analysis. The z-axis points to the 'forward' direction along the proton beam. The polar angle is defined with respect to this direction. Looking backwards from the interaction point the x-axis points to the right towards the center of the HERA ring.

The central detector components, described below, are embedded in a superconducting coil 6, which produces a homogeneous magnetic field of 1.2 T and an iron return yoke 10, instrumented with streamer tubes for muon detection. In the forward direction

[2]Numbers in □ refer to fig. 2.2.

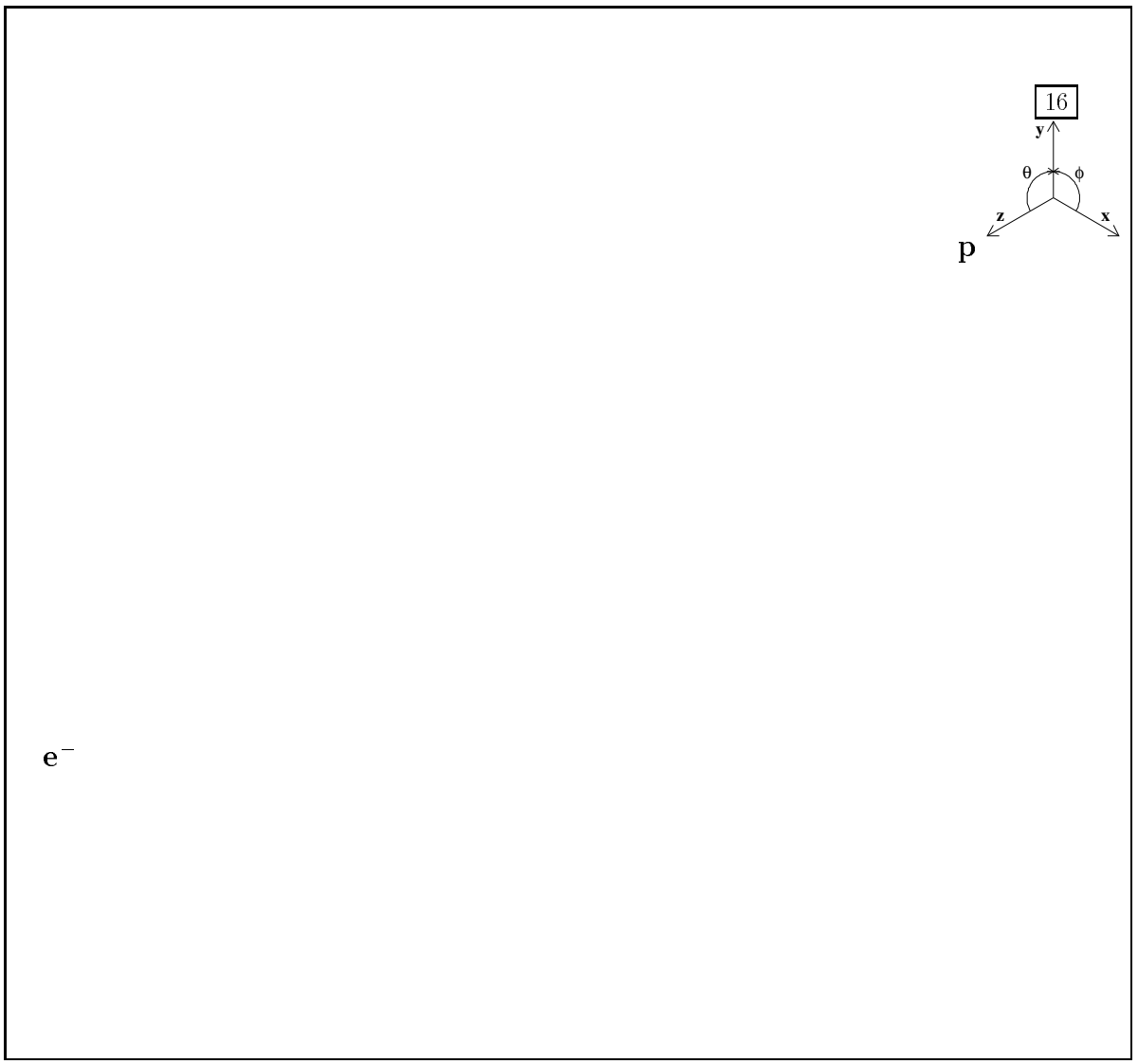

1	Beam pipe and beam magnets	9	Muon chambers
2	Central tracking device	10	Instrumented iron yoke
3	Forward tracking device	11	Forward muon toroid
4	Electromagnetic LAr calorimeter	12	Backw. calorimeter (Spacal)
5	Hadronic LAr calorimeter	13	PLUG calorimeter
6	Superconducting coil (1.15 T)	14	Concrete shielding
7	Compensating magnet	15	Liquid argon cryostat
8	Helium supply for 7	16	Coordinate System

Figure 2.2: Schematic view of the H1 Detector. The different detector components are explained in the text.

the measurement of muons is supplemented by the forward muon spectrometer, [9] and [11]. The following detector components are particularly relevant to this analysis:

- **The Central Tracking Devices**, [2], in the region of -1.5 m $< z <$ 2.5 m comprise six coaxial tracking chambers[3]. Next to the beam pipe the Central Inner Proportional Chamber (CIP), a two layer multi wire proportional chamber, is situated. It is surrounded by the Central Inner z-chamber (CIZ). With its wires oriented perpendicular to the beam pipe the CIZ is optimized for the exact measurement of the z-position of the tracks. The signal wires of the inner Central Jet Chamber (CJC1) are again parallel to the beam axis. The CJC1 covers polar angles between 15° and 165°. The proportional chamber COP, the z-chamber COZ and the Central Jet Chamber 2 (CJC2) analogously repeat this structure in the outer part of the central tracking system.

  CJC1 and CJC2 are optimized to measure tracks in the $r\phi$-plane with a space point resolution of 170 μm. Resolution along z is obtained by comparing the signals read out at both wire ends. Better precision in z is provided by the z-chambers CIZ and COZ which have a resolution of typically 300 μm. The proportional chambers CIP and COP provide a fast signal ($t_{0,vtx}$) used to distinguish between successive beam crossings on the first trigger level.

- **The Forward Tracking Device**, [3], accepts particles with polar angles between $5° \leq \theta \leq 25°$. It consists of three modules of drift and proportional chambers (FPC) and transition radiation detectors each.

- **The Liquid Argon Calorimeter** covers the region between 4° and 153°. It consists of roughly 45000 cells in two sections, an electromagnetic, [4], and a hadronic part, [5], with lead and iron absorber, respectively. Particle energies are measured by ionization of liquid argon atoms and subsequent charge collection. An equivalent of 4 to 8 interaction lengths guarantees a measurement of hadronic energies at a precision of 4% [31] and a resolution σ/E of $50\%/\sqrt{E}$.

- **The Backward Calorimeter Spacal**, [12], is a lead / scintillating-fiber calorimeter of spaghetti type. It covers the backward region, i.e. polar angles of $153° < \theta < 177.8°$. As part of the H1 Detector Upgrade Program [32] the Spacal was installed in the H1 detector in the beginning of 1995 together with the drift chamber BDC (see below). BDC and Spacal replace the backward proportional chamber BPC and the electromagnetic sandwich calorimeter BEMC [30]. The Spacal will be described in detail in section 2.3.

- The exact position of charged particles entering the Spacal is measured by the **Backward Drift Chamber** (BDC) (near [12]) [27, 33]. The BDC is subdivided into 8 octants consisting of 4 double layers which cover the polar angular region

[3]Since 1996 a Silicon Strip Vertex Detector has been in place in addition.

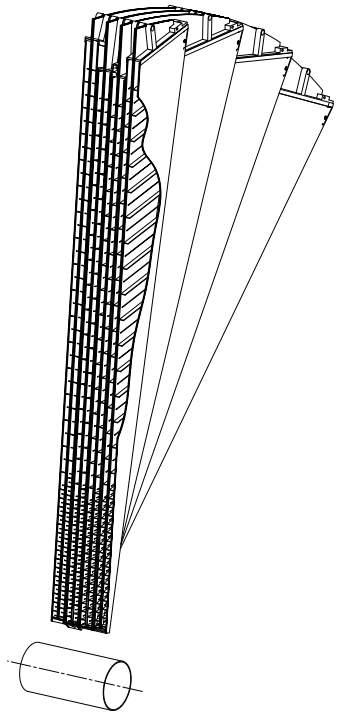

Figure 2.3: 3-dimensional sketch of a BDC octant. The four double layers are rotated relatively to each other by 11.25°. The beam axis is indicated by the dashed-dotted line.

of $153° < \theta < 177.5°$. Fig. 2.3 shows a 3-dimensional sketch of one BDC octant. Each signal wire is contained in a separate cathode cell. For the inner 16 cells the wire distance is 1 cm and for the outer part it is 3 cm. In the transition region between the two zones an intermediate cell with a width of 2 cm is situated. The wires of the transition cells are situated between 21.7 and 23.3 cm in radius, depending on the layer. In total, 2048 signal wires are azimuthally oriented in a spiderweb fashion, i.e. perpendicular to the radius and to the beam pipe. This geometry optimizes the spatial resolution of the polar scattering angle θ which is particularly relevant for the reconstruction of the event kinematics. Together with the Spacal, the BDC is the essential device for the measurement of the scattered electron in the present analysis (see also section 4.7).

- **The Luminosity System** is sketched in fig. 2.4. It comprises two small calorimeters, the electron tagger (ET) and the photon detector (PD), situated at z-positions of -33.4 m and -102.9 m, respectively, upstream of the H1 Detector in the HERA tunnel. Both detectors consist of crystal scintillation counters segmented in 7×7 (ET) and 5×5 (PD) cells of about 2×2 cm^2 size. The photon detector is protected from low energetic synchrotron radiation by a lead-copper absorber of 2 radiation lengths (F) with a water Čerenkov veto counter (VC) which distinguishes events with particles interacting in the absorber from high

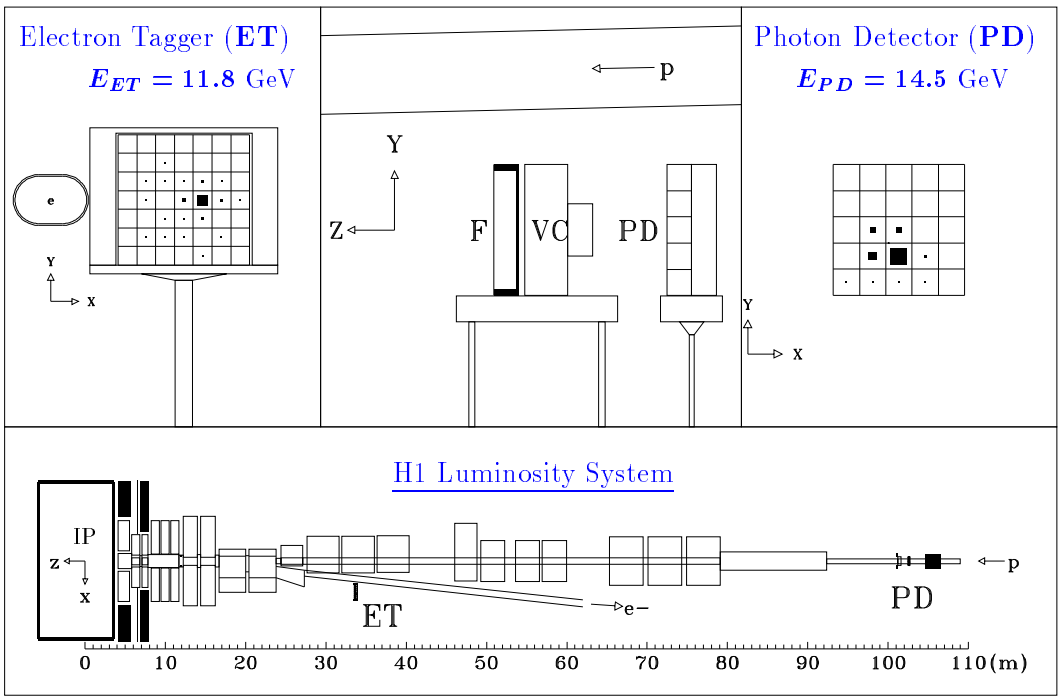

Figure 2.4: Bremsstrahlung event measured by the luminosity system. The scattered electron deposits 11.8 GeV in the electron tagger (ET, upper left panel). The photon energy of 14.5 GeV is measured by the photon detector (PD, upper right panel). The lower picture shows a sketch of the complete luminosity system. The upper central picture zooms the details of the photon detection system consisting of the photon detector (PD) itself and the filter (F) and veto counter (VC) against synchrotron radiation.

energetic photons. The magnetic field of the electron beam optics bends the charged electrons at momenta between 10 and 20 GeV into the electron tagger. Thus, the signal in the electron tagger is devoid of background arising from high energy photons. The luminosity is measured by counting Bethe-Heitler (BH) bremsstrahlung events $ep \to ep\gamma$ [34] (see also section 4.9) detected by the coincidence of a photon and an electron in the luminosity system. Since the cross section of BH events is very large and well known from theoretical calculations, the instantaneous luminosity can be calculated from the measured event rate taking into account the detector acceptances. The systematic uncertainty achieved with 1995 data is 1.07%. The average luminosity was 2.25 $\mu b^{-1} s^{-1}$ at typical currents of 56 mA and 20 mA for protons and electrons respectively [35].

In addition to the luminosity measurement the electron tagger is also used for the identification of photoproduction events (see section 4.8).

- **The Time-of-Flight (ToF) System** consists of scintillation counters situated at different positions along the beam pipe, namely the Backward ToF (BToF, at $z \approx -275$ cm), Forward ToF (FToF at $z \approx 790$ cm, near 1), the Plug ToF

(PToF, at $z \approx 540$ cm, [13]) and the veto walls (at $z \approx -390$ cm). The time resolution is at the level of ns and can therefore be used to reject beam induced background arriving out-of-time in the H1 detector [36]. For this purpose the ToF counters are operated in veto mode on the first trigger level L1. The loss of good events due to the L1 ToF veto condition is of the order of 1% (section 4.4). In this analysis, the PToF is also used for the determination of the vertex reconstruction efficiency (section 4.5). The ToF system supplements the time sensitive electron trigger of the Spacal discussed below.

- **The H1 Trigger System** presently consists of four levels of event filtering, L1, L2, L4 and L5. In 1995 L2 was not yet operational. It was commissioned in 1996.

  The first trigger level L1 [37] is a dead time free system providing trigger decisions after 2.5 μs. During this time the full event information is stored in pipelines. The L1 trigger conditions (subtriggers) are based on simple logical combinations of the trigger signals (trigger elements) from the different detector components. L1 accepts an event if at least one subtrigger condition is fulfilled. A natural trigger rate limit is given by the capacity (bandwidth) of the Read Out System. Facilities to downscale the triggered rate (usually called 'prescales') are implemented. The rate of triggered physics events is optimized to meet the read out bandwidth by imposing prescales to subtriggers with large background contributions. In order to allow the determination of the trigger efficiencies from the data a set of monitor triggers is installed with loose (minimum bias) trigger conditions. For later data analysis the status of each subtrigger before ('raw') and after being accepted by possible prescales ('actual') is recorded with each event.

  L2 validates the L1 decisions using more complex algorithms within 20 μs. At a positive trigger decision the read out of the event is started. The full event information is digitized at the different detector components, collected and transferred to the trigger level L4. In 1995 the actual event rate at L1 ideally was about 30 Hz, corresponding to an averaged dead time of about 10%[4].

  L4 is a software filter consisting of 30 parallel processors[5]. With the complete event information available the event selection algorithm can make full use of the intrinsic detector resolution. About 20% of the events pass the L4 selection cuts and are written to tape. The output event rate is technically limited to about 20 Hz or 1.5 MBytes/s. For monitoring purposes, one out of 100 rejected events is written to a separate data file.

  At L5, finally, the full event reconstruction is performed. Calibration and correction constants are applied to the data (see also section 2.3.4 for the example of the Spacal). The calibrated events are preselected and classified in an analysis dependent way. Non-classified events are rejected to reduce the data volume.

[4]Since 1996 the rate accepted by L2 has been increased to 50 Hz by data volume compression at the front ends of the detector components and optimized background suppression of large events.

[5]Since 1997 36 processors are active.

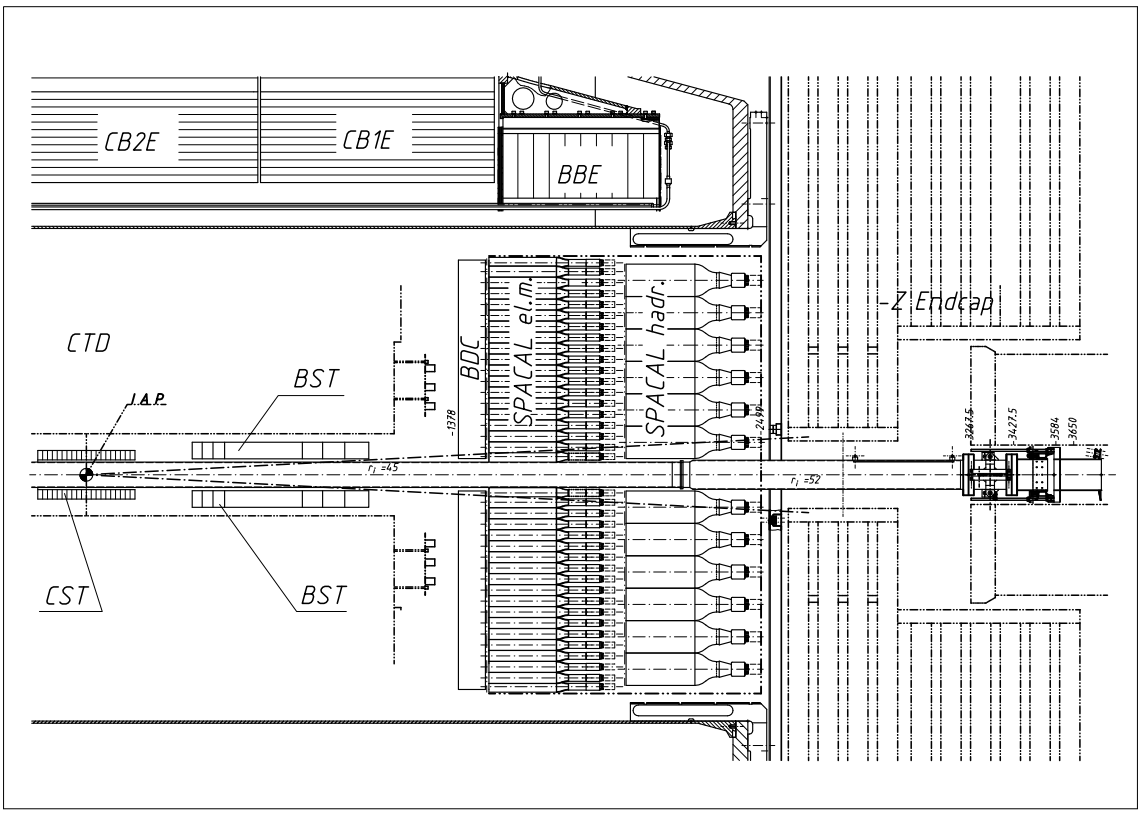

Figure 2.5: Schematic view of the Spacal Calorimeter and the Backward Drift Chamber (BDC) in the backward region of the H1 Detector.

Similar to level L4 1% of the rejected events are stored for monitoring. Classified events are written on so-called Data Summary Tapes (DST) which usually provide the starting point for physics analyses.

2.3 The Backward Calorimeter Spacal

Since 1995 the Spacal Calorimeter replaces the electromagnetic lead / scintillator sandwich calorimeter BEMC and the BEMC-ToF system in the backward region of the H1 Detector. Detailed descriptions of the Spacal can be found in [32, 38].

In this section an outline of the Spacal performance is given. The Spacal detector and the read out and trigger electronics are subsequently described in section 2.3.1 and section 2.3.2. The inclusive electron trigger is covered in a separate section 2.3.3. Finally, in section 2.3.4, the reconstruction of the energy and position of the scattered electron from the raw data is explained.

Fig. 2.5 shows the geometric position of the Spacal Calorimeter in the backward region of the H1 Detector. The front face z-position is -150 cm. The Spacal has a diameter of 160 cm (see fig. 2.6) and consists of two sections, an electromagnetic and a

hadronic section with an active depth of 25 cm each. With the Spacal the calorimetric performance and the background suppression is improved in several aspects:

- The angular acceptance for scattered electrons has been enlarged to a polar angle of 177.8° with respect to the nominal interaction point. With this the kinematic reach[6] extends down to values of $Q^2 \gtrsim 0.85$ GeV^2.
- Small cell sizes of 4×4 cm^2 cross section increase the sensitivity to the measurement of the shower shape, resulting in an improved spatial resolution of less than 4 mm [27] and an enhanced e/π separation power (> 100) [39]. Electromagnetic particles can be separated above a distance of 7 to 8 cm. This allows to resolve exclusive processes (e.g. the measurement of decay products of light mesons such as $\pi^0 \to \gamma\gamma$ [40]) as well as the measurement of QED final state radiation (see section 4.9.2).
- The Spacal has a very good homogeneity (see section 3.5).
- The use of photomultiplier tubes (PMT) and an electronic chain with extremely low noise at a level of 3 MeV [41]) allows very low trigger thresholds and a reliable reconstruction of very small energy deposits. The Spacal is therefore sensitive to minimally ionizing particles. The PMTs provide a time resolution of better than 1 ns allowing the construction of a Time-of-Flight based inclusive electron trigger (IET). The IET provides the means to efficiently reduce the proton beam related background (see section 2.3.3).
- Finally, with the installation of a hadronic calorimeter (replacing the former BEMC-ToF system) the measurement of hadronic energies in the backward region of the H1 detector is improved considerably. The longitudinal division of the Spacal in two parts adds to the e/π separation power (see section 4.6).

The intrinsic performance parameters of the Spacal have been determined in test beam measurements [39, 42]. In the context of the present analysis the basic values are remeasured using DIS events (see chapters 3 and 4). The results are listed in table 2.1. It is expected that in future with more experience an even better performance will be achieved.

2.3.1 Spacal Detector Design

The electromagnetic part of the Spacal consists of 1192 cells with an active volume of $40.5 \times 40.5 \times 250$ mm^3 each. A front view of this section is depicted in fig. 2.6. The cells are made of grooved lead plates and scintillating fibers with a lead / fiber ratio of 2.27:1. 52 stacked lead plates, each comprising 4680 fibers, form a 2-cell-unit (submodule). The fibers have a diameter of 0.5 mm. They are of the type BICRON

[6] For data with nominal ep interaction point.

Acceptance	$153° \leq \theta_e \leq 177.8°$
Energy Resolution (EM) σ_E/E	$7.5\%/\sqrt{\mathrm{E}} \oplus 2\%$
Energy Scale Uncertainty (EM)	0.7% at 27.5 GeV
Energy Resolution (Hadrons) σ_E/E	$\sim 30\%/\sqrt{\mathrm{E}}$
Spatial Resolution σ_R/R	3.4 mm
Time Resolution Δt	≤ 1 ns
Noise level ΔE	≤ 3 MeV

Table 2.1: Performance Parameters of the Spacal measured *in situ* with data from the commissioning year 1995. For the energy resolution for hadrons beam test results with 4 GeV pions are quoted [39].

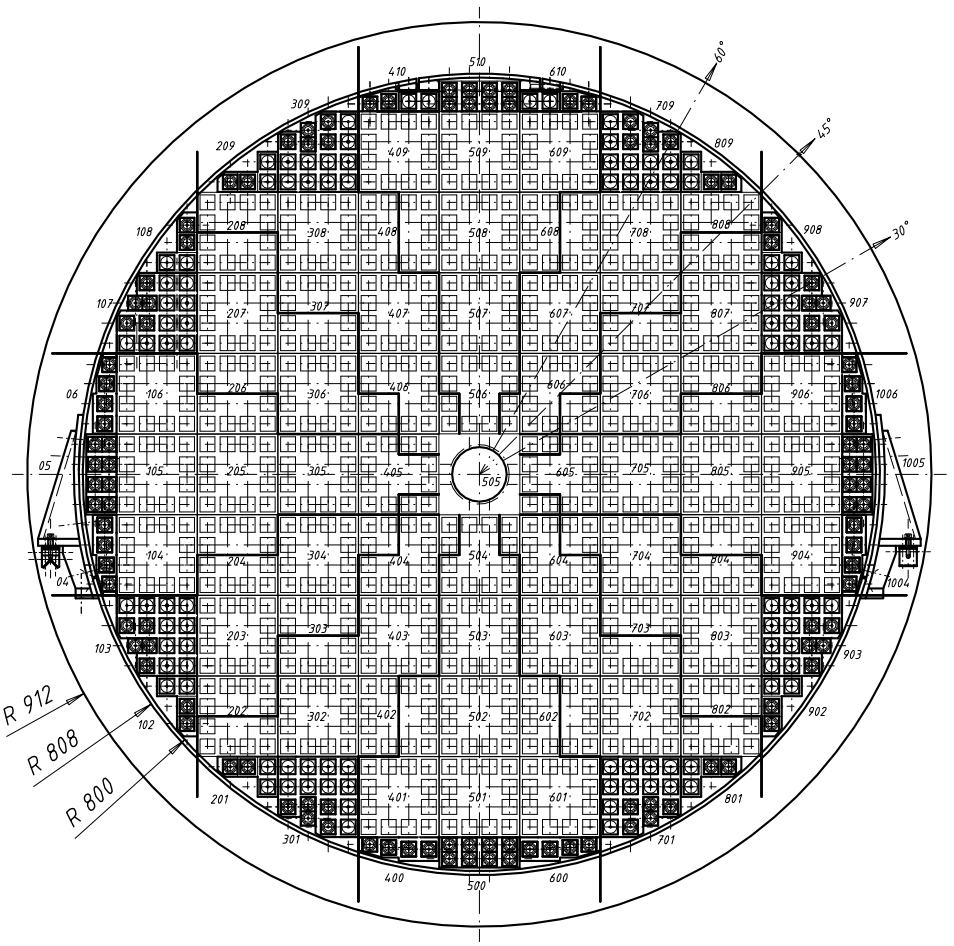

Figure 2.6: Schematic front view of the Electromagnetic Spacal Calorimeter.

Parameter	Electromagnetic Section	Hadronic Section
Fiber Diameter	0.5 mm	1.0 mm
Fiber Type	BICRON BCF-12	BICRON BCF-12
Lead / Fiber Ratio	2.27:1	3.4:1
Number of Cells	1192	136
Cell Volume	$4.05 \times 4.05 \times 25$ cm^3	$12.0 \times 12.0 \times 25$ cm^3
Radiation Length X_0	0.91 cm	0.85 cm
Interaction Length λ	25 cm	25 cm
Molière Radius	2.55 cm	2.45 cm
Lead-Fiber Density	7.3 g/cm^3	7.7 g/cm^3
PMT Type	Hamamatsu R5505	R2490-06

Table 2.2: Technical parameters of the Spacal Calorimeter.

BCF-12 and emit blue light with a peak value of 430 nm. In order to enhance the light transmission, the fibers have a cladding of 20 μm around the fiber core. The core and the cladding have refractive indices of 1.6 and 1.49 allowing for total reflexion up to an angle of 22°. In addition the fibers are mirrored at the front face. An attenuation length of about 3 m is achieved [43]. A standard 16-cell-supermodule is composed of 8 submodules yielding a volume of $162.6 \times 162.6 \times 250$ mm^3. On the back of the supermodule the fibers of each cell are bundled and guided to light mixers. A small air gap between the light mixer and the fibers guarantees a well-defined light transmission. The scintillation light of each cell is converted into an electric pulse using photomultiplier tubes (PMT). The fine-mesh type PMTs [44] are operated in the magnetic field of 1.2 T at an amplification (gain) of $\sim 10^4$.

With a density of 7.3 g/cm^3 and an active length of 25 cm the Electromagnetic Spacal corresponds to 27.47 radiation lengths (X_0) and 1 hadronic interaction length (λ). The Molière radius amounts to 2.55 cm. The basic technical parameters of the Spacal are summarized in table 2.2.

The center of the Spacal contains the Insert, a module shaped to fill the gap between the main body of the Spacal and the beam pipe. The Insert is depicted in fig. 2.7. 12 cells of different sizes encircle four veto layers of 8 mm width. At the inner radius (of 5.7 cm) a tantalum frame shields against synchrotron radiation from the beam. The veto layers are used to measure potential energy leakage into the beam pipe (see section 4.6).

The Hadronic Spacal [45] comprises 136 cells of $120 \times 120 \times 250$ mm^3 providing an equivalent of one nuclear interaction length. The fibers are of the same type as in the electromagnetic section but have a larger diameter of 1.0 mm. With a lead to fiber volume ratio of 3.4:1 the Hadronic Spacal is compensating, i.e. the fraction of detected energy of hadronic and electromagnetic showers is almost equal.

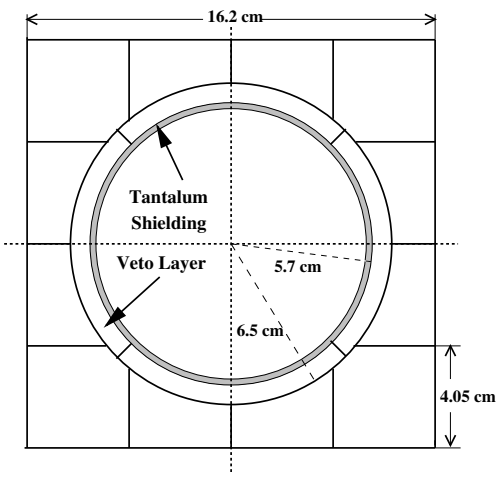

Figure 2.7: Schematic view of the cell geometry of the Insert module in the center of the Electromagnetic Spacal.

2.3.2 Spacal Electronics

A charge integration of the photomultiplier anode signal of each cell is performed by a preamplifier (active base). The decay time constant of the resulting output signal is set to 180 ns in order to avoid pile-up effects. The signal is transported via 19 m coaxial cables into the front end electronics where it is split into three branches, the energy read out, the time measurement and the trigger branches. A detailed description of the Spacal electronics can be found in [46, 47].

- **Energy Read Out Branch:** At the input of the read out branch the pulse is shaped into a bipolar signal with a (positive) peak value of 180 ns. The large time constant ensures insensitivity of the measurement to the exact timing of the read out and the bipolarity guarantees that the signal returns to the base line after a finite amount of time (1.5 μs). The signal is fed through a delay line (pipeline), adjustable between 2.3 and 2.5 μs in steps of 20 ns, and into a sample and hold circuit. In case the event is accepted the signals are multiplexed by 128 cells and read by a peak sensing 12 bit ADC. Two different ADC channels are used, with gains differing by a factor of 4, in order to decrease the digital step width of the ADC for low energy signals. Digital signal processors (DSP) read the ADC data and perform pedestal subtraction and zero suppression. Finally the DSP produce a raw data energy bank which forms the input to the event reconstruction on the trigger levels L4 and L5.

- **The Time Measurement Branch** signal is shaped to rise to its peak value within 3 ns. For the time measurement the signals are fed into Constant Fraction Discriminators (CFD) with a delay of 4 ns and a fraction of 20%. CFDs correct for pulse height effects (slewing) by reshaping the signals such that a 'zero crossing' of the pulse is obtained independent of the pulse height. The threshold is adjusted

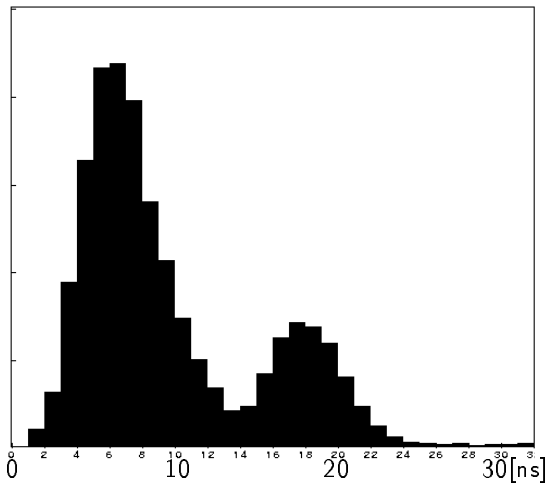

Figure 2.8: Typical time distribution of signals in the Spacal as measured by the TDC online histogramming system. The left maximum corresponds to proton beam related background, the right maximum shows the position of *ep* interactions. Note that no trigger or event selection is performed.

very close to the noise level. In the case of the Spacal a full energy validation can not be performed since the CFD output must be fast enough for use in the trigger branch.

The CFD signal output is split into two subbranches. One signal is fed into the TDC system for the time measurement. The TDC system provides time information of all cells for the offline analysis. The other signal is used for the time dependent event-by-event steering of the Time-of-Flight sensitive inclusive electron trigger (see below).

– The TDC system [48] performs a cell-wise time measurement. It provides the time information for the offline analysis. In addition it is equipped with a fast histogramming unit providing online rates and time spectra for functionality checks and monitoring of the Spacal performance. A typical online histogram of the time distribution measured in the Spacal is depicted in fig. 2.8. The distribution contains all signals arriving in the Spacal with an energy above 30 MeV given by the CFD threshold independent of the H1 trigger conditions. No event selection is performed. The left maximum (around 4 to 8 ns) is due to proton background traversing the Spacal directly from 'upstream'. The right maximum (around 18 ns) contains good *ep* interactions (and electron related background). The relative height of the maxima gives an impression of the proton background rate compared to good *ep* events. The difference in time of 10 ns roughly corresponds to a path length difference of interacting protons and proton background of 2×1.50 m.

  - The time information is also used to select in-time events for the electron trigger. In-time events are defined by an adjustable gate, called Time-of-Flight-window ('ToF-window') as follows: For a given Spacal cell the trigger signal is fed into the ToF-branch of the Spacal trigger (see below) if the CFD signal is in coincidence with the ToF-window. Otherwise it is fed into the 'AToF' (='Anti-ToF') branch. Typically the ToF branch is active in the time window between 8 ns and 24 ns relative to the HERA clock and thus insensitive to proton beam related background (compare fig. 2.8). After a switch to the ToF branch the standard AToF position is recovered automatically 150 ns later.

- **The Trigger branch** [46] works with unipolar signals of 10 ns time constant. It produces analog energy sums, to be compared with adjustable trigger thresholds separately for the ToF and AToF branch and for Hadronic and Electromagnetic Spacal. The ToF branch is highly segmented. It basically comprises the inclusive electron trigger (IET) described in detail below. In the AToF branch coarse energy sums are formed, serving for the positive identification of out-of-time proton related background. The main purpose of the AToF trigger condition is its use as a veto to be applied in combination with other detector components.

2.3.3 The Inclusive Electron Trigger

The inclusive electron trigger (IET) of the Electromagnetic Spacal is segmented in 320 arrays of 4×4 neighboring cells (IET-windows). The IET-windows overlap, they are 'sliding' in order to avoid efficiency gaps at the borders of the windows which would cause loss of events. In each window an analog sum of the in-time (ToF-branch) energies of the 16 cells is separately built. Three different discriminator thresholds, $\mathrm{IET} > 0, \mathrm{IET} > 1$ and $\mathrm{IET} > 2$, adjustable in the range between $\sim$ 100 MeV and $\sim$ 20 GeV, are used to evaluate the analog signal. If, inside a given IET-window, the signal exceeds one of the three discriminator thresholds a logical bit (cluster bit) is set. The Spacal trigger logic computes the logical 'or' of all[7] cluster bits for each of the three thresholds and encodes the result in a 2 bit trigger element sent to the central H1 trigger controller[8]. The design of the IET Trigger combines two assets:

- Spatial segmentation (sliding windows): The segmentation in sliding windows of only 16 cells each allows to (coarsely) localize the position of the scattered electron at the first trigger level L1. Background can be efficiently suppressed using topological criteria[9]. Secondly, coherent noise effects are minimized since the number of channels used in the analog trigger sum is small.

[7] Since 1996 the central region and the outer part of the Spacal have been logically separated.

[8] The cluster bits are also available to the trigger level L2 for more detailed topological evaluation of the event.

[9] Since 1996 a large variety of topological criteria are defined in particular on trigger level L2.

- Time-of-Flight sensitivity (ToF-window): The IET trigger is active during the expected time of arrival of signals from good ep interactions only. Consequently it is insensitive to out-of-time proton background. An external out-of-time veto condition is therefore not necessary to first order.

2.3.4 Reconstruction of the Energy and Position of the Scattered Electron in the Spacal

As mentioned above the reconstruction of the data is performed on the trigger level L5. In this section the reconstruction algorithm for the scattered electron data in the Spacal is briefly sketched. Details about the Spacal reconstruction can be found in [49]. The cell energies are calculated by rescaling the raw data, described in DSP counts, to obtain energy values in GeV. Potential gain variations of the photomultiplier tubes in time are corrected using the correction factors measured by the Spacal LED System [50]. Calibration constants are applied to precisely adjust the cell energies. A clustering algorithm assigns each cell to a local energy maximum ('hottest cell' or 'cluster seed'). Cells with an absolute energy value of less than 15 MeV are rejected[10].

- The cluster energy is given by the sum of the single cell energies inside a cluster.
- The precise shower position is reconstructed by determining the center of gravity $\vec{r}_{\mathrm{cog}}$ of the cluster,

$$\vec{r}_{\mathrm{cog}} = \frac{\sum_{i=1}^{N_{cl}} w(E_i)\vec{r}_i}{\sum_{i=1}^{N_{cl}} w(E_i)}. \tag{2.1}$$

  Here i runs over all cells of a cluster and $\vec{r}_i$ is the position of the center of the i-th cell with the energy E_i. In general the best spatial resolution can be obtained using a logarithmic weight function [51] with the weights following the exponential decrease of the deposited energy with the distance from the center of gravity. However, for the reconstruction of the 1995 data, $w(E)$ is chosen as $w(E) = \sqrt{E}$ (square root-weighting) in order to reduce the sensitivity to noise in the low energy tails of the cluster[11]. In this analysis the special shape of the Insert cells is taken into account according to [52].
- The lateral width of the shower is parametrized by the so-called cluster radius. The cluster radius is defined as

$$R_{cl} = \frac{1}{E_{cl}} \sum_{i=1}^{N_{cl}} E_i |\vec{r}_i - \vec{r}_{cog}|. \tag{2.2}$$

[10] Also negative energy values between -15 and -100 MeV are accepted. Negative energy values arise from noise as well as 'pile-up' effects [47].

[11] Studies have shown that the level of noise in the 1995 data is unexpectedly high (at the level of 5 to 10 MeV), caused by software and hardware problems. A substantial reduction of the noise (to the level of 3 MeV quoted above) has been achieved by maintenance of the Spacal electronics in the shutdown 95/96.

With the help of the cluster radius electromagnetic and hadronic particles can be separated to a large extent (see section 4.6).

2.4 Reconstruction of the Event Kinematics

In deep inelastic ep scattering at HERA the energy and the angles of both the scattered electron and the hadronic final state are measured independently, providing four kinematic quantities in the laboratory frame, namely E'_e, θ_e, E_h and γ_h. Two of the four quantities suffice to determine the Lorentz invariant variables x, y and Q^2 and to unambiguously define the kinematics of the lowest order ep scattering process (see section 1.1). Thus, the event kinematics is overconstrained.

The redundancy of the measurement can be exploited for two important purposes: First and most importantly, detector resolution effects can be minimized by combining the quantities measured with the least systematic uncertainty; and second, influences from higher order effects can be detected and corrected by combination of differently derived kinematic variables.

Before discussing the different reconstruction methods the kinematic quantities are briefly introduced. E'_e and θ_e describe the energy and the polar angle of the scattered electron. E_h and γ_h are derived summing over all particles of the hadronic final state. γ_h is called the 'jet angle' or in the parton picture the scattering angle of the struck quark (see also fig. 1.1(b)). It is defined as

$$\tan\frac{\gamma_\mathrm{h}}{2} = \frac{\Sigma}{p_{\perp,h}} \tag{2.3}$$

where $p_{\perp,h}$ is the total transverse momentum of the hadrons and $\Sigma = \sum_\mathrm{hadrons}(E - p_z)$ is the difference between the energy and the z-component of the momentum summed over all particles of the hadronic final state,

$$\Sigma \equiv \sum_{\text{had. fin. state}} (E_i - p_{z,i}) = \sum_{\text{had. fin. state}} E_i(1 - \cos\theta_i). \tag{2.4}$$

Adding the contribution $E'_e - p_{z,e}$ of the scattered electron one obtains

$$E - p_z \equiv \sum_{\text{all particles}} (E_i - p_{z,i}). \tag{2.5}$$

Due to energy and momentum conservation $E - p_z = 2 \cdot E_e = 55$ GeV before and after the scattering. Thus, $E - p_z$ is sensitive to high energetic particles escaping through the backward beam pipe hole. The measured value of $E - p_z$ is reduced by twice the energy of the lost particles. This property is particularly useful for the detection of events with bremsstrahlung photons (see section 4.9) and low angle scattered electrons in photoproduction processes (see section 4.8). Furthermore, $E - p_z$ can be used as a constraint for calibration purposes (see section 3.6).

Method	Q^2	y
e	$4 \cdot E'_e \cdot E_e \cdot \cos^2\frac{\theta_e}{2}$ (2.6)	$1 - \frac{E'_e}{E_e} \cdot \sin^2\frac{\theta_e}{2}$ (2.7)
JB	$\frac{(\sum p_{\perp,h})^2}{1 - y_{\mathrm{JB}}}$ (2.8)	$\frac{\Sigma}{2 \cdot E_e}$ (2.9)
Σ	$\frac{p^2_{\perp,e}}{1 - y_\Sigma}$ (2.10)	$\frac{\Sigma}{E - p_z}$ (2.11)
DA	$\frac{4 \cdot E_e^2 \cdot \sin\gamma_{\mathrm{h}} \cdot (1 + \cos\theta_{\mathrm{e}})}{\sin\gamma_{\mathrm{h}} + \sin\theta_{\mathrm{e}} - \sin(\theta_{\mathrm{e}} + \gamma_{\mathrm{h}})}$ (2.12)	$\frac{\sin\theta_{\mathrm{e}} \cdot (1 - \cos\gamma_{\mathrm{h}})}{\sin\gamma_{\mathrm{h}} + \sin\theta_{\mathrm{e}} - \sin(\theta_{\mathrm{e}} + \gamma_{\mathrm{h}})}$ (2.13)

Table 2.3: Relations for the reconstruction of the event kinematics using different methods.

In the following the different methods to reconstruct the event kinematics are presented and their performance is discussed. Detailed descriptions of the methods and comparisons can be found in [53, 54]. In table 2.3 the basic relations for the calculation of Q^2 and y are given. In all methods x is derived via the relation $x = Q^2/ys$ (section 1.1).

- **The Electron Method** (e in table 2.3) exclusively uses the angle θ_e and the energy E'_e of the scattered electron. The resolution in y depends on the precision of the measurement of calorimetric energy and polar scattering angle as

$$\frac{y-1}{y}\left(\frac{\delta E'_e}{E'_e} \oplus \frac{\delta\theta_e}{\tan(\theta/2)}\right). \tag{2.14}$$

  Here, $\oplus$ stands for a quadratic summation of the terms. At high y the resolution in y of the e method is superior to all other methods. Towards lower y the resolution degrades as $1/y$. For the use of the electron method in the range of moderate and small y the optimization of the detector resolutions is mandatory. At $y \lesssim 0.2$ other methods are preferable. The resolution of Q^2_e, at low Q^2, depends mainly on the precision of the polar scattering angle θ_e. Towards high Q^2 the influence of the energy scale of the scattered electron increases. The kinematics of the e method is directly affected by bremsstrahlung processes off the incident electron (QED initial state radiation, see section 4.9) which lead to a reduction of

the incident electron energy, and cause large migrations in the electron variables. However, since this process is well known Monte Carlo simulations can be used to correct for radiative effects.

- **The Hadrons-Only Method**, often called 'Jaquet Blondel' (JB) after its developers [55], defines $y_{\rm JB}$ and $Q^2_{\rm JB}$ purely on the basis of the distribution of hadronic energies and momenta as measured by the calorimeter or by both the calorimeter and the tracking devices. At $y \lesssim 0.2$ the method provides a fairly precise measurement of $y_{\rm JB}$. The resolution in y is proportional to the hadronic energy resolution which degrades towards high values of y. The precision of $Q^2_{\rm JB}$ is poor due to the loss of hadrons with transverse momenta in the beam pipe. Besides the good resolution of $y_{\rm JB}$ at low y the hadrons-only method is to first order independent of radiative corrections and it is the only possible method for charged current events in which the outgoing neutrino is not detected.

- **The Σ Method**, in contrast to the above methods, makes more efficient use of the redundancy of the measured variables. y_Σ and Q^2_Σ are derived in analogy to the JB method, replacing the nominal electron beam energy, E_e, by the measured beam energy, $(E - p_z)/2$, and the hadronic transverse momentum by the transverse momentum of the scattered electron. The Σ method has a good resolution in a wide kinematic range. The resolution of y_Σ is given as

$$(1-y)\left(\frac{\delta\Sigma}{\Sigma} \oplus \frac{\delta E'_e}{E'_e} \oplus \frac{\delta\theta}{\tan(\theta/2)}\right). \tag{2.15}$$

  At small y the resolution behaves like the hadrons-only method since $\frac{\delta\Sigma}{\Sigma}$ is the dominating contribution. With increasing y the decrease of the term $(1-y)$ partially compensates the rise of $\frac{\delta\Sigma}{\Sigma}$. At large y where the contribution from hadrons to $E - p_z$ becomes comparable to the electron, the fluctuations of the measured hadronic energies start canceling between the nominator and denominator in equation (2.11).

  Replacing the nominal electron beam energy by the measured value of Σ the Σ method implicitly accounts for losses of incident electron energy due to QED initial state radiation (section 4.9).

  In this analysis y_Σ is determined using a combination of central tracks and calorimeter cells. The momentum measured from tracks is included if the transverse track momentum is less than 300 MeV. An isolation criterion is used to avoid counting the energy in calorimeter cells originating from a track already taken into account.

  Generally, x_Σ can be derived in two different ways since s can be computed from either the recalculated beam energy or the nominal beam energy. Here, the latter way is chosen using $s = 4 \cdot E_e \cdot E_p$.

- **The Double Angle Method** (DA) uses the polar angles of the scattered electron θ_e and the hadronic final state $\gamma_{\rm h}$. It provides reasonable resolution at medium y ($0.05 \gtrsim y \gtrsim 0.3$). Towards very low and very large values of θ_e and $\gamma_{\rm h}$ both Q^2 and y resolutions degrade as $\frac{\delta\theta_e}{\sin\theta_e} \oplus \frac{\delta\gamma_{\rm h}}{\sin\gamma_{\rm h}}$. The double angle method is therefore less precise at small values of Q^2 where the electron scattering angle is large and outside the region of moderate y where the angle of the struck quark approaches 0° or 180° respectively. However, using angles only, it is to first order independent of the overall energy calibration and can therefore be used for calibration purposes (section 3.4). The energy of the scattered electron is reconstructed from the two scattering angles via the relation

$$E_{\rm DA} = \frac{E_e \cdot \sin\gamma_{\rm h}}{\sin\gamma_{\rm h} + \sin\theta_e - \sin(\theta_e + \gamma_{\rm h})}. \tag{2.16}$$

2.5 Event and Detector Simulation

The properties of the measured data can be regarded as a convolution of pure physics event characteristics with the intrinsic detector resolutions. Monte Carlo simulations (MC) of the physics processes and the detector behavior are used to reproduce the measured data with the aim of disentangling the two contributions. Consequently, the Monte Carlo calculations are divided into two parts, the Monte Carlo generator and the detector simulation. The pure physics process is simulated on generator level according to a given theoretical model. As the result of the MC event generation the four-momenta and identities of all particles in the final state are known. In a second step the generated events are fed into the detector simulation program (H1SIM [56]) based on GEANT [57]. The detector response is computed taking the detector geometry and the resolution of the different detector components into account. The correct description of the detector material is crucial. The simulation of the detector response depends not only on the correct description of the active detector material but also on the understanding of dead material effects. Interactions of the initial particles with dead detector material may in particular lead to preshowering processes. Incorrect description of these processes may in turn cause problems in the understanding of detector effects (see section 4.7). The detector simulation requires by far the largest amount of computing time and makes the mass production of Monte Carlo events difficult.

The simulated Monte Carlo data are reconstructed in the same way as the measured data in order to allow the use of the same analysis chain. In the present analysis two specific generator programs are used, namely DJANGO [58] for the simulation of deep inelastic scattering events and PHOJET[59] for the estimation of the photoproduction background.

- The generator **DJANGO** is based on HERACLES [60] and LEPTO [61]. HERACLES simulates electroweak processes taking into account leptonic and quarkonic

radiative corrections to first order $\mathcal{O}(\alpha)$ as well as one-loop corrections (see section 4.9). The x and Q^2 dependence of the generated cross section can be chosen using parametrizations of parton densities available in the PDFLIB [62].

LEPTO provides the fragmentation of the scattered quark. In the present analysis the Color Dipole Model as implemented in ARIADNE [63] is chosen because of its good description of the hadronic final state measurements [64]. The hadronization step is computed using the Lund-string model as implemented in JETSET [65].

DJANGO does not generate events with a large rapidity gap. Possible influences on the final result have been investigated using the Monte Carlo generators RAPGAP [66] and DIFFVM (see section 4.5).

The cross section assumed for the generation of the DIS events is chosen according to the GRV parametrization [20] (see section 5.4). The simulated event sample used for the analysis of the nominal vertex data corresponds to an integrated luminosity of 1689 nb^{-1} (289 nb^{-1} with $Q^2 < 1$ GeV^2). For the shifted vertex data analysis a set of events was generated using the MRSD0' description [67] since at small Q^2 (by construction) GRV is unrealistically small (see section 5.4). MRSD0' is used at very small values of Q^2 ($Q^2 < 0.35$GeV^2) and high y ($y > 0.5$).

- **PHOJET** [59] simulates all components of the total photoproduction cross section. Detailed descriptions of photoproduction processes can be found in [68]. PHOJET incorporates both soft and hard hadronic processes. The soft processes are modelled using Regge phenomenology while the hard processes are calculated using perturbative QCD with leading order matrix elements. The hadronization is performed by the Lund-string model in JETSET [65] and the flux of quasi-real photons is generated using the generator IJRAY [69].

  PHOJET allows to distinguish between diffractive and non-diffractive events. Non-diffractive events classify as resolved photon or direct processes. Diffractive events, mediated by exchange of a colorless object, may appear in four different categories, as sketched in fig. 2.9. There are elastic processes (EL: $\gamma p \to Vp$ where $V = \rho^0, \omega, \phi$), Photon Diffraction (GD: $\gamma p \to Xp$), Proton Diffraction (PD: $\gamma p \to VY$), Double Dissociation (DD: $\gamma p \to XY$). The diffractive contribution to the photoproduction cross section is of the order of 50%. In this analysis the distinction of the diffractive components turns out to be relevant for the estimation of the photoproduction background (section 4.8) since the four classes have strongly different event signatures. The figure is taken from [3], detailed explanations can be found in [70].

  For the detector simulation of the photoproduction background events a so-called 'Turbo' program is used. Turbo preselects potential background event candidates for the simulation and rejects events with no high energetic particles in the backward region. With Turbo a reduction in the number of events to be simulated by roughly a factor of 5 is achieved, thus saving computing time and data stor-

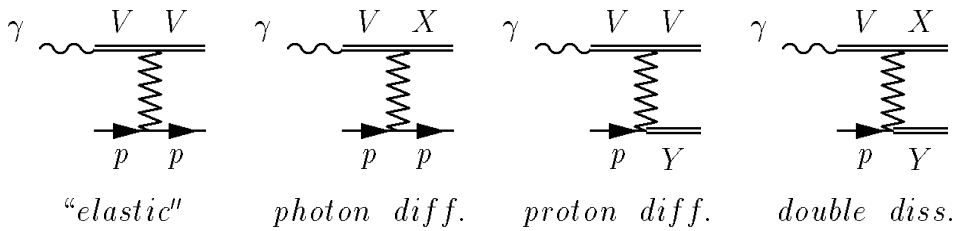

Figure 2.9: The four classes of diffractive processes are sketched. From left to right Elastic processes (EL), Photon Diffraction (GD), Proton Diffraction (PD) and Double Dissociation (DD).

age media. The simulated event sample used for the analysis corresponds to an integrated luminosity of 150 nb^{-1}.

Chapter 3

Energy Calibration

With the installation of the Spacal in the H1 Detector in Spring 1995 an extensive calibration and adjustment program was set up leading to continuous improvements in the detector performance. The initial energy calibration was obtained by the iterative application of several independent methods, exploiting the photoelectron statistics of the photomultiplier tubes with the help of the LED system [50, 71] and using cosmic muons [72], proton beam halo muons [73] as well as π^0 decays [74].

The energy calibration pursues two main objectives, namely the relative equalization of the response of the calorimeter cells and the determination of the absolute energy scale. The relative equalization of the calorimeter cells is necessary in order to achieve a homogeneous detector response and optimum energy resolution. The absolute calibration is vital for the correct reconstruction of the event kinematics and internal consistency between different reconstruction methods. The aim is to maximize the accessible phase space with good precision.

This chapter focuses on the final step of the energy calibration for the measurement of the structure function F_2 of the proton, using scattered electrons in the 'Kinematic Peak' and the 'Double Angle Method'. The calibration with scattered electrons provides by far the most precise results. However, the rate of scattered electron events in the Spacal decreases strongly with decreasing scattering angle ($\sim 1/\cos^4\frac{\theta}{2}$). Thus, the event rate at large radii is small. In 1995, due to lack of statistics, only the inner part of the Spacal could be calibrated with scattered electrons. The outer part of the Electromagnetic Spacal, at radii above $\sim$ 35 cm, as well as the cells of the Hadronic Spacal were calibrated using cosmic muon data.

In section 3.1 an introduction to the nature of the kinematic peak of scattered electrons is given. The determination of corrections for each individual Spacal cell is discussed in section 3.2. In section 3.3 the calibration procedure is presented. Events in the kinematic peak are selected with the requirement that the inelasticity reconstructed from the hadronic final state is small yielding a so-called 'monochromatic' energy distribution. The results of the calibration are cross checked using the double angle method (section 3.4). Investigations on the spatial homogeneity of the detector response and its

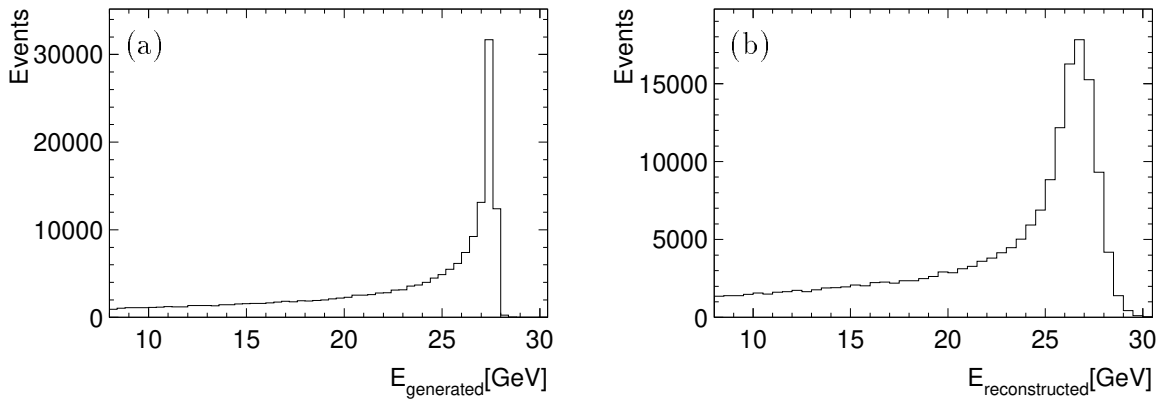

Figure 3.1: The kinematic peak of the energy spectrum of the scattered electrons using Monte Carlo simulated events (a) on generator level and (b) on reconstruction level.

linearity are briefly summarized in section 3.5. Finally, the calibration of the hadronic energies in the Spacal is presented (section 3.6) and a summary is given (section 3.7).

3.1 The Kinematic Peak

In ep-collisions at low and moderate Q^2 ($Q^2 \lesssim 100$ GeV^2) at HERA the energy distribution of scattered electrons has a characteristic shape with a prominent maximum, commonly called 'kinematic peak', close to the electron beam energy of 27.5 GeV. This is illustrated in fig. 3.1(a) showing a typical energy distribution of scattered electrons in a Monte Carlo simulation of ep DIS events on generator level, i.e. without simulation of the detector response (see section 2.5). As its name suggests the peak originates mainly in kinematic effects. Small influences arise from the parton distributions in the proton and from calorimeter properties.

The shape of the energy spectrum can be understood by inspection of the cross section dependence on the inelasticity y. Equation (1.12), given in section 1.2, can be rewritten as

$$\frac{\mathrm{d}^2\sigma}{\mathrm{d}Q^2\mathrm{d}y} = \frac{2\pi\alpha^2}{Q^4 y}\left(2(1-y) + \frac{y^2}{1+R}\right) F_2(x,Q^2). \tag{3.1}$$

The structure function F_2 itself is comparatively flat in the entire kinematic region accessible (see section 1.4). Therefore, at sufficiently small values of y the cross section rises proportionally to $1/y$. It does not diverge since in the limit of $y \to 0$, or $x \to 1$, $F_2 \to 0$. The $1/y$ dependence translates into the energy behavior via the relation

$$\frac{1}{y} = \frac{E_e}{E_e - E'_e \sin^2(\frac{\theta}{2})}. \tag{3.2}$$

The above equations show that the cross section becomes large in the region of $E_e \approx E'_e \sin^2(\frac{\theta}{2})$. Formally, the same result can be derived from equation (3.1) by virtue of a

(Jacobian) transformation of variables $\sigma(y, Q^2) \rightarrow \sigma(E, \theta)$. In fact the kinematic peak appears more and more pronounced towards smaller Q^2 since here the phase space corresponding to the region where the electron is scattered with roughly the beam energy increases. This is also visualized in the context of section 5.1 in fig. 5.1.

The width of the kinematic peak obtained from the calorimetric measurement of the scattered electron is mainly due to the resolution of the calorimeter. The relatively sharp true energy distribution (fig. 3.1(a)) is widened as soon as detector effects are taken into account (fig. 3.1(b)). Note that due to the non-symmetric shape of the true energy distribution the maximum of the reconstructed distribution appears slightly shifted towards lower energies. Secondary influences on the shape of the peak may arise from energy losses due to dead material in front of the detector as well as possible leakage effects etc.

Being predominantly of kinematic origin the position of the kinematic peak is in good approximation independent of the structure function. Monte Carlo simulations are used to predict the exact position and shape of the kinematic peak measured in the calorimeter as a function of the scattering angle and the detector resolution. The residual influences from the behavior of the structure function can also be simulated according to the current knowledge (see section 2.5). In this sense the Monte Carlo simulation can be viewed as providing data from an ideally calibrated detector. It therefore provides a suitable reference for the calibration of the energy scale.

The energy calibration using kinematic peak electrons is based on comparisons between Monte Carlo simulations and data. Correction factors are applied to the data such that the measured position of the kinematic peak matches with the simulated expectation. Once a certain precision is reached, secondary effects start dominating and the simulated cross section and detector resolution must be tuned to optimally describe the data. At this level of precision the measurement of the cross section becomes relevant to the energy calibration. The calibration therefore consists of an iterative procedure in which data and Monte Carlo simulations are successively brought to convergence.

3.2 Relative Calibration of the Calorimeter Cells

Typically 10 to 20 cells share the energy of the scattered electron as it produces an electromagnetic shower in the calorimeter. Unfortunately, the details of the shower development are not reliably simulated quantitatively. This is illustrated in fig. 3.2 showing the fraction of energy deposited in the hottest, i.e. the most energetic, cell of the electron cluster for data and Monte Carlo simulation. The discrepancy visualizes that the parametrization of the shower development used in this Monte Carlo simulation has not yet been tuned precisely enough. As a consequence the simulated showers are too compact, and data and Monte Carlo simulation are not comparable

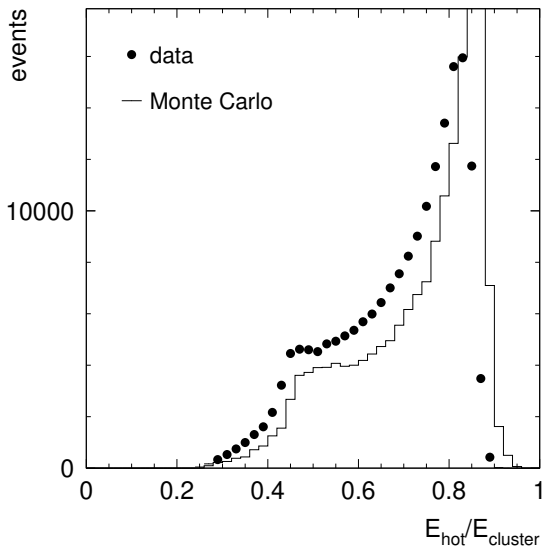

Figure 3.2: Fraction of the electron energy carried by the hottest cell in the cluster in data (points) and Monte Carlo simulations (solid line).

on the cell level (see also section 4.6)[1]. However, the impact on the energy calibration is small as long as the total cluster energy (E_{cl}), i.e. the sum of the cell energies in the cluster, which in the measurement is identified with the energy of the scattered electron (E'_e), matches between the Monte Carlo simulation and the data. The aim is to determine the corrections of the individual cells such that the cluster energies in data and simulation match.

In a general form the problem of the calibration can be described by a system of linear equations where the coefficients denote correction constants of the individual Spacal cells. Such an approach was followed in [75]. Another method of extracting calibration constants of the individual cells is based on simultaneous fits of the correction constants to the expected energy distribution [76]. The latter approach is technically quite complicated and depends somewhat on the expectation of the shape of the energy distribution.

In the following the 'Method of the Hottest Cell' is used which, although being technically much simpler, yields an equivalent precision. The correction factor c_i for a given cell i is defined as

$$c_i = \frac{\langle E^{MC}_{cl,i} \rangle}{\langle E^{data}_{cl,i} \rangle}, \tag{3.3}$$

[1]The Monte Carlo simulation of the Spacal used in this analysis was tuned to beam test measurements only. One of the reasons for the discrepancy between beam test and *in situ* measurements may be the dead material in front of the Spacal causing preshowering effects which appear as widening of the shower in the Spacal.

where $\langle E_{cl,i} \rangle$ is the electron cluster energy reconstructed in events in which the given cell i is the hottest cell of the electron cluster. The correction factor is calculated using the total cluster energy and assigned to the hottest cell in the cluster. Such a treatment is based on the fact that the hottest cell contains the dominant contribution to the cluster energy as is shown in fig. 3.2. The fraction of energy deposited in the hottest cell amounts on average to about 65% of the cluster energy with a maximum at about 80%. Consequently, the ideal correction factor of the hottest cell can be approximated using the correction factor calculated from the cluster energy. It is, however, obvious that miscalibrations of the neighboring cells in the cluster cause deviations of the obtained correction factor from the ideal value. The effect is minimized by performing iterations with recalibrated cell energies until the remaining correction constants are small. The main disadvantage of this simple method is given by the fact that each event can be used for the calibration of only one cell, namely the hottest. In addition the convergence behavior of this method is rather slow and formally not fully understood.

3.3 Calibration Procedure

3.3.1 Event Selection

In the naive approach, outlined in the last paragraph, kinematic peak electrons are selected in an interval around the electron beam energy (e.g. between 23 and 30 GeV). Background in this region originates mainly from proton gas interactions. It is suppressed by demanding that the cluster radius be less than 3.3 cm (see section 2.3.4) and the measured Time-of-Flight within 10 and 20 ns (see section 2.2). With these cuts typically an energy distribution similar to the distribution shown in fig. 3.1(b) is obtained[2]. The correction constant of the hottest cell is then derived from the ratio between the arithmetic mean values of Monte Carlo simulation and data. This procedure is established for the routine calibration of the Spacal data. Neglecting the discrepancies in the shape between data and Monte Carlo simulations the uncertainties on the absolute energy scale amount to 1–2% [71].

Better precision can be gained by exploiting the fact that the event kinematics is overconstrained by the measurement of both the hadronic final state and the scattered electron (see section 2.4). Selecting events with the requirement that $y_{\mathrm{JB}} < 0.05$ the fraction of events with electrons scattered at beam energy can be enhanced. This is illustrated in fig. 3.3(a) which plots the true electron energy spectrum at generator level of the Monte Carlo simulation with the cut $y_{\mathrm{JB}} < 0.05$ applied at detector level. The distribution has a very sharp peak at the electron beam energy (compare with fig. 3.1(a)). The distribution is often called monochromatic since almost all selected electrons have the same energy. The tail towards lower energies originates from radiative events where the energy of the incoming electron is reduced by radiating a

[2] The figure shows the distribution without the energy cut.

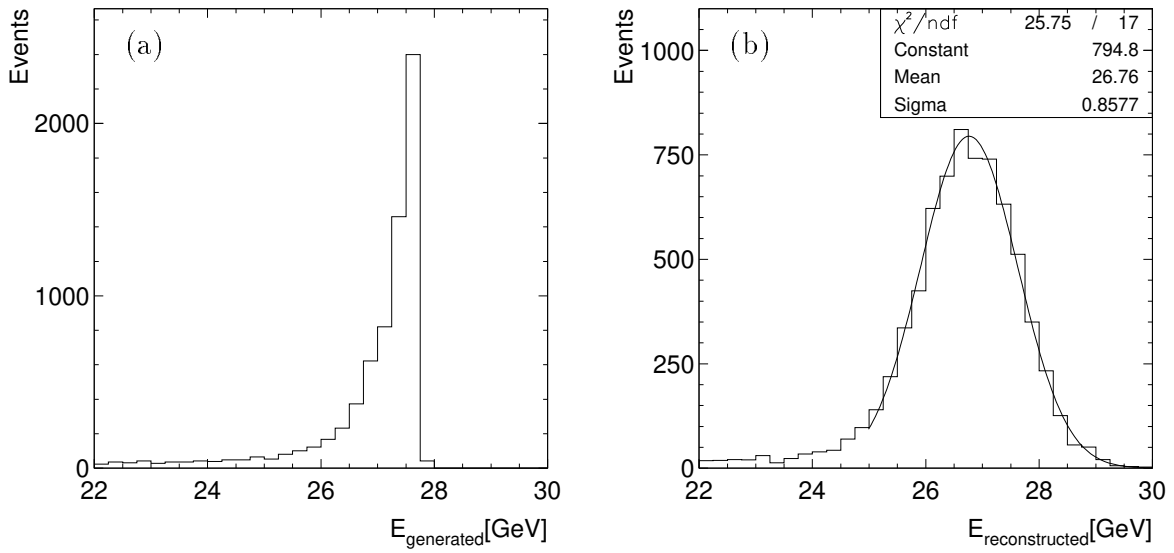

Figure 3.3: Monochromatic energy distribution of the scattered electron using Monte Carlo simulations (a) on generator and (b) on reconstruction level selecting events at $y_{\mathrm{JB}} < 0.05$. In (b) a Gaussian function is fitted in the interval of 25 GeV to 30 GeV. The parameters of the Gaussian are displayed in the figure caption.

bremsstrahlung photon (see section 4.9). Fig. 3.3(b) shows the same Monte Carlo simulated events after detector simulation and reconstruction. The distribution is wider due to the finite detector resolution and can be described by a Gaussian function above 25 GeV. The Gaussian shape of the energy distribution results in the following advantages for the calibration, compared to the naive approach.

- It allows a simple determination of the maximum independent of the radiative tail towards lower energies.

- The influence of the simulated cross section is reduced. Cross section discrepancies between the data and the Monte Carlo simulation, do to first approximation not affect the shape but only the normalization of the measured distribution.

- The width of the distribution allows an effective detector resolution to be determined directly from the data. This information is useful to tune the Monte Carlo simulation to a realistic description of the detector. Note that for the intrinsic detector resolution the width of the underlying true monochromatic energy distribution must be taken into account.

In order to make use of these advantages it is, however, necessary to investigate the influence of the selection cut $y_{\mathrm{JB}} < 0.05$ on the result of the calibration. The distribution of y_{JB} is investigated in the following.

3.3.2 Understanding the y_{JB} Distribution

In fig. 3.4 the measured distribution of y_{JB} is shown in a logarithmic scale for data and Monte Carlo simulations. Here, all selection cuts of the structure function analysis as given in table 4.1 are applied except the requirement of a reconstructed vertex (cut # 10 in table 4.1). Events at $\log_{10}(y_{\mathrm{JB}}) < -4.4$ are accumulated in the overflow bin at -4.4. While at $\log_{10}(y_{\mathrm{JB}}) > -1.6$ (corresponding to $y_{\mathrm{JB}} \gtrsim 0.025$) the distributions match reasonably well, disagreement is revealed at smaller values of y_{JB}. In this region the data overshoot the Monte Carlo simulation.

One of the possible reasons for this behavior may be the fact that the simulation program DJANGO does not generate events at values below $W_{\mathrm{gen}} < 4$ GeV (corresponding to $y \lesssim 2 \cdot 10^{-4}$). W_{gen} denotes the generated invariant mass of the hadronic final state. Hence, lack of rate is inherent to the Monte Carlo simulation which due to migrations may extend to relatively large values of y_{JB}. The size of the effect is estimated by double counting the simulated events in the region $4 \text{ GeV} < W_{\mathrm{gen}} < 8$ GeV. The resulting distribution, shown as a dashed line in fig. 3.4(a), indicates that the influence is quite large. It must be mentioned here that in the low Q^2 region a realistic description of the cross section at very small values of W must take into account the production of resonances together with the fact that F_2 vanishes in the limit of $x \to 1$, i.e. $W \to m_p$, where m_p is the proton mass. Double counting of events is thus only justified in the framework of this technical investigation.

Event migration to larger y can be identified using the hadronic jet angle γ_{h} of the scattered quark (equation (2.3) in section 2.4) in comparison with the equivalent quantity γ_e as reconstructed using the angle and the energy of the scattered electron[3]. The distribution $\gamma_{\mathrm{h}}/\gamma_e$ is shown in fig. 3.4(b). The tail towards small values of $\gamma_{\mathrm{h}}/\gamma_e$ mostly belongs to radiative events where γ_e is overestimated. Events with badly reconstructed γ_{h} are situated in the tail towards large values of $\gamma_{\mathrm{h}}/\gamma_e$. The overflow bin at a value of 3 accommodates events with $\gamma_{\mathrm{h}}/\gamma_e \geq 3$. The distribution shows that the γ-criterion can be used to verify the measurement of the hadronic final state. Events which do not obey the relation $\gamma_{\mathrm{h}}/\gamma_e < 2$ are rejected. The resulting distribution of y_{JB} is shown in fig. 3.4(c) for data and Monte Carlo simulations. Comparison with fig. 3.4(a) shows that the rejected events originate from the region of low y. The fact that the fraction of rejected events in the data is larger than in the Monte Carlo simulation indicates that the migrations in data are larger than expected. The investigation shows that the γ-criterion provides a handle to control possible influences on the calibration due to discrepancies between the Monte Carlo simulation and the data in the low y region. The calibration procedure itself, described in the following, is performed without the γ-criterion (since it makes use of the measured electron energy). The γ-criterion will be used to cross check the result.

[3] γ_e is obtained in a similar way as γ_{h} replacing the hadronic quantities in equation (2.3) with the same variables measured from the scattered electron, $\tan\frac{\gamma_e}{2} = \frac{2\,E_e y_e}{p_{\perp,e}}$.

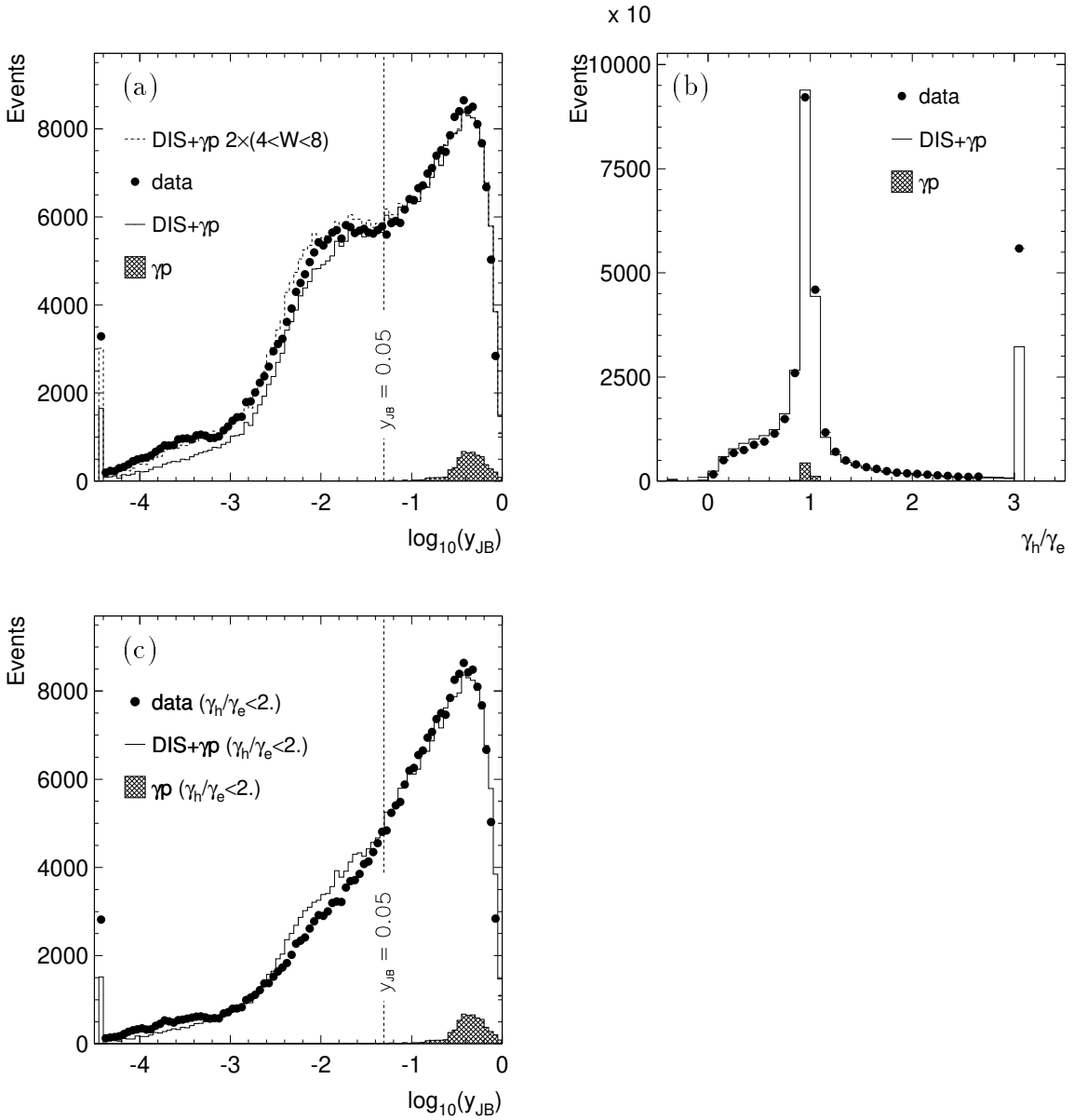

Figure 3.4: (a) Distribution of $\log_{10}(y_{\rm JB})$ in data (points) and DIS+γp Monte Carlo simulation (solid line). Events with $\log_{10}(y_{\rm JB}) < 10^{-4}$ are accumulated in the overflow bin. The dashed line shows the DIS+γp Monte Carlo simulation double counting events with 4 GeV $< W_{\rm gen} <$ 8 GeV. (b) The distribution $\gamma_{\rm h}/\gamma_e$ is shown for data (full points) and Monte Carlo simulations (solid line). Events with badly reconstructed γ_h mainly appear in the overflow bin at a value of 3. (c) Distribution of $\log_{10}(y_{\rm JB})$ in data (points) and Monte Carlo simulation for events with $\gamma_{\rm h}/\gamma_e < 2$. Here, no double event counting is performed. The hatched histogram represents the simulated γp background.

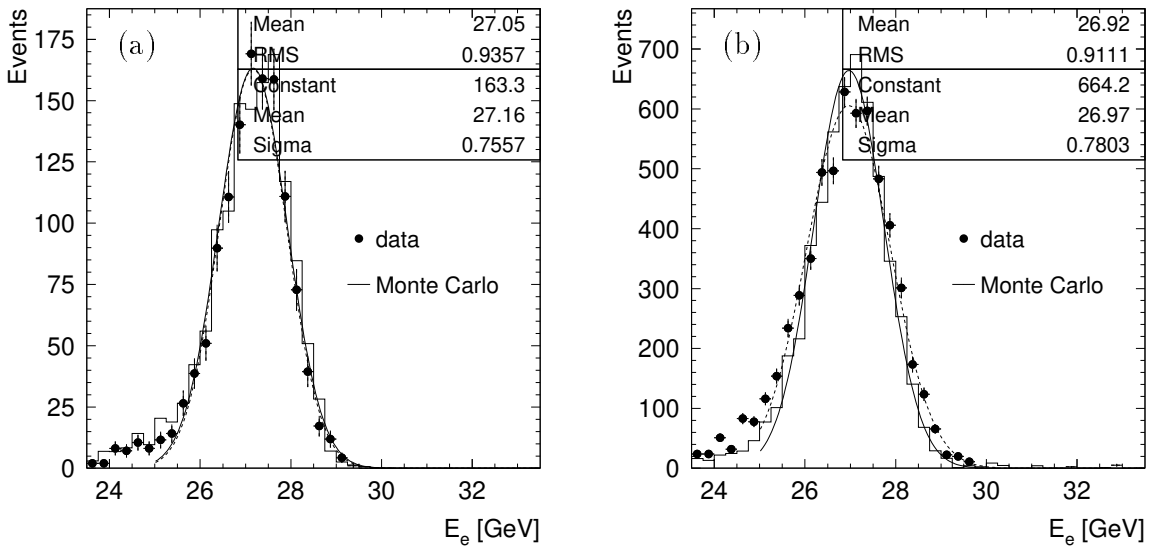

Figure 3.5: Comparison of the monochromatic electron energy distribution reconstructed for data (points) and Monte Carlo simulation (solid line) for two exemplary cells of the inner region of the Electromagnetic Spacal. Events are displayed if (a) cell number 39, (b) cell number 17 is the hottest cell of the cluster, respectively. Gaussian functions are fit separately to the data (dashed line) and to the Monte Carlo simulation (solid line) yielding to sets of fit parameters. The fit parameters displayed refer to the Monte Carlo simulation.

3.3.3 Calibration Procedure and Results

In the following the calibration procedure itself is described. Events are selected in the region of $0.005 < y_{\mathrm{JB}} < 0.05$. The requirement $y_{\mathrm{JB}} > 0.005$ is introduced in order to avoid the uncertainties of the Monte Carlo simulation in the limit of $y \to 0$. Background is rejected by demanding that the electron cluster radius be less than 3.3 cm (see section 2.3.4). The γ-criterion is not applied. Monte Carlo simulated events in the interval 4 GeV $< W_{\mathrm{gen}} <$ 8 GeV are doubly counted. A reconstructed vertex is not required due to lack of track chamber acceptance for events with small values of y.

The calibration is performed individually for the inner 144 cells of the Electromagnetic Spacal. In the outer part of the Spacal, at radii larger than 24 cm corresponding to the region of $Q^2 \gtrsim 10$ GeV, the number of available events per cell is too small[4] to perform a calibration cell by cell. In this region radial zones of 4 cm width, each segmented in four quadrants in the azimuthal angle ϕ, are calibrated in common. Each event is assigned to the hottest cell of the electron cluster as described in section 3.2. For each cell the maximum of the energy distribution in the data and in the Monte Carlo simulation is determined by a Gaussian fit in the interval between 25 GeV and 30 GeV

[4]The cross section decreases as $1/R^4$ while the number of cells increases with R^2, leading to a $1/R^6$ behavior of the number of events per cell.

yielding the correction factors. The procedure is iterated recalibrating the data in each iteration until the remaining corrections are smaller than 0.1%.

The detector resolution is determined from the calibrated data. The result is used to adjust the simulation of the detector resolution. In order to avoid a complete resimulation of the Monte Carlo events additional smearing corrections S_i are applied to the simulated cell energies. They are given by the relation

$$S_i = \sqrt{\sigma^2_{i,data} - \sigma^2_{i,MC}} \tag{3.4}$$

where σ_i denotes the measured width of the monochromatic energy distribution of cell i. Note that the simulated detector resolution can only be increased. S_i is set to zero if $\sigma^2_{i,data} < \sigma^2_{i,MC}$. $\sigma_{i,MC}$ amounts to 3%.

Fig. 3.5 depicts the fitted cluster energy distributions for data and Monte Carlo simulations for two cells. In (a) the distributions of data and Monte Carlo simulations show good agreement in the detector resolution, in (b) the simulation slightly underestimates the resolution. The captions display arithmetic mean and fitted maximum of both distributions. They agree to 0.5% or better. This shows that the result of the calibration is independent from the way the maximum is determined (see also below).

The result of the calibration is summarized in fig. 3.6. In (a) the position of the maximum of the energy distribution is shown for each of the inner 144 cells in the data and in the simulation. The fluctuations at small cell numbers of the central region of the Spacal correspond to cells of the Insert (first 16 cells, see fig. 2.7 in section 2.3.1) and the adjacent cells. Here, energy leakage into the beam pipe, inhomogeneities of the detector response (see section 3.5) and influences from the reduced size of the Insert cells lead to a variation of the averaged measured energy at the level of 1%. However, data and Monte Carlo simulations show the same behavior. The agreement is quantified in fig. 3.6(b) where the ratio of the data and the Monte Carlo simulation as a function of the cell number is shown. In the statistically rich inner region (at small cell numbers) Monte Carlo simulations and data agree to 0.5% or better. In fig. 3.6(c) the measured detector resolution is depicted. The corrections to the resolution are applied here, yielding good agreement between the data and Monte Carlo simulation on a cell-by-cell level. Disagreement mostly appears in cells where the resolution in data is smaller than of the simulated resolution of 3%. Here, the Monte Carlo simulation can not be adjusted properly. Note that the measured resolution only gives an upper limit to the intrinsic detector resolution. In order to exactly calculate the intrinsic detector resolution the distribution of the true electron energy must be taken into account. Fig. 3.6(d) illustrates the systematic uncertainty of the determination of the correction constants comparing between the position of the fitted maximum of the energy distribution and the arithmetic mean as a function of the cell number. Both methods agree very well showing the same dependence on the position as a function of the cell number. This provides additional confidence in the procedure. At large cell numbers the deviations become larger due to statistical fluctuations.

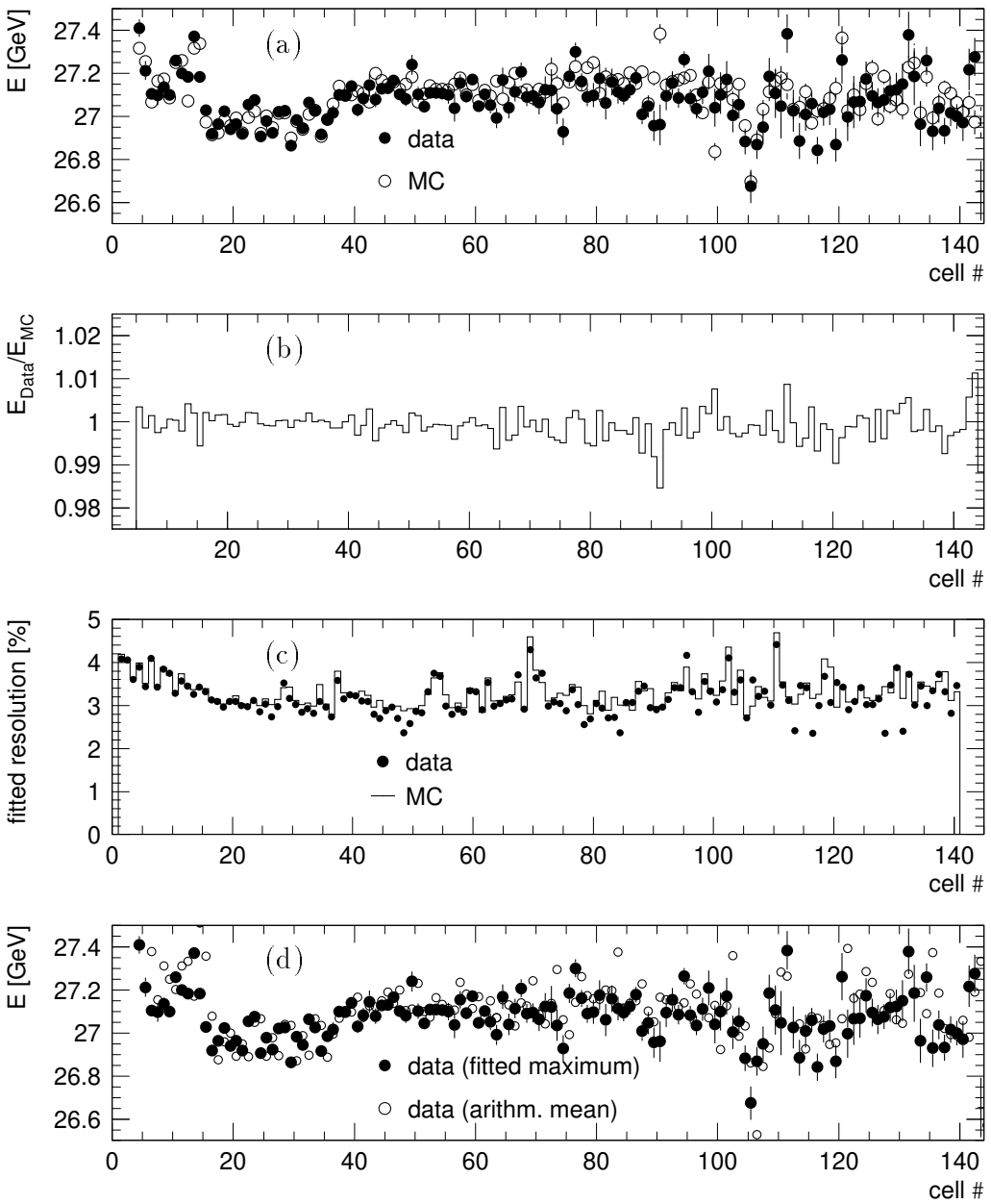

Figure 3.6: (a) The position of the maximum of the monochromatic peak as a function of the cell number for data (full points) and Monte Carlo simulations (open points). (b) Ratio between the values in data and in MC shown in (a). (c) Detector resolution for data (full points) and corrected MC (solid line). (d) Comparison between arithmetic mean (open points) and fitted maximum (full points) of the monochromatic peak extracted from the calibrated data.

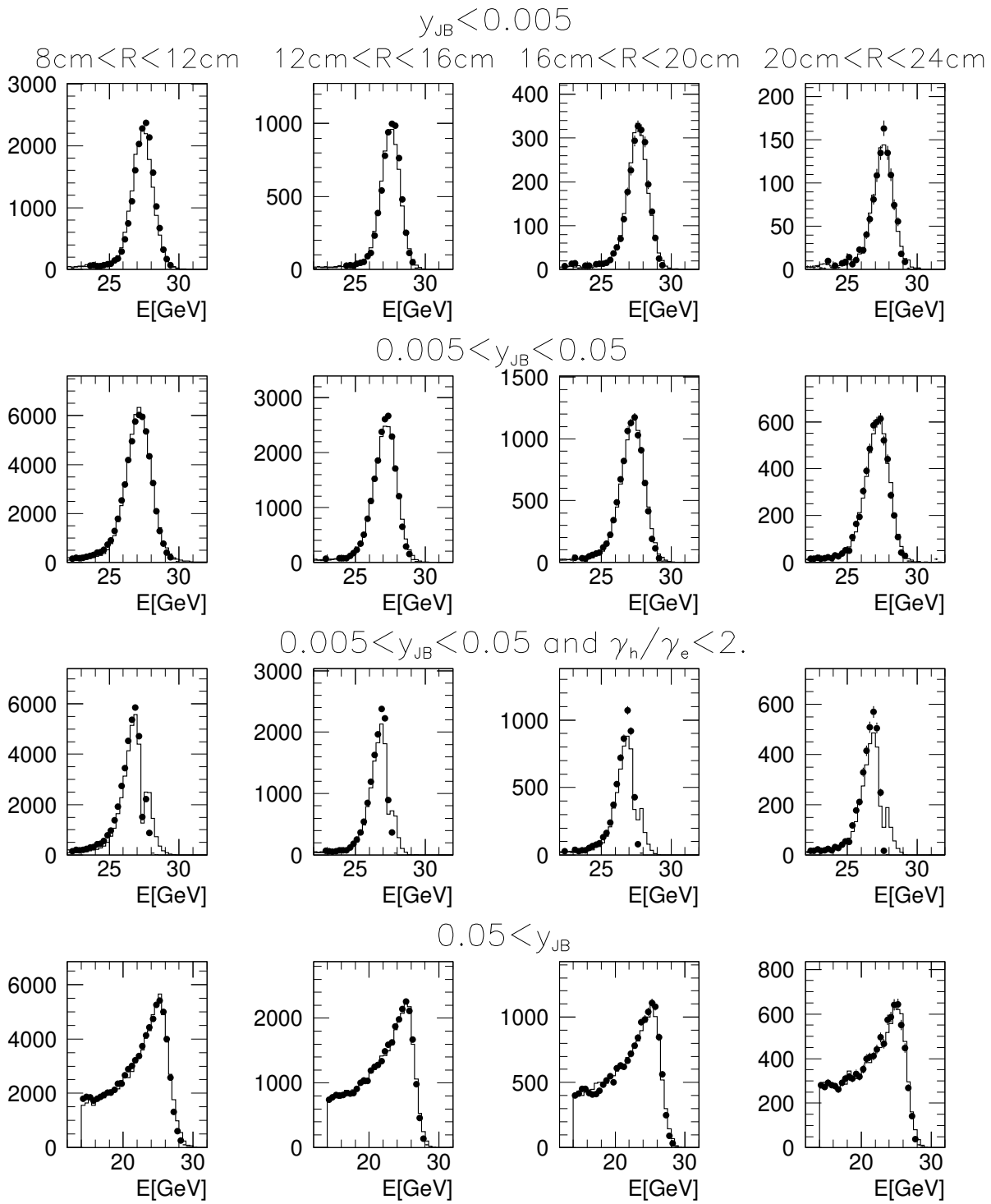

Figure 3.7: Electron energy spectra in Monte Carlo simulations (solid line) and data (points) are compared for four different regions of radius (columns) in different intervals of y_{JB} (rows).

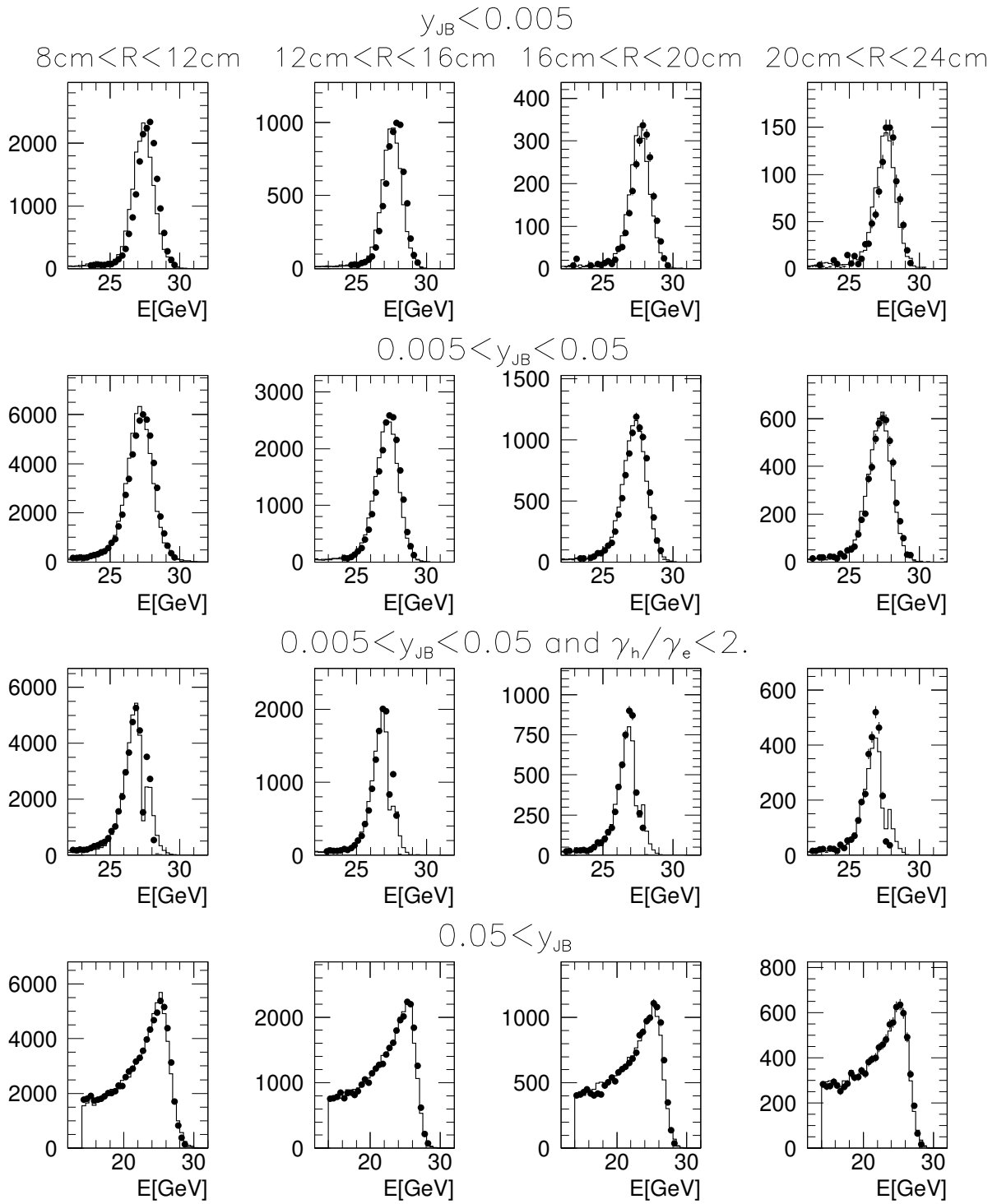

Figure 3.8: The reconstructed electron energies in the data (points) are globally increased by 0.7% relative to the standard calibration. The Monte Carlo simulation (solid line) is unchanged compared to fig. 3.7.

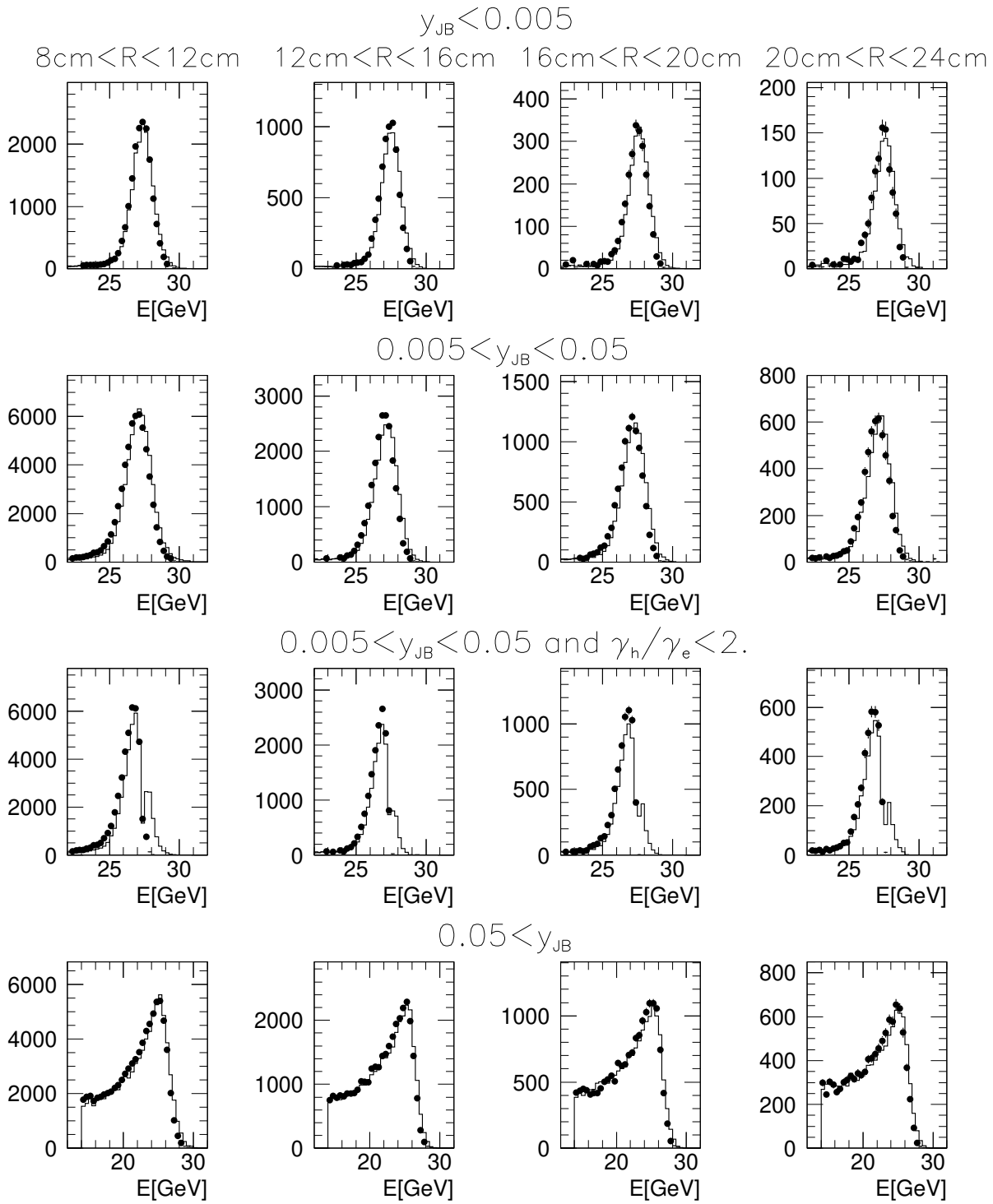

Figure 3.9: The reconstructed electron energies in the data (points) are globally decreased by 0.7% relative to the standard calibration. The Monte Carlo simulation (solid line) is unchanged compared to fig. 3.7.

So far, events with $0.005 < y_{\rm JB} < 0.05$ were selected for the calibration and used for the presentation of the results. In order to ensure that the calibration is valid for the entire kinematic region covered in the measurement of the structure function, the results will now be compared to other regions in y, separately for four different intervals of the impact radius of the scattered electron in the Spacal. Each row of fig. 3.7 refers to one interval of $y_{\rm JB}$ and each column to a region of 4 cm width of impact radius (8 cm to 12 cm, 12 cm to 16 cm, 16 cm to 20 cm and 20 cm to 24 cm, respectively). Monte Carlo simulations and data are normalized to the number of events in the given plot. The first row shows events at $y_{\rm JB} < 0.005$. Here one observes a small shift towards larger energies of the data relative to the Monte Carlo simulation. This shift can be explained by the lack of rate in the Monte Carlo simulation at very small values of y (see above section 3.3.2). The histograms in the second row contain events in the interval $0.005 < y_{\rm JB} < 0.05$. These events have been used for the calibration. It is thus natural that data and Monte Carlo simulations agree perfectly. The sensitivity of the calibration to the discrepancies between data and Monte Carlo simulations at small values of y (see fig. 3.4(a)) is investigated by selecting events from the same range of y, but imposing the γ-criterion $\gamma_{\rm h}/\gamma_e < 2$ in addition. The result is shown in the third row of fig. 3.7. Only the right edge of the distribution is affected by the selection cut. Overall, and in particular on the left side, data and Monte Carlo simulations agree reasonably well. This proves that the influence of the γ-criterion on the result of the calibration is small. In the fourth row events with $y_{\rm JB} > 0.05$ are shown. A subsample of these events, obtained by applying more restrictive selection cuts, is used for the determination of the structure function (see chapter 4). Data and Monte Carlo simulations agree very well.

The above investigations suggest a systematic uncertainty of the absolute energy scale at the level of 0.5% to 1%. In fact a value of 0.7% can be derived from the following study. A test of the sensitivity of the distributions shown in fig. 3.7 against a (possibly undetected) global shift of the energy scale is performed by varying the energies in the data by $\pm 0.7\%$. For fig. 3.8 and fig. 3.9 the scale in the data is increased by $+0.7\%$ and decreased by -0.7%, respectively. In both figures the distributions of the Monte Carlo simulations are unchanged compared to fig. 3.7. The clear deterioration of the agreement between data and Monte Carlo simulations in all radii and values of inelasticity compared to the standard calibration proves that the systematic uncertainty of the energy calibration is smaller than 0.7%. For events with $y_{\rm JB} > 0.05$ the deterioration is mainly visible at the right edge of the distributions. For shifted vertex data a systematic uncertainty of 1% has been achieved.

3.4 Double Angle Method

An independent check of the calibration is performed using the double angle method. In this method the expected electron energy E_{DA} is determined from the polar scattering angle θ_e of the electron and the polar angle $\gamma_{\rm h}$ of the current jet (see section 2.4).

The angle of the struck quark is correctly determined in events where the undetected fraction of transverse momentum of the hadronic final state is small. A large fraction of events at very small values of y does not satisfy this requirement and has to be rejected.
The most prominent properties of the double angle method are the following:

- It is, to first order, independent of the energy calibration since the kinematics is reconstructed using angles only.
- The ratio of the predicted to the measured electron energy E_{DA}/E'_e shows a peaked distribution (see fig. 3.11(b)) providing high sensitivity to the absolute energy scale.
- Since it is based on internal consistency between different detector components the double angle method is to first approximation independent of Monte Carlo simulations and thus of assumptions on the structure function. However, a high precision calibration can only be achieved with the help of the Monte Carlo simulation since the influences from the detector resolution and acceptance must be taken into account. A correct description of the hadronic final state is thus essential. Furthermore the dead material in the detector must be properly simulated. The calibration constant corrected by the Monte Carlo simulation is given as

$$c_{DA} = \langle E_e^{MC}/E_{DA}^{MC}\rangle / \langle E_e^{Data}/E_{DA}^{Data}\rangle. \tag{3.5}$$

- Towards very small and very large scattering angles of both the struck quark and the electron the resolution of the double angle method degrades (see section 2.4). At small values of Q^2 the double angle method is thus inferior to using monochromatic peak events for the extraction of calibration constants.

The measurement of the two polar angles of the electron and the hadronic final state is investigated comparing the calibrated data with the Monte Carlo simulation. Events are selected with $E_{DA} > 23$ GeV and $E'_e > 23$ GeV and a cluster radius of the scattered electron of less than 3.3 cm. Fig. 3.10(a) shows the averaged relative deviation $(E'_e - E_{DA})/E_{DA}$ of the calorimetric electron energy measured in the Spacal from the electron energy calculated by the double angle method as a function of the jet angle $\gamma_{\rm h}$. The dependence of the relative energy deviation on the measured jet angle in the data is reproduced by the Monte Carlo simulation at the level of 0.5%. The absolute size of the deviation of $\sim 1.5\%$ is due to the systematics of the double angle method. It indicates that the incident electron beam energy used for the calculation of E_{DA} is underestimated in both Monte Carlo simulations and data (see section 2.4). Events at low $\gamma_{\rm h} < 20^\circ$ suffer from the limitation of the detector acceptance at small polar angles (see section 2.2). At large angles, both data and Monte Carlo simulations show an increase of the average deviation of up to 3.5% at $\gamma_{\rm h} \gtrsim 150^\circ$ where the Spacal calorimeter is situated. In order to reduce these influences on the calibration, events are selected within a jet angle interval of $20^\circ < \gamma_{\rm h} < 140^\circ$.

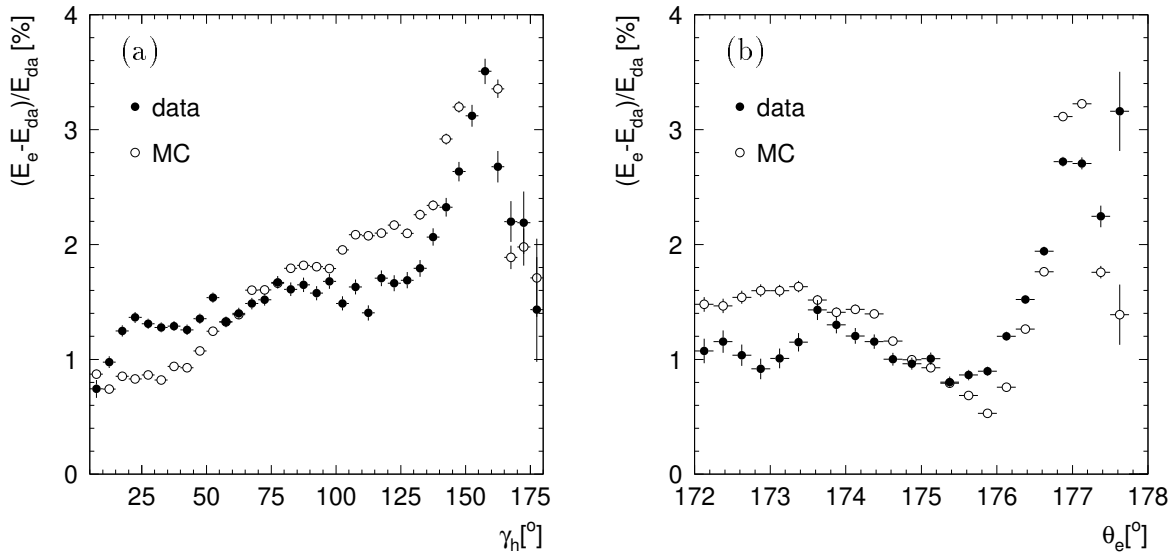

Figure 3.10: The average relative deviation $(E'_e - E_{DA})/E_{DA}$ as a function (a) of the jet angle $\gamma_{\rm h}$ and (b) of the electron angle θ_e for data (full points) and Monte Carlo simulations (open points). In (b) a cut on $20° < \gamma_{\rm h} < 140°$ is applied.

The selected events are used to investigate the dependence of $(E'_e - E_{DA})/E_{DA}$ on the polar angle of the scattered electron. Fig. 3.10(b) shows that the Monte Carlo simulation and the data behave very similarly. At angles above 176° a strong increase of $(E'_e - E_{DA})/E_{DA}$ is visible. It indicates a shift of the measured polar angle from the true value which is well reproduced in the Monte Carlo simulation.

In fig. 3.11 the ratio E'_e/E_{DA} is plotted, globally averaged over all cells in the data and in the Monte Carlo simulation. In (a) the scale is decreased by -0.7%, in (b) the default scale is used and in (c) the scale is increased by $+0.7\%$. The figures show clear sensitivity to the miscalibrations and thus confirm nicely the calibration obtained with the monochromatic peak electrons.

The agreement on cell level between the two methods is shown in fig. 3.12. In (a) the quantity E'_e/E_{DA} is compared for data and Monte Carlo simulation. Fig. 3.12(b) shows a direct comparison between the correction factors obtained by the monochromatic peak and by the double angle method. In (c) the ratio of the two sets of correction factors plotted in (b) is shown. It represents the degree of consistency between the two methods. While at small cell numbers both methods agree excellently, a small decrease is visible towards larger cell numbers indicating systematic discrepancies between the two methods at the level of 0.5% with a tail to -1%. Finally, (d) shows the projection of (c) onto the y-axis. The mean of the ratio quantifies the discrepancy of the two methods with respect to the absolute scale which proves to be negligible. The width, given in the figure as 'RMS', indicates that the uncertainty of the cell-by-cell calibration is of the order of 0.5%.

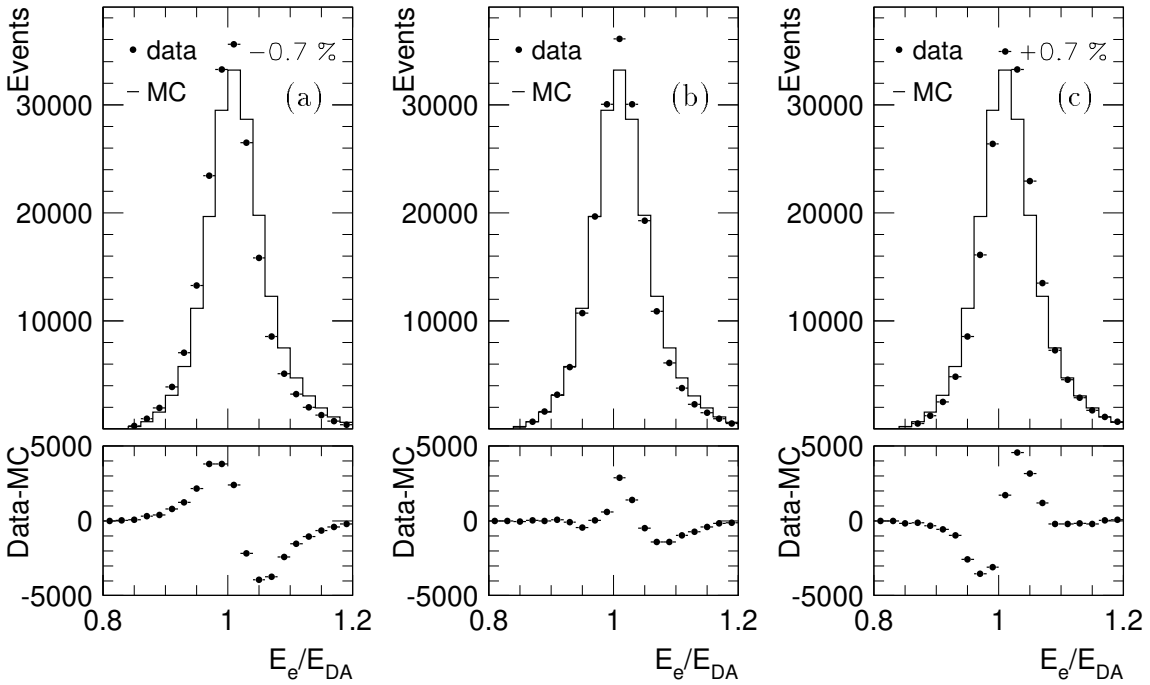

Figure 3.11: Distribution of the ratio between the electron energy measured in the Spacal and calculated via the double angle method E'_e/E_{DA}. The energy scale is varied for data (points) by (a) -0.7% (b) 0% (c) $+0.7\%$. The difference between the data and the simulation is shown in the small diagrams below.

The investigations presented so far have shown that the calibration has led to an uncertainty of the absolute energy scale of less than 0.7% for energies of the order of 27 GeV. This result is supported by the consistent results of two methods with different systematics. The intrinsic detector resolution was found to have an upper limit of 3% at 25 GeV. With the final calibration it is now possible to investigate the homogeneity of the detector, i.e. the spatial distribution of the detector response at distances smaller than the size of a cell, and the linearity, i.e. the accuracy of the detector response at lower energies.

3.5 Homogeneity and Linearity

As the result of the cell calibration the average response of the detector cells is equalized. However, inside a given cell and at cell borders, the response may still vary considerably, e.g. due to gaps without active detector material or due to damage of scintillation fibers in certain areas. An investigation of the homogeneity in the scale of millimeters in the central part of the Spacal was performed in [26] using scattered electrons of the shifted vertex data sample. Here, the results are briefly reported. Kinematic peak events were selected in bins of 5×5 mm^2 width using the center of gravity of the scattered electron

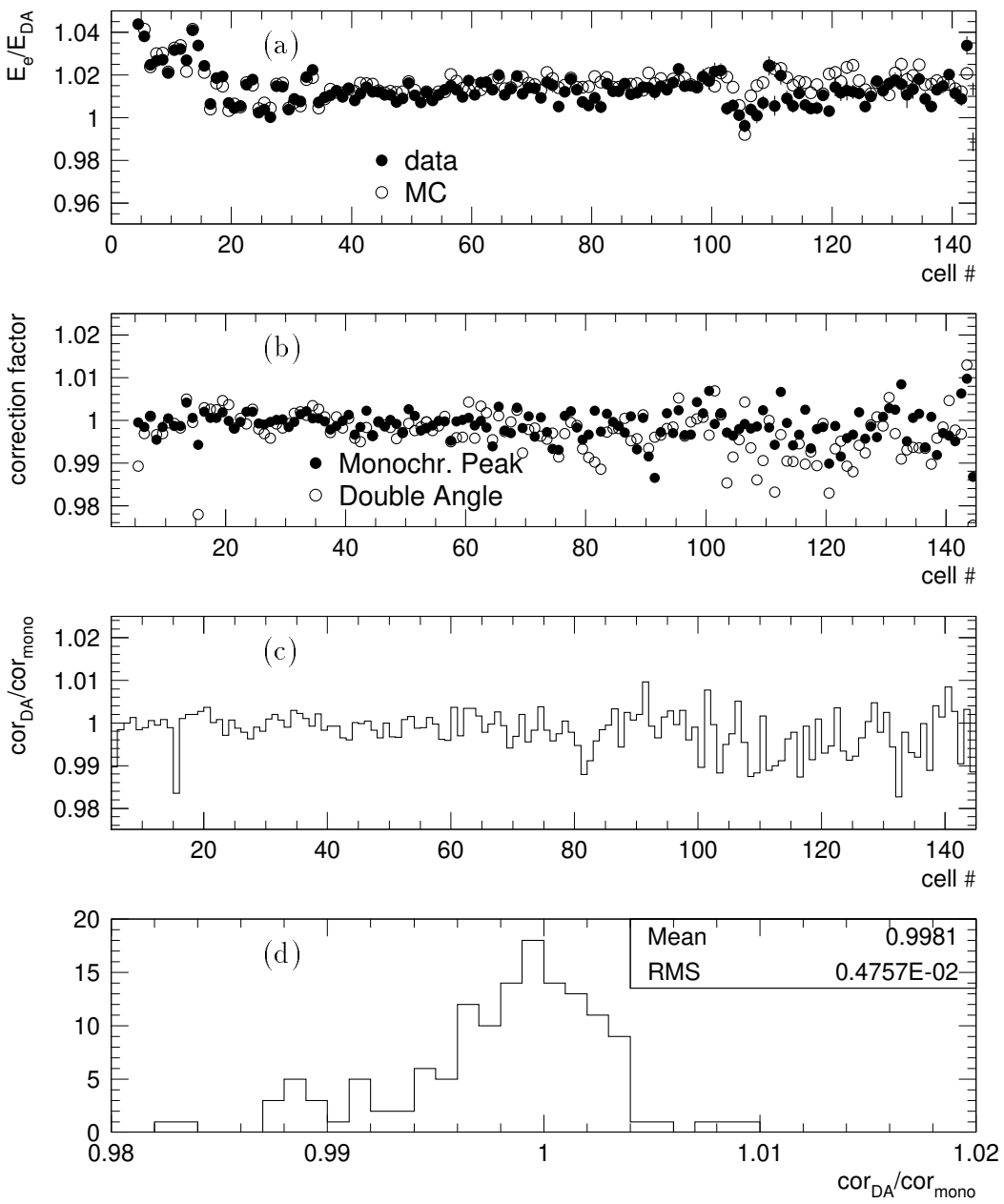

Figure 3.12: (a) The ratio E'_e/E_{DA} is shown for MC (open points) and data (full points) as a function of the number of the hottest cell. (b) Comparison between the correction factors obtained using the double angle method (open points) and the monochromatic peak method (full points). (c) the ratio of the two sets of correction factors shown in (b) as a function of the number of the hottest cell. (d) The projection of the ratio shown in (c).

cluster (see section 2.3.4). Inhomogeneities were generally found to be smaller than 2% increasing to the level of 3–4% at the border between the main body of the Spacal and the insert at values of x and y of ± 8 cm. The maximum inhomogeneity is localized in the insert and amounts to 7%. A prescription was developed which partially corrects the border region and the gaps between the quadrant modules of the insert. In this analysis the proposed corrections are applied.

Another important property to be studied is the relationship between the energy deposited and the energy measured in the Calorimeter. In the simplest case this is a linear relationship. In test beam measurements a maximum deviation from linearity of 1.3% was found for the Spacal [77]. An *in situ* measurement of the linearity was performed in [78] using QED Compton events (see section 4.9). Using the double angle method presented above, the two angles of the scattered electron-photon-system were used to predict the energies of the electron and the photon. The data showed a maximum deviation $(E_{DA} - E_{cl})/E_{cl}$ of about -6% between the calculated double angle energy and the energy measured in the Spacal at a cluster energy of 8 GeV. The corresponding value found in the Monte Carlo simulation is -4% reflecting known systematic influences, e.g. from the reconstruction of the angles as well as the dead material in the detector. Relevant to the structure function analysis is the difference between the data and the Monte Carlo simulation since it adds to the uncertainty of the energy scale. For the measurement of the structure function (described in the following chapter 4) an uncertainty of the absolute energy scale of 2.5% at 8 GeV (7 GeV) and 0.7% (1%) at 27.5 GeV, with a linear interpolation between the minimum and maximum energies, is assumed for nominal (shifted) vertex data, respectively.

3.6 Energy Calibration of the Spacal for Hadrons

While electromagnetic showers develop by virtue of bremsstrahlung and pair production processes, hadronic showers are dominated by the strong interactions between hadronic shower particles and the nuclei of the detector material. As a consequence the fraction of visible energy, i.e. the amount of energy detected in the calorimeter relative to the energy of the incident particle, is different for hadronic and electromagnetic showers. Typically the detector response to hadrons is smaller than for electrons ($\pi^{\pm}/e \sim 70\%$). The aim is to measure the true energy deposited in each cell as precisely as possible. Therefore electromagnetic and hadronic signals are treated differently. For the Spacal the hadronic energy corrections were initially estimated in a Monte Carlo study yielding values of 1.1 (1.3) for the Electromagnetic (Hadronic) Spacal, respectively [79]. The corrections are applied to the energy of all cells outside the cluster of the electron candidate for both Monte Carlo simulations and data providing the starting point of the following investigations.

The relative calibration of the cells of the Hadronic Spacal, as well as a large part of the Electromagnetic Spacal (at radii $r > 35$ cm) was performed using cosmic muon data. A detailed description of the data acquisition and the event selection of cosmic muons

may be found in [72]. While the resulting uncertainty of the relative cell calibration is less than 5% the uncertainty on the absolute energy scale is large. In fact for reasons poorly understood the measured detector response to cosmic muons in the Spacal differs considerably from the expectation. In the Electromagnetic Spacal the absolute scale is known from kinematic peak events. The cosmic muons were used to transfer the knowledge of the absolute scale to the outer region. For the Hadronic Spacal a different strategy must be used.

The energy scale of the Spacal is determined using the measured hadronic energy flow in ep DIS events. Energy scale corrections are applied to Spacal cells which do not belong to the electromagnetic cluster of the selected electron candidate (see section 4.1). The energy in a given cell is not taken into account if the corrected cell energy is below the noise cut of 50 MeV. Hadronic energy flow in the backward region of the H1 detector originates from events of large inelasticity y. Here, events with $y_e > 0.55$ are selected in order to enhance the average hadronic energy deposited in the Spacal. Note that y_e is independent of the hadronic energy scale. In fig. 3.13(a) the hadronic energy flow in both Hadronic and Electromagnetic Spacal is shown. Fig. 3.13(b) shows the total energy in the Hadronic Spacal only. Reasonable agreement between data and Monte Carlo simulation in the energy scale is found after adjustment of the data to the Monte Carlo expectation in the following way: The energies in the cells of the Hadronic Spacal are multiplied with a correction factor of 0.7 and, in addition, the hadronic energies in both Electromagnetic and Hadronic Spacal are multiplied by a factor of 1.07.

Fig. 3.13(a) shows that at small energies and also at large energies the data overshoot the Monte Carlo simulation. This effect can not be traced back to the energy calibration but rather indicates discrepancies in the description of the hadronic final state in the Monte Carlo simulation[5].

The absolute energy scale is determined demanding that the inelasticity measured with the hadronic final state y_{JB} be on average balanced with y_e as reconstructed from the scattered electron, i.e. $\langle y_{\mathrm{JB}}/y_e \rangle = 1$. For the structure function measurement this requirement is particularly important not only because the event kinematics must be consistently described between different reconstruction methods but also because the event selection exploits the hadronic final state rejecting events at $E - p_z < 35$ GeV (see section 4.6). The relation between y_{JB} and y_e is investigated in fig. 3.14(a) for events at $y_{\mathrm{JB}} > 0.05$ and $y_e < 0.73$. The correlation between y_{JB} and y_e is visualized by the contour lines. The plot shows that the ratio y_{JB}/y_e is constant independently of the selected region of y. It can thus be used to determine the absolute scale of hadronic

[5]There are indications that at high y the Monte Carlo simulation underestimates the energy flow in the backward region but slightly overestimates the hadronic energy measured in the Liquid Argon calorimeter (see also fig. 4.19(c) and (d) in section 4.10). A possible explanation for the excess of the Monte Carlo simulation at small energies is that the generator DJANGO does not simulate processes in which the exchanged virtual photon is resolved. In resolved processes measured in the data a 'photon remnant' jet is formed in the backward region increasing the energy flow in the data in comparison to the Monte Carlo simulation [68].

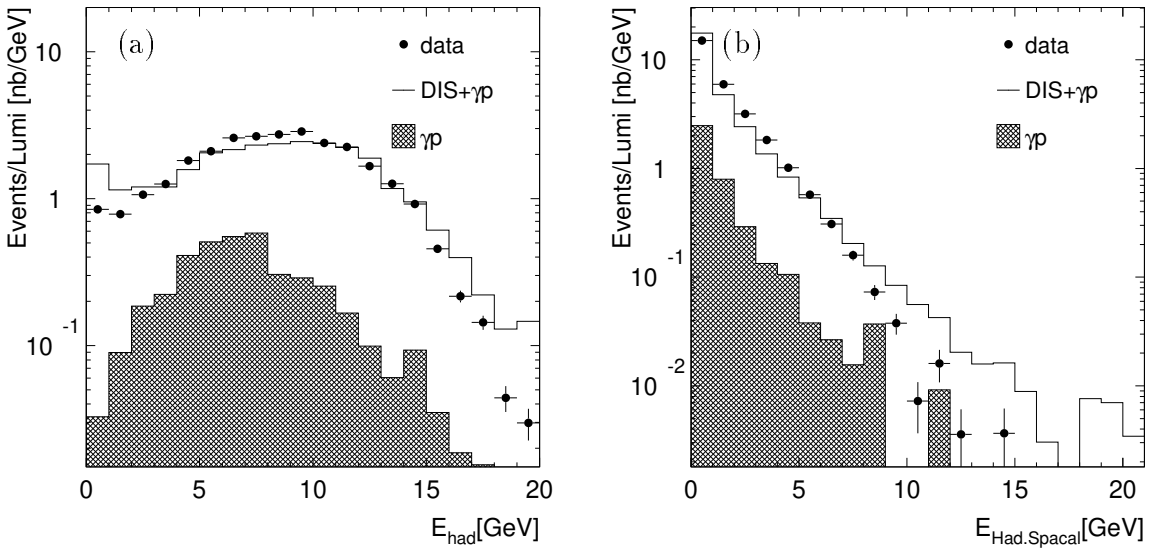

Figure 3.13: Hadronic energy flow, (a) in both Hadronic and Electromagnetic Spacal and (b) in the Hadronic Spacal for data (points) and DIS+γp Monte Carlo simulation (solid line). The hatched histogram shows the simulated contribution from photoproduction background.

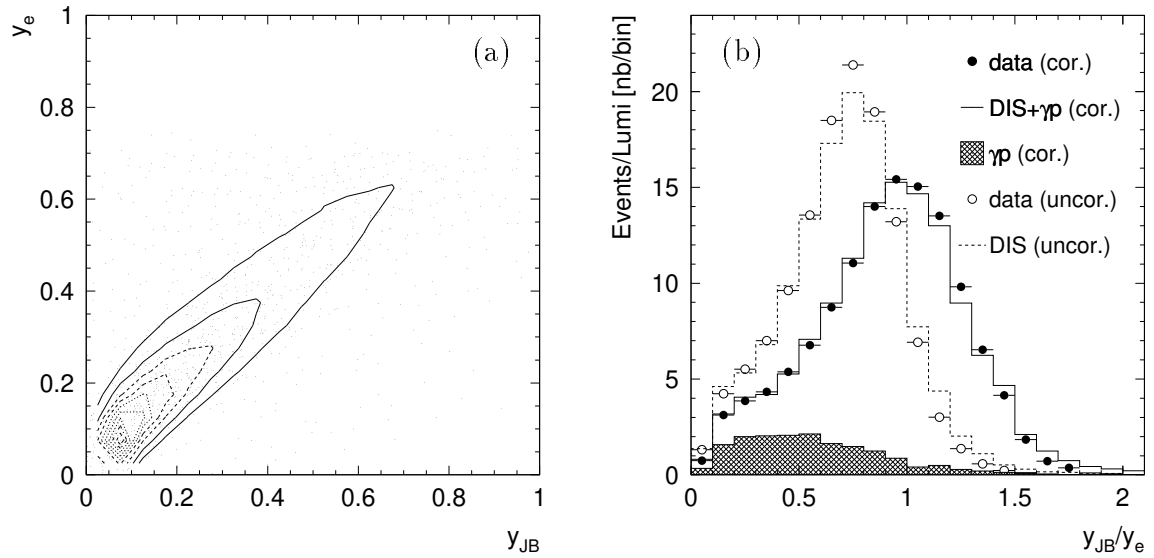

Figure 3.14: (a) Data are used to plot $y_{\rm JB}$versus y_e. The contour lines indicate the correlation. For the calculation of $y_{\rm JB}$ hadronic energies in the Spacal are multiplied by a factor of 1.5 according to the findings below (see text). (b) The ratio $y_{\rm JB}/y_e$ is plotted before (open points, dashed line) and after (full points, solid line) the correction for data and Monte Carlo simulation, respectively.

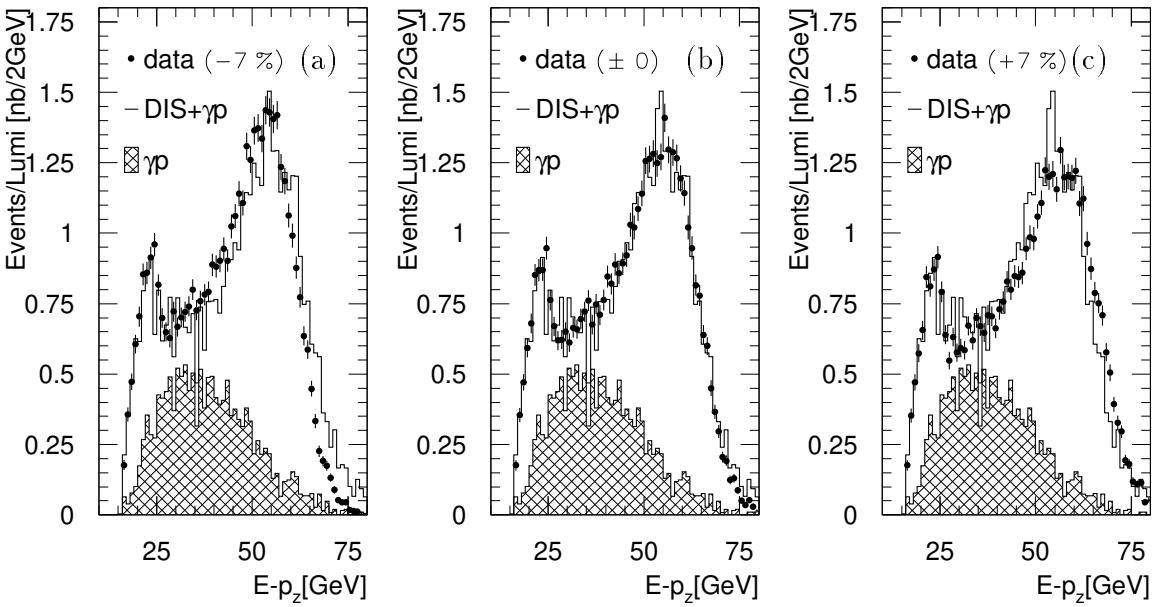

Figure 3.15: The systematic error of the hadronic energy calibration in the Spacal is determined using the $E - p_z$ distribution for events with $y_e > 0.55$. The hadronic energy scale in the data (points) is varied by $\pm 7\%$. In (a) the energy is reduced for data by 7%. In (b) the data are unchanged and in (c) the energy is increased by 7%. Also shown are the DIS+γp Monte Carlo simulation (solid line) and the simulated γp Background.

energies in the Spacal selecting events with $y_e > 0.3$. In fig. 3.14(b) the distribution y_{JB}/y_e is shown before and after application of a correction factor. The uncorrected distribution has a maximum at about 0.7. The corrected distribution is obtained by applying a correction factor of 1.5 to the energy of the hadronic final state measured in the Spacal for both data and Monte Carlo simulation.

The correction accommodates different effects which are not yet quantitatively disentangled. Apparently the corrections of 1.1 (1.3) for the Electromagnetic (Hadronic) Spacal (see above) were underestimated. In addition to discrepancies in the simulated Spacal response to hadrons, also energy leakage, i.e. the incomplete containment of hadronic showers in the Spacal may play a role. A quantitative investigation of these effects has been performed only in test beam measurements [39]. As further possibly contributing influences loss of energy in the dead material in front of the detector and the relatively large noise cut of 50 MeV should also be mentioned here.

The uncertainty of the absolute energy scale for hadrons in the Spacal is estimated varying of the hadronic energies measured in the Spacal in the data by $\pm 7\%$. A suitable quantity for this test is $E - p_z$ since it has a comparably sharp distribution. Events with $y_e > 0.55$ are selected. The three distributions of $E - p_z$ obtained with this sample for different hadronic energy scales are depicted in fig. 3.15. In (a) the hadronic energy in the Spacal is reduced by 7% in the data, in (b) it is unchanged and in (c) the hadronic energy in the data is increased by 7%. The variations lead to clear

discrepancies between the Monte Carlo simulation and the data. From this it can be concluded that the systematic uncertainty on the hadronic energy scale in the Spacal is smaller than 7%.

3.7 Summary

The results of the calibration presented in this chapter are summarized as follows.

- A precise calibration of the electron energy was achieved by the use of electrons in the kinematic peak. The position and the shape of the kinematic peak measured in the calorimeter is predicted with sufficient precision by Monte Carlo simulations.
- The determination of the correction factors for each cell follows the prescription of the method of the hottest cell in which the full electron cluster energy correction is assigned to the hottest cell of the cluster.
- A calibration of high precision is performed using events in the monochromatic peak. In this method kinematic peak events are selected with the additional requirement $y_{\mathrm{JB}} < 0.05$. The systematic uncertainty on the resulting energy scale is less than 0.7%. For shifted vertex data a value of 1% has been achieved. The upper limit of the detector resolution at 27 GeV is 3%.
- The result of the calibration is cross checked using the double angle method yielding additional confidence in the above results.
- Studies of the homogeneity and the linearity are reported. The homogeneity in the inner part of the Spacal is found to be better than 2% except at the border to the Insert. Using QED Compton events the linearity is proven to be better than 2.5% at particle energies of 8 GeV.
- The hadronic energy scale of the Spacal is calibrated. The relative calibration of the cells was performed using cosmic muon data. The absolute scale of the data is determined using the hadronic energy flow in data and in Monte Carlo simulated events imposing consistency requirements between the different reconstruction methods. For the measurement of the hadronic final state in the Spacal a correction factor of 1.5 is found. The uncertainty on the absolute energy scale of hadrons in the Spacal is estimated to be less than 7%.

A quantitative discussion of the impact of a potential miscalibration of the energy scale on the measurement of the structure function $F_2(x, Q^2)$ will be given in section 5.2.

Chapter 4

Data Selection

The measurement of the structure function F_2 involves the determination of the double differential ep cross section as a function of x and Q^2. One of the main issues of the measurement, therefore, is the selection of events in deep inelastic scattering and the reconstruction of the event kinematics. For this purpose it is essential to identify the scattered electron in the detector and to precisely measure its energy and its scattering angle. Furthermore, it is necessary to determine the efficiencies of the trigger and of the event selection.

The chapter is organized as follows: In section 4.1 the method used in the present analysis to extract the structure function from the data is described. A brief outline of the DIS event selection criteria is given in section 4.2. In section 4.3 the run selection criteria used to define the analyzed data set are described. A suitable set of event triggers is selected and their efficiency and integrated luminosity is calculated (section 4.4). The DIS event selection cuts are presented in detail in the sections 4.5, 4.6 and 4.7. The main background source, given by small angle ep scattering (photoproduction), is investigated in section 4.8. In section 4.9 the influence of radiative corrections is discussed. Monte Carlo simulation and data are compared for events with QED final state radiation. Finally, the kinematic distributions are shown in section 4.10. The results will be presented in chapter 5.

4.1 Extraction Method of F_2

As described in section 1.2 the structure function F_2 of the proton is defined with respect to the double differential Born cross section. The Born cross section describes ep scattering in the single photon exchange approximation to lowest order in α where α is the electromagnetic coupling constant. Following equation (1.12) F_2 is determined via the measurement of the Born cross section. However, the measured events comprise contributions to all orders in α and the Born cross section is thus not directly accessible experimentally. Particularly large corrections originate from bremsstrahlung processes

of real photons from the incident electron. A description of the most relevant radiative processes is given in section 4.9.

Expressing the radiative corrections as $\delta_{RC}(x, Q^2)$ the relation between the measured cross section and F_2 can be written as

$$\frac{d^2\sigma}{dxdQ^2} = \kappa(R) \cdot F_2(x, Q^2) \cdot (1 + \delta_{RC}(x, Q^2)) \tag{4.1}$$

with the so-called kinematic factor

$$\kappa(R) = \frac{2\pi\alpha^2}{Q^4 x}\left(2(1-y) + \frac{y^2}{1+R}\right). \tag{4.2}$$

In addition to containing kinematic terms κ depends on $R = F_L/F_2 - F_L$, i.e. the ratio between the cross sections of longitudinally and transversely polarized photons as defined in section 1.2 by equation (1.19). F_L has not yet been directly measured in the HERA regime. It has, however, been shown recently [80] that the QCD model of F_L according to [20, 81] is consistent with the data[1]. In this analysis the F_L model by Badelek, Kwiecinski and Stasto (BKS) [82] is used to extract F_2 from the measured cross section. The model is based on the photon-gluon fusion process and has the proper limit for $Q^2 \to 0$ where F_L should vanish as Q^4. It predicts values of R between 0.2 and 0.3 in the measured kinematic region (see also table 5.1). Equation (1.12) shows that the sensitivity of the cross section to F_L is kinematically suppressed with y^2. At low $y \lesssim 0.35$ the effect of F_L on the extracted value of F_2 is therefore negligible. It does not exceed $\sim 10\%$ anywhere in the kinematic range so far explored at HERA.

The measurement of the double differential cross section is performed in bins of x and Q^2, denoted as $\square_{x,Q^2}$ in the following. The uncorrected bin integrated cross section is obtained from the number of events $\tilde{N}$ reconstructed in this bin normalized to the integrated luminosity $\mathcal{L}$,

$$\tilde{\sigma}_{\square_{x,Q^2}} = \int_{\square_{x,Q^2}} \frac{d^2\sigma(x, Q^2)}{dxdQ^2} dxdQ^2 = \frac{\tilde{N}}{\mathcal{L}}. \tag{4.3}$$

From this the Born cross section is extracted by applying a set of corrections.

- First of all, background is subtracted. The main background sources of the measurement are photoproduction processes, where the scattered electron escapes through the beam pipe and part of the hadronic final state is misidentified as the scattered electron.
- The effect of the finite detector resolution on the measurement of the angles and energies of the scattered particles is taken into account by the acceptance correction A.

[1] For a direct measurement of F_L it is necessary to disentangle the contributions from F_2 and F_L to the cross section using measurements of the cross section at different ep center of mass energies.

- Loss or gain of events due to the behavior of the trigger and the event selection cuts is calculated (ϵ).
- Finally, the radiative corrections δ_{RC} are applied.

The Born cross section integrated over the given bin is then

$$\sigma_{\square_{x,Q^2}} = \frac{N_{data} - N_{bg}}{\mathcal{L}} \frac{1}{A \cdot \epsilon} \frac{1}{(1+\delta_{RC})}. \tag{4.4}$$

To obtain the differential cross section at a chosen point in x and Q^2 rather than a bin integrated value the bin size and the cross section behavior inside the bin is taken into account. The bin size correction transforms the integrated cross section into a bin averaged cross section. Application of the bin center correction yields the cross section at the chosen central values (x_c, Q_c^2) of the bin. The bin center correction is important since the cross section typically varies considerably inside a given bin. The two corrections are contained in the following relation:

$$c_{bc} = \frac{\frac{d^2\sigma(x,Q^2)}{dxdQ^2}|_{x=x_c,Q^2=Q_c^2}}{\int_{\square} \frac{d^2\sigma(x,Q^2)}{dxdQ^2} dxdQ^2}. \tag{4.5}$$

In order to obtain F_2 from the double differential Born cross section the values of R are assumed. The BKS model [82] (see above) used in this analysis predicts values of R between 0.2 and 0.3 in the measured region (see also table 5.1).

Monte Carlo simulations are used to estimate the background and to perform the acceptance corrections. Deep inelastic ep scattering events are simulated using the Monte Carlo generator DJANGO which includes first order radiative processes (see section 2.5). The detector simulation of DJANGO events thus contains the acceptance corrections for both the detector resolutions and the radiative processes. The photoproduction background is estimated using the generator PHOJET (see section 2.5).

Provided that the Monte Carlo simulations correctly reproduce the data the complete measurement of F_2 can be compactly accommodated in the following relation:

$$F_2(x_c, Q_c^2) = \frac{N_{data}(\square_{x,Q^2}) - N_{bg}(\square_{x,Q^2})}{N_{MC}(\square_{x,Q^2})} \frac{\mathcal{L}_{MC}}{\mathcal{L}_{data}} \cdot F_2^{MC}(x_c, Q_c^2) \tag{4.6}$$

N_{MC} is the number of DIS events in the Monte Carlo simulation for the integrated luminosity, the simulated cross section is given by $N_{MC}/\mathcal{L}_{MC}$. Note that both R and the bin center correction enter the formula in the relation between F_2^{MC} given at the central values (x_c, Q_c^2) and the expected number of events $N_{MC}(\square_{x,Q^2})$, proportional to the bin averaged cross section used in the Monte Carlo simulation.

The measurement is performed in an iterative procedure: For the first iteration the behavior of F_2^{MC} is assumed. The choice of a realistic behavior is preferable but not

necessary. F_2 is then measured using equation (4.6) by iteratively adjusting F_2^{MC}. In order to avoid the repeated simulation of events, the Monte Carlo simulated events are reweighted corresponding to the measured cross section in each step of the iterations. The final result of F_2 is obtained with a Monte Carlo simulation tuned to describe the data in all aspects. In this analysis the parametrization of the global QCD fit to H1 data recorded in 1994 and results from previous experiments with $Q^2 \geq 5$ GeV^2 is used [15] (see section 1.4).

It should be emphasized that the use of the above relation (4.6) is justified only if the Monte Carlo simulation reproduces the data with respect to detector acceptance and efficiency to good precision. One of the main issues of the analysis, therefore, is to thoroughly compare the Monte Carlo simulation with the data and to prove good consistency. In this analysis discrepancies between the data and the Monte Carlo simulation are revealed in various respects. Most of them are traced back to inaccuracies of the simulation of the new detector components Spacal and BDC. The discrepancies are corrected where possible and assigned a systematic error otherwise.

The event selection criteria follow the aim of minimizing the systematic uncertainties of the measurement. In general, two conditions must be fulfilled, namely a minimum loss of good events and a maximum background rejection. A sketch of the event selection criteria is given in the following.

4.2 Outline of the Event Selection

In this section an outline of the event selection criteria used in the present analysis is given. The cuts are listed in table 4.1. The present analysis is based on data recorded in 1995 with nominal z-position of the ep interaction point (nominal vertex data). As mentioned in section 1.5 in the same year a set of data was recorded in which the z-position of the ep interaction point was shifted by +70 cm (shifted vertex data). The latter data were analyzed and the results have been published [25]. In the following and throughout this chapter the shifted vertex data analysis is mentioned in parentheses where substantially different from the present analysis.

- The event selection is based on the identification of the scattered electron. The electromagnetic cluster in the Spacal with the highest energy deposit is selected as the electron candidate. The minimum energy required for the electron candidate is 8 GeV (7 GeV). The time of flight of electron candidates in the Spacal lies within the interaction time window of 8.5 ns $< t <$ 16.5 ns (12.5 ns $< t <$ 22.5 ns).

- The lateral size of the electron candidate, described by the cluster radius R_{cl}, is less than 3.5 cm. The longitudinal size of the shower, estimated using the energy $E_{e,had}$ in the Hadronic Spacal behind the electron candidate, is smaller than 0.5 GeV. Energy leakage into the beam pipe is suppressed by a cut on the energy in the Spacal veto layer of $E_{veto} < 1$ GeV.

cut #	Nominal Vertex Data (present analysis)	Shifted Vertex Data
1	$E'_e > 8$ GeV	$E'_e > 7$ GeV
2	8.5 ns $< t <$ 16.5 ns	12.5 ns $< t <$ 22.5 ns
3	$R_{cl} < 3.5$ cm	
4	$E_{e,had} < 0.5$ GeV	
5	$E_{veto} < 1$ GeV	
6	$\lvert\Delta R\rvert < 2$ cm	
7	$\lvert R\Delta\phi\rvert < 2.5$ cm	
8	$R_\theta > 8.7$ cm	
9	$E - p_z < 35$ GeV	
10	$\exists$ reconstructed vertex	
11	-30 cm $< z_{\rm vtx} < 30$ cm	40 cm $< z_{\rm vtx} <$ 100 cm

Table 4.1: The DIS event selection cuts used in the two analyses with 1995 data.

- At least one reconstructed track is found in the BDC within a distance to the electron candidate in the Spacal of less than 2 cm in radial and 2.5 cm in azimuthal direction. The BDC track closest to the electron candidate is selected as the electron track and used for the polar electron scattering angle θ_e. Events with a radial impact point R_θ of the scattered electron in the Spacal of less than 8.7 cm distance from the beam axis are rejected.

- Events are rejected if the global quantity $E - p_z < 35$ GeV (equation (2.5)). This cut suppresses photoproduction background and reduces the influence of QED initial state radiation.

- Each selected event has a reconstructed vertex with a z-position within ± 30 cm of the nominal interaction point, i.e. between -30 cm and $+30$ cm (40 cm and 100 cm) for the nominal (shifted) vertex data, respectively.

4.3 Run Selection

Full functionality of the detector must be guaranteed for the set of data used in the analysis in order to achieve high precision for the measurement. Investigations have shown that in 1995 only the data recorded after the 20th of October safely fulfill the quality requirements. Before this date various hardware problems, connected with the new installation of the backward detector components BDC and Spacal (e.g. trigger inefficiencies and spurious read out errors [83]), lead to cross section uncertainties at the 5% level, too large for the analysis presented here. Runs recorded between 20th of

October 1995 and the end of the 1995 run period (27th of November 1995) are selected. In addition the following run selection criteria are imposed:

- **HV alarm bits:** All relevant components of the central detector, i.e. the inner tracking chambers CJC1 and CIZ, the BDC, the Luminosity System, the Time-of-Flight counters and the Spacal and Liquid Argon calorimeters must be operational. A given run is rejected if at least one of the HV alarm bits is on for more than 5% (50%) of the integrated luminosity recorded in this run in the nominal (shifted) vertex data analysis respectively. For accepted runs the luminosity is corrected accordingly.

- **Events per luminosity:** It is demanded that the integrated luminosity within a run be larger than 0.2 nb^{-1} in order to guarantee statistical significance. The number of selected events in each run must be approximately proportional to the luminosity. A run is accepted if the number of good events does not deviate significantly (more than 4σ, where σ denotes the statistical error of the number of events in the given run) from the overall averaged number of events per luminosity. This criterion mainly ensures the continuous functionality of the event trigger.

- **Stability of the energy response:** The mean energy of the electron candidates within each run must be within 1σ of the global average.

- **Beam tilts:** The beam coordinates and the inclination of the beam axis relative to the H1 coordinate system defined by the central jet chamber CJC1 are calculated for each run separately using the distribution of event vertices measured with the CJC. For the shifted vertex data runs are rejected where the difference from the mean beam tilt is large, i.e. if $x'_{\mathrm{beam}} < -0.0008$ or $y'_{\mathrm{beam}} < -0.0006$ or $y'_{\mathrm{beam}} > 0.0016$. No cut is imposed in the analysis of the nominal vertex data.

4.4 DIS Trigger Selection

The H1 trigger system is described in section 2.2. In many runs the DIS event triggers are considerably prescaled. The effective integrated luminosity collected with a given trigger is thus reduced. The subtriggers used in this analysis are listed in table 4.2. In column 2 of the table the subtrigger definitions are given. For each of the subtriggers a minimum energy deposit in the Spacal is required. IET>0, IET>1 and IET>2 refer to different thresholds of the Spacal IET trigger, providing full trigger efficiency at 5 GeV, 8 GeV and $\sim$ 23 GeV, respectively [46]. The IET Spacal Trigger is described in section 2.3.3. $s6$, $s7$ and $s2$ demand a coincidence between the IET trigger and a combination of vertex trigger conditions, abbreviated here as $t_{0,\mathrm{vtx}}$. $s7$ and $s2$ ask in addition for the absence of the RZ_{veto} signal. The RZ_{veto} is based on fast histogramming of hits in the z-chambers CIZ and COZ. It gives an estimate of the z-position of the event vertex. Events with too many tracks pointing outside the interaction region

Subtrigger		Nominal Vertex Data				Shifted Vertex Data			
		Prescales		Lumi	W	Prescales		Lumi	W
		min	max	nb^{-1}		min	max	nb^{-1}	
$s2$	$IET > 1 \cdot t_{0,vtx} \cdot \neg RZ_{veto}$	1	11	565.2	1.0	1	1	115.8	(1.0)
$s3$	$IET > 2$	1	4	266.7	2.1	1	1	115.8	(1.0)
$s0$	$IET > 1$	1	30	108.8	5.2	1	1	115.8	1.0
$s5$	$IET > 0$	50	> 9999	4.9	(115.3)	1	201	41.7	2.8
$s6$	$IET > 0 \cdot t_{0,vtx}$	4	5001	10.2	(55.5)	1	101	77.8	(1.5)
$s7$	$IET > 0 \cdot t_{0,vtx} \cdot \neg RZ_{veto}$	4	> 9999	56.9	(9.9)	1	21	105.9	1.1

Table 4.2: Table of DIS subtriggers used for the nominal and shifted vertex data analysis. Column 2 shows the subtrigger definitions (see text). The minimum and maximum occurring prescales and the effective integrated luminosity recorded with the respective subtrigger including prescales are listed in columns 3 to 5, and 7 to 9. In columns 6 and 10 the event weights (W) used in the trigger selection scheme are listed (see text). Subtriggers with weight values in parentheses are not used for the analysis. The luminosity values include the correction for the rejection of proton satellite events of 3.6% (4.6%) for the nominal (shifted) vertex data.

are rejected. In addition to the intrinsic ToF condition of the Spacal IET trigger, all subtriggers require the absence of out-of-time background signals. This condition is realized using a background veto signal from the ToF counters FToF, PToF and BToF and the Veto Wall (see section 2.2). Columns 3,4 (7,8) of table 4.2 give an overview over the prescales imposed on the different subtriggers. The collected luminosity for each subtrigger after correction of prescales and subtraction of satellite bunch contributions is listed in columns 5 (9).

4.4.1 Trigger Efficiencies

The largest amount of luminosity of nominal vertex data is collected by subtrigger $s2$. The subtriggers $s3$ and $s0$, which have less restrictive conditions are more sensitive to background and are thus higher prescaled. Unfortunately, $s2$ has reduced efficiency, since a considerable fraction of good DIS events does not fulfill the vertex trigger requirements imposed on $s2$.

The efficiency of $s0$ is calculated from the data using a sample of events triggered independently of the Spacal. Events fulfilling the standard event selection criteria are accepted for the trigger sample if at least one Spacal-independent actual subtrigger has triggered the event. The efficiency is then given by the ratio between the number of events in the trigger sample where the 'raw' subtrigger $s0$ is on and the total number of events in the trigger sample. The definitions of raw and actual subtriggers is given in section 2.2.

Fig. 4.1(a) shows the trigger efficiencies for $s2$, $s0$ and $s3$ as a function of the logarithm

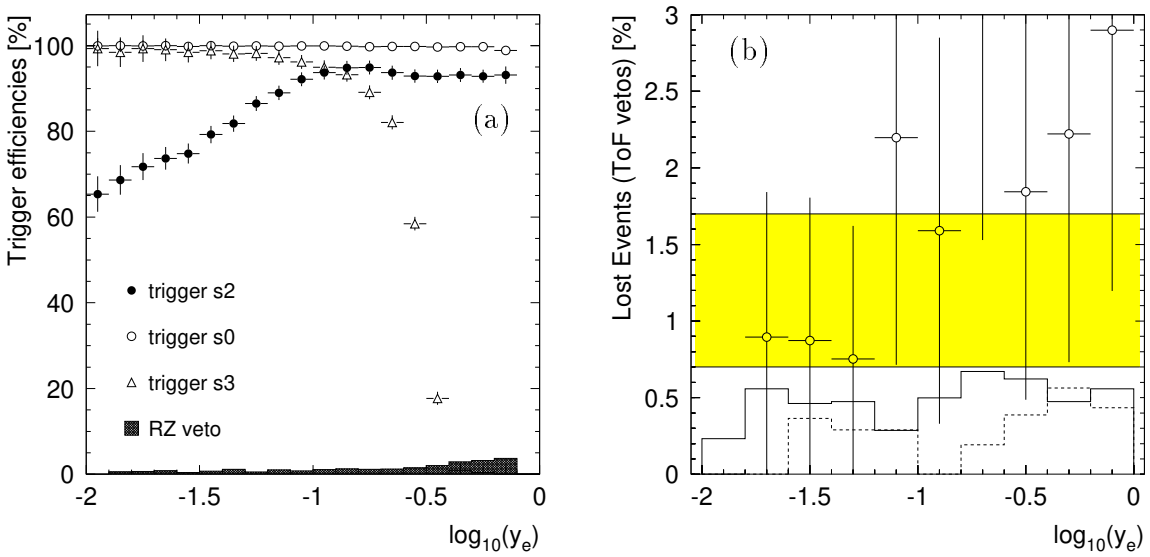

Figure 4.1: (a) The subtrigger efficiencies shown as a function of $\log_{10}(y)$ for the subtriggers $s0$ (open points), $s2$ (full points) and $s3$ (triangles). The black histogram indicates the fraction of events lost due to the RZ_{veto} requirement. (b) The fraction of lost events due to the ToF background veto is represented by the grey error band. Separately shown are the contributions from BToF-or-PToF (open points), FToF (solid line) and Veto Wall (dashed line).

of the inelasticity y. $s0$ is fully efficient ($> 99.5\%$) everywhere, except at the highest values of y. Here, small inefficiencies originate from the region very close to the beam pipe due to gain adjustment problems of particular Spacal cells. The inefficiency is explicitly corrected individually for each analysis bin. The behavior of subtrigger $s3$ is determined using an event sample triggered with $s0$. The figure shows the onset of the events triggered with $s3$ at $\log_{10}(y) \lesssim -0.5$ corresponding to $y \gtrsim 0.3$ or an electron energy of more than ~ 20 GeV. The efficiency of the vertex requirements of subtrigger $s2$ is determined using a sample of events triggered with $s0$. At high y, $s2$ reveals an efficiency of 90% to 95% which decreases towards lower y down to a level of 65% at $y = 0.01$. This behavior is expected since in events with low inelasticity y the hadronic final state is oriented to the extreme forward direction and may therefore miss the acceptance region of the tracking detectors. The black histogram depicts the y dependent inefficiency originating from the RZ_{veto} condition. It reaches a level of 4% at the highest values of $y \sim 0.7$.

The fraction of events lost due to the background veto from the ToF counters (FToF, BToF, PToF and Veto Wall) is estimated[2]. For this purpose the dedicated subtriggers $s8$, $s11$ and $s12$ are used. They consist of a Spacal IET > 0 requirement in coincidence with a positive out-of-time condition (inverted veto) for the FToF ($s8$), BToF 'ored'

[2]The efficiency of the timing requirement in the Spacal IET Trigger is implicit to the efficiency of $s0$.

with PToF ($s11$), and the Veto Wall ($s12$). The number of good events rejected by the out-of-time veto condition of the ToF counters is measured by counting the number of events accepted by the opposite condition, i.e. a positive out-of-time condition. In fig. 4.1(b) the fraction of good events lost due to one of the ToF requirements is plotted as a function of y. The contribution from the FToF ($s8$) and the veto wall ($s12$) are both of the order of 0.5%. The open points refer to BToF 'ored' with PToF as measured with $s11$. The size of the error bars is due to the large trigger prescales of $s11$. Within the large uncertainty there is some indication that the loss of events due to BToF 'ored' PToF increases with increasing y. However, the total loss of events is estimated assuming uncorrelatedness and constant behavior in y. The result of $1.2\% \pm 0.5\%$ is represented in the figure by the grey error band. The number of events measured in the data is corrected accordingly. Another way to estimate the loss of good events due to the veto requirements is to calculate the random coincidence between good ep events and beam related background.

4.4.2 Trigger Selection and Efficiency Correction

The trigger selection is based on subtrigger $s2$. $s0$ and $s3$ are used to compensate the inefficiency of $s2$ using the following prescription: All events 'actually' triggered by $s2$ are accepted and assigned a weight of 1. Events are recovered, i.e. accepted nevertheless, if the 'raw' subtrigger $s2$ is not on and if either: 'actual' $s3$ is on, or: 'raw' $s3$ is off and 'actual' $s0$ is on. The weight of the recovered events is given by the ratio of the luminosity collected with $s2$ and the luminosity collected with $s0$ and with $s3$ respectively. The values of the weights can be read off column 6 (10) in table 4.2. The advantage of the scheme is the following. The sample contains the whole phase space of event topologies whereas a pure $s2$ sample would be biased according to the behavior of the vertex triggers. Full use is made of the available statistics. Thus, effectively, the minimum bias trigger $s0$ is used. Replacing $s2$ by $s0$, $s3$ by $s7$ and $s0$ by $s5$ one obtains the prescription for the shifted vertex data.

Loss of events due to the software filters L4 and L5 has been checked and found negligible in general[3].

4.5 Vertex Reconstruction

The position of the interaction vertex is measured using the central and forward drift chambers. Events are rejected if no reconstructed vertex exists or if the reconstructed z-position of the vertex is further than 30 cm away from the nominal interaction point (cuts # 10 and 11 in table 4.1). The cuts are motivated by three main reasons. Firstly, the precise knowledge of the position of the interaction point is needed for the accurate

[3]For the shifted vertex data a small fraction (2%) of lost events has been actually detected where, due to a mistake in the software at level L4, events exclusively triggered with $s0$ were rejected. The effect is compensated using subtrigger s6 for the specific runrange.

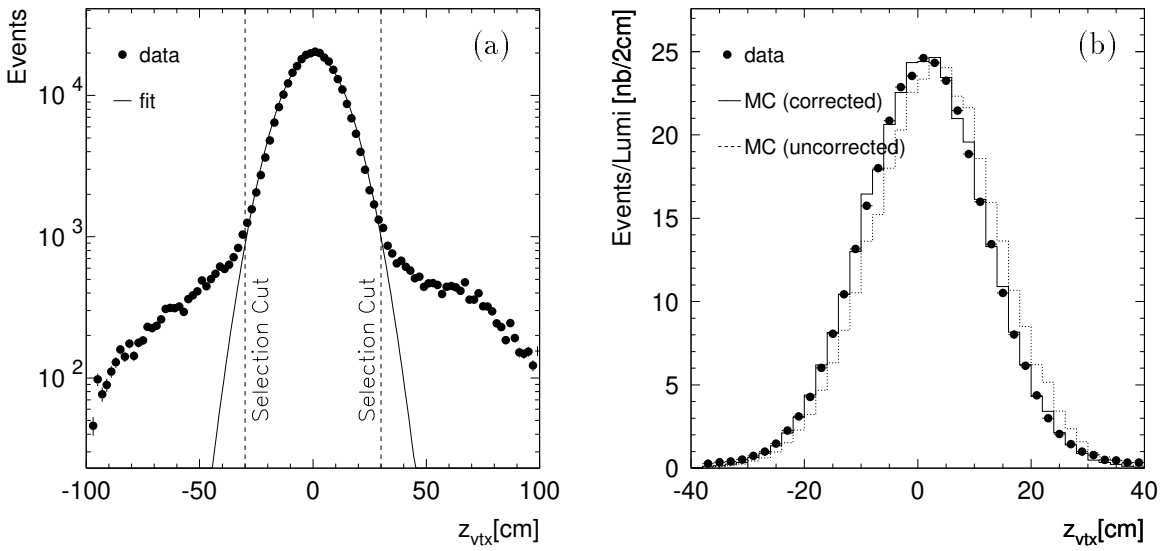

Figure 4.2: (a) Distribution of the z-position of the vertex in the data. Events outside ± 30 cm are rejected. (b) The vertex distribution in the data (points) and in the corrected Monte Carlo simulation (solid line). The dashed line shows the distribution of the uncorrected distribution in the Monte Carlo simulation.

reconstruction of the event kinematics. In particular the z-position varies considerably from event to event and, thus, directly affects the measurement of the polar scattering angle θ and the reconstruction of Q^2. Secondly, the cut on the z-position is necessary to restrict the data sample to the main interaction region for which reliable Monte Carlo simulations are available. Finally, the cut is important to suppress beam induced non-ep background. The determination of the efficiency of the vertex requirement is one of the crucial points of the analysis presented here and will be discussed in section 4.5.2.

4.5.1 Position of the Reconstructed Vertex

In fig. 4.2(a) the distribution of the z-position of the reconstructed event vertices is shown as measured in the data. The solid line depicts a fitted Gaussian curve. All selection cuts are imposed except the cut on the z-position of the vertex (cut # 11 in table 4.1). The latter cut is indicated in the figures by the dotted line at ± 30 cm. Outside this region non-Gaussian tails are visible. They are partially due to proton satellite bunches. Early and late proton satellites are shifted in time by ± 4.8 ns with respect to the main proton bunch and collide with the main electron bunch around ± 70cm, respectively. Other contributions come from events with a badly reconstructed vertex or from beam wall or beam gas interactions.

Efforts by the HERA machine group to reduce in particular the late satellite bunches lead to the asymmetry of the distribution. In addition L1 trigger criteria (e.g. the PToF veto) and cuts in the H1 event classification are responsible for the rejection of late

satellite bunches while early satellite bunches are kept for potential physics analysis. The rejection of satellite bunches connected with z-vertex values of more than 30 cm involves a correction of the integrated luminosity by $-3.6\% \pm 1.5\%$ ($-4.6\% \pm 3\%$) for the nominal (shifted) vertex data, respectively [35]. This correction introduces the main uncertainty on the overall normalization of the measurement. The values listed in table 4.2 refer to the corrected integrated luminosity.

In fig. 4.2(b) the reconstructed z-position of the interaction point of the selected events is shown in the data and in the Monte Carlo simulation. The simulated distribution is corrected to the data using a z-position dependent weighting of the simulated events assuming a Gaussian shape. Also shown is the uncorrected distribution. This distribution was initially assumed for the simulation of the Monte Carlo events.

4.5.2 Vertex Reconstruction Efficiency

For the measurement of the cross section the loss of good ep events due to the vertex existence requirement has to be quantified. For this purpose the Monte Carlo simulation is compared to the data with respect to the vertex reconstruction efficiency. The vertex reconstruction efficiency is defined as the ratio between the number of selected events with a reconstructed vertex within 30 cm and the total number of events from ep collisions within 30 cm. The determination is not straight forward. On the one hand it is necessary to remove the vertex existence requirement, on the other hand the z-position of the vertex should be known for all events. As soon as the cut is removed events without a vertex from outside 30 cm enter the event sample and thus spoil the measurement. Beyond that, the fraction of non-ep background events becomes sizable.

In former analyses the Central Inner Proportional Chamber CIP was used to identify electron tracks of good events [80]. In connection with the BDC (formerly with the BPC) the z-position of the vertex could be reconstructed. However, this method works only in the acceptance region of the CIP at scattering angles $\theta \lesssim 170°$ (corresponding to $Q^2 \gtrsim 10$ GeV^2). At lower values of Q^2 a vertex reconstruction independent of the Central and Forward Drift Chambers is not possible[4]. The uncertainty of the slope of the electron track measured in the BDC alone is too large to determine the z-position of the interaction point (see section 4.7).

For the low Q^2 analysis presented here, a different strategy is developed. A backward-forward Time-of-Flight criterion is imposed to select events within $\pm$ 30 cm around the nominal vertex position[5]. It makes use of the time information of the PToF (forward) and the Spacal (backward). While the Spacal measures the arrival time of the electron the PToF measures the timing of the proton undergoing the interaction, thus the z-position of the interaction can be estimated. Events are selected if the PToF time lies

[4]Since 1997 the Backward Silicon Tracker (BST) is operational. It measures the electron track up to an angle of $\sim 176°$ at the nominal vertex position and thus provides a means to determine the vertex position for low Q^2 events independently of the Central Jet Chamber.

[5]A detailed account of the use of Time-of-Flight conditions for background rejection is given in [36].

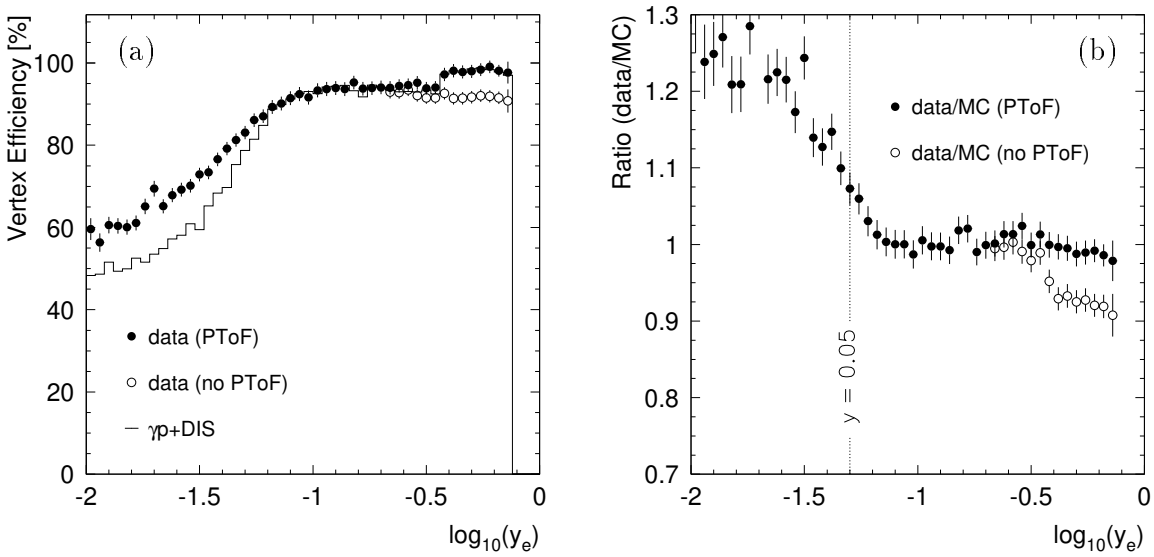

Figure 4.3: (a) The vertex reconstruction efficiency is shown for the data (points) and for the DIS+γp Monte Carlo simulation (solid line) as a function of $\log_{10}(y_e)$. A sharp Time-of-Flight cut on Spacal and PToF time is applied. The vertex reconstruction efficiency without PToF cut is shown as open points. (b) Ratio between the data and the Monte Carlo simulation with (full points) and without (open points) PToF timing criterion.

in the range between 37 and 45 ns. In the backward region the time of the hottest cell of the Spacal is required within 11 and 13 ns for the nominal vertex data. In the shifted vertex data an offset of +4 ns is applied to the Spacal timing according to the increase of the time of flight. Unfortunately, the acceptance of the PToF is very limited (to polar angles of $0.7^\circ < \theta < 3.2^\circ$ for the nominal vertex data). Possible consequences to the result will be discussed at the end of this section.

Fig. 4.3(a) compares the vertex efficiency as a function of $\log_{10}(y_e)$ as determined for the data and for the DIS+γp Monte Carlo simulation. For $\log_{10}(y_e) > -1.2$, i.e. $y_e \gtrsim 0.06$, it is at the level of 90 to 95%. In fig. 4.3(b) the ratio of the efficiencies between the data and the Monte Carlo simulation is plotted. The agreement in this region is better than 2%. Towards lower y the vertex reconstruction efficiency severely degrades. This behavior is expected since the hadronic final state of low inelasticity events is mostly located in the extreme forward direction where the tracking detectors have limited acceptance. The same behavior is observed for the efficiency of subtrigger $s2$ (see above). However, the discrepancy between the Monte Carlo simulation and the data in this region is not understood. Possible reasons are an inappropriate description of the hadronic final state properties and/or uncontrolled migrations of events in y. The region of extremely low y ($y < 0.05$) where the discrepancy is larger than $\sim 5\%$ is therefore excluded from the measurement of F_2 (see section 5.1).

Inefficiencies at larger values of y_e are mainly caused by migrations of low y events without a reconstructed vertex due to radiation of high energy bremsstrahlung photons

from the incident electron. For these events with initial state radiation (ISR, see also section 4.9) the reconstructed value of y_e is generally overestimated significantly. The step in fig. 4.3(a) at $\log_{10}(y_e) = -0.45$, i.e. $y_e = 0.35$ can be explained by the properties of the event selection cut $E - p_z > 35$ GeV (cut # 9 in table 4.1). In events with $y_e < 0.35$ the electron energy alone is large enough to fulfill the selection criterion $E - p_z > 35$ GeV and all events are accepted[6]. Only in events with $y_e > 0.35$ the hadronic final state becomes relevant for the selection cut. In this region, ISR events are typically rejected since the measured value of $E - p_z$ is small. Thus, the vertex reconstruction efficiency in this region is increased.

The influence of the PToF time requirement is investigated in the following. The vertex reconstruction efficiency is calculated without forward timing criterion. At the same time the cut on the z-position is removed. Background is reduced as far as possible, demanding that there be less than 5 tracks in the BDC around the selected electron. The result is depicted by the open points in fig. 4.3(a) and (b), respectively. The reconstruction efficiency is considerably reduced (by up to $\sim 10\%$) especially at large values of y, indicating that a large number of background events enter the sample as soon as the vertex cut is removed.

Due to the fact that the angular acceptance of the PToF is limited the use of the PToF requirement tightly constrains the event topologies accepted for the vertex efficiency determination. In particular diffractive events with a 'rapidity gap' where no activity in the forward direction is measured, are completely rejected because, by definition, they do not have any signal in the PToF [84]. A dedicated study of the vertex reconstruction efficiency of diffractive events has been performed using Monte Carlo simulations [85]. This showed that in particular non-dissociative diffractive events (where the proton stays intact) producing low mass vector mesons (ρ, ϕ, ω) are rejected due to the vertex requirement. The influence on this measurement is smaller than 2% in the region of $Q^2 \geq 0.85$ GeV^2 and can thus be neglected for the nominal vertex data analysis. At the lowest values of $Q^2 = 0.35$ GeV^2 the influence amounts to 6%. In the shifted vertex data analysis the measured values of F_2 are corrected by up to +6% assigning a systematic error of 50% on the correction.

4.6 Event Selection Using the Spacal

The event selection is based on the successful identification of the scattered electron in the Spacal. The proper electron identification is essential for the correct reconstruction of the event kinematics. A preselection using coarse electron selection cuts, as defined by the H1 event classification scheme, is performed during the reconstruction of the data. The final electron selection cuts as outlined in section 4.2 will now be described.

At least one electromagnetic cluster with an energy of more than 8 GeV (7 GeV for the shifted vertex data) in the Spacal is required (cut # 1 in table 4.1). The cluster in

[6] At low Q^2 the relation $y \sim 1 - E'_e/E_e$ holds in good approximation.

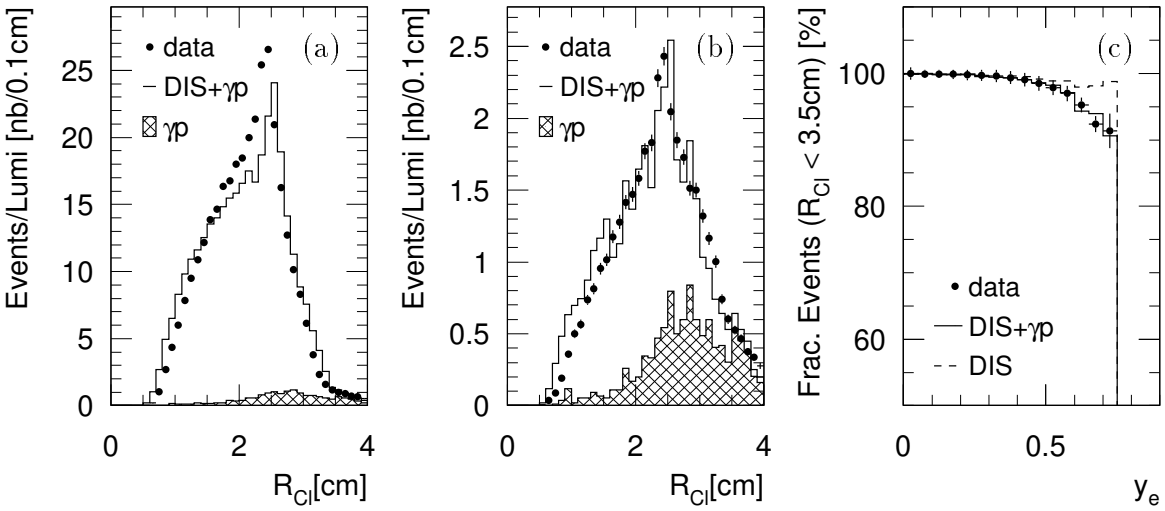

Figure 4.4: The cluster radius R_{cl} is shown in the data (points) and in the DIS+γp Monte Carlo simulation (solid line). (a) includes all events, (b) shows events with $Q_e^2 < 4$ GeV^2 and $y_e > 0.55$. The hatched histogram represents the simulated γp background. In (c) the fraction of events accepted by the electron selection cut $R_{cl} < 3.5$ cm is plotted. The dashed line shows the fraction of accepted true electron events as simulated in the DIS Monte Carlo.

the Spacal with the highest energy deposit is selected as the electron candidate. The event is kept if the complete set of selection criteria as given in table 4.1 is fulfilled at the same time.

The timing of the hottest cell of the electron cluster should be within a window of 8.5 (12.5) and 16.5 (22.5) ns for the nominal (shifted) vertex data, respectively (cut # 2 in table 4.1). This cut is designed to reject out-of-time proton background which, due to different flight path lengths, arrives earlier in the Spacal (see fig. 2.8). Applying all other selection cuts the timing requirement rejects less than 0.1% of the events.

The cluster radius R_{cl} as defined in section 2.3.4 is required to be smaller than 3.5 cm (cut # 3 in table 4.1). The cluster radius provides an estimate of the lateral width of the shower and can thus be used to distinguish between electromagnetic and the broader hadronic showers. In fig. 4.4(a) the distribution of R_{cl} is shown. All event selection criteria are applied except the cut on the cluster radius itself. The distribution of the simulated DIS Monte Carlo events was shifted by a factor of 1.1 in order to achieve agreement at the right edge of the distribution where the selection cut is applied. As is indicated in section 3.2 (fig. 3.2) the description of the shower development in the Monte Carlo simulation is not appropriate. Recent test simulations have shown that reasonable agreement between the simulation and the data can be achieved by tuning the sampling frequency of the shower development in the simulation [86]. In

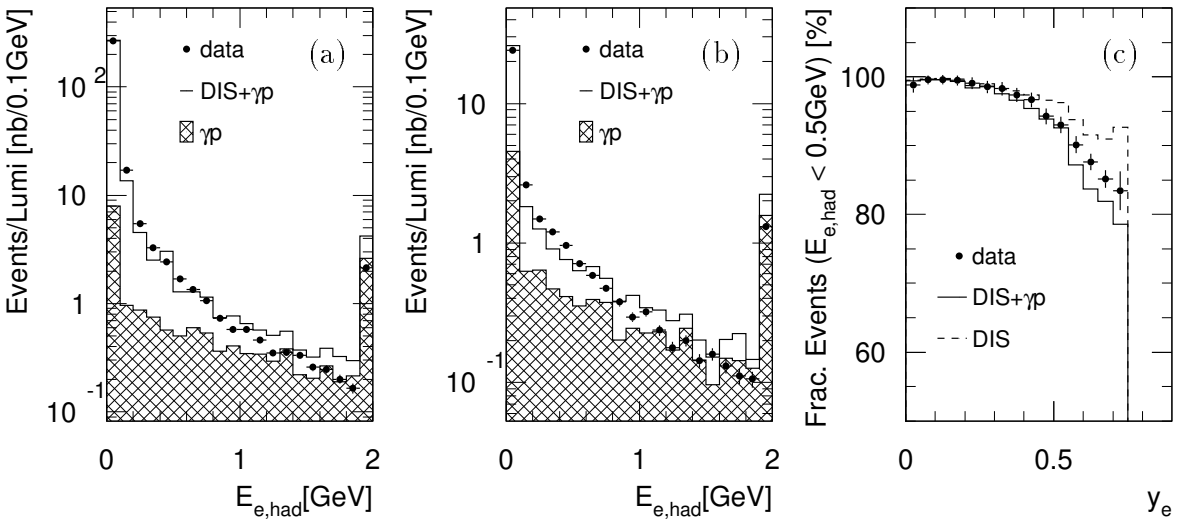

Figure 4.5: Distribution of the energy in the hadronic section of the Spacal behind the electron candidate $E_{e,had}$ is shown for the data (points) and the DIS+γp Monte Carlo (solid line). (a) includes all events and (b) shows events with $Q_e^2 < 4$ GeV^2 and $y_e > 0.55$. The hatched histogram represents the simulated γp background. In (c) the fraction of events accepted by the electron selection cut $E_{e,had} < 0.5$ GeV is plotted. The dashed line shows the fraction of accepted events in the DIS Monte Carlo simulation.

order to study the region with small Q^2 and high y, where the contribution from background is particularly large, events are selected with $Q_e^2 < 4$ GeV^2 and $y_e > 0.55$. The distribution of R_{cl} for these events is depicted in fig. 4.4(b). Here the agreement between the data and the corrected Monte Carlo simulation is slightly better than in the overall distribution.

The behavior of the selection cut, $R_{cl} < 3.5$ cm, is investigated in fig. 4.4(c). Here, the fraction of events accepted by the selection cut is depicted as a function of y_e for the data and for the DIS+γp-Monte Carlo simulation. The dashed line shows the fraction of accepted true electron events as simulated in the DIS Monte Carlo. It is larger than 98% everywhere, proving that the amount of lost DIS events is very small and that the bulk of rejected events is due to photoproduction background.

The systematic uncertainty of the cut on the measurement of F_2 is estimated to be 30% of the fraction of electrons lost due to this cut according to the Monte Carlo simulation. It is calculated separately for each analysis bin. The same prescription is used for the uncertainty determination of all electron identification cuts. A full summary of the systematic errors is given in section 5.2.

The energy 'behind' the electron candidate in the Hadronic Spacal $E_{e,had}$ inside a cylinder of 17.5 cm should be smaller than 0.5 GeV (cut # 4 in table 4.1). This cut is motivated by the fact that electromagnetic showers in general are completely

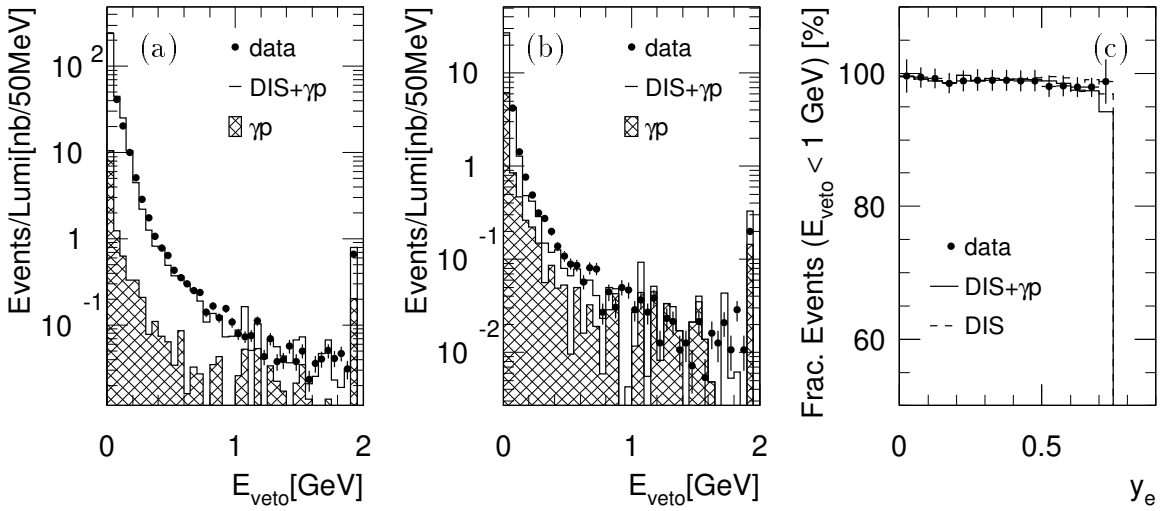

Figure 4.6: The energy in the veto layers close to the electron candidate for DIS+γp Monte Carlo simulation (solid line) and data (points), (a) in all events and (b) in events with $Q_e^2 < 4$ GeV^2 and $y_e > 0.55$. The fraction of events with $Q_e^2 < 2.5$ GeV^2 and an energy deposit of less than 1 GeV is shown in (c). The dashed line refers to the DIS Monte Carlo simulation showing the fraction of electrons accepted.

contained in the Electromagnetic Spacal. In fig. 4.5(a) the distribution of $E_{e,had}$ is shown for all events, in (b) events with $Q_e^2 < 4$ GeV^2 and $y_e > 0.55$ are selected. All selection criteria are imposed except the cut on $E_{e,had}$ itself. Events with more than 2 GeV are accumulated in the histogram at 2 GeV. In both distributions reasonable agreement between the data and the Monte Carlo simulation can be observed. However, the tails of the distributions indicate weaknesses in the understanding of the shower development in the Spacal in particular for the photoproduction background (see section 4.8). In fig. 4.5(c) the fraction of events accepted by the cut $E_{e,had} < 0.5$ GeV is shown. The behavior indicates that in particular at large values of y the fraction of DIS events rejected is large. Such behavior is conceivable for DIS events where a part of the hadronic final state is selected as the electron candidate or in the case of overlap of the scattered electron and the hadronic final state.

The energy in the veto layers of the Spacal near the beam pipe, E_{veto}, measured within a distance of 15 cm from the electron cluster should not exceed 1 GeV (cut # 5 in table 4.1). The distributions are depicted in fig. 4.6(a) and (b) for all events and for events with $Q_e^2 < 4$ GeV^2 and $y_e > 0.55$, respectively. Both distributions are well described in the Monte Carlo simulation, also in the far tail of the distribution and in the overflow bin. The figures show that the number of events which leak electron energy into the beam pipe is very small. This is due to the fiducial radial cut $R_\theta > 8.7$ cm, described in the following section. In fig. 4.6(c) the fraction of events accepted by the

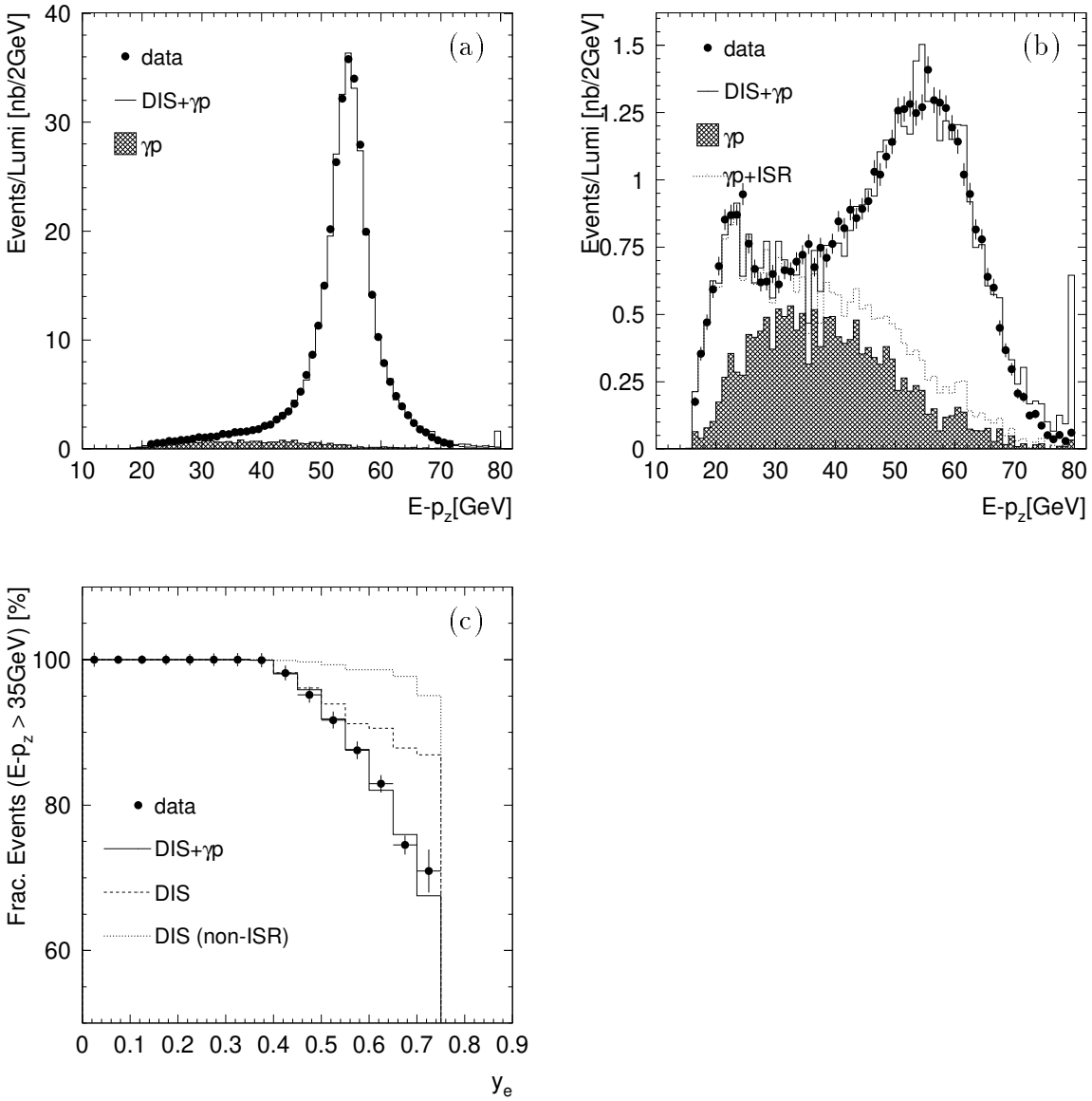

Figure 4.7: The distributions of $E-p_z$ in the data (points) and in the Monte Carlo simulation (solid line). In (a) all events and in (b) events with $Q_e^2 < 4$ GeV^2 and $y_e > 0.55$ are shown. The hatched histogram represents the simulated photoproduction background. In (b) ISR events are represented as a dashed line. In (c) the fraction of events accepted by the cut $E - p_z > 35$ GeV is plotted for the data (points) and for the DIS+γp (solid line), DIS (dashed line) and DIS Monte Carlo simulations excluding ISR events (dotted line).

selection cut is shown as a function of y_e. Here, only events with $Q_e^2 < 2.5$ GeV^2 where the cut is relevant are used.

The value of $\mathbf{E - p_z}$ should be larger than 35 GeV (cut # 9 in table 4.1). $E - p_z$ denotes the difference between the energy and the z-component of the momentum summed over all particles. Its value gives an estimation of the containment of backward going particles in the detector (section 2.4). $E - p_z$ is measured by summing over the energies of all calorimeter cells of the central detector, excluding the electron tagger and photon detector (section 2.2),

$$E - p_z = \sum_{\text{cells}} E \cdot (1 - \cos\theta_i). \tag{4.7}$$

For the use as a selection cut no track information is taken into account. Fig. 4.7(a) shows that the distribution of events is peaked at the expected value of 55 GeV ($= 2 \cdot E_e$). All selection cuts are applied except $E - p_z$ itself. The excellent agreement between the data and the Monte Carlo simulation proves a good energy calibration. The tail towards lower values originates from photoproduction events, and events with initial state radiation. This is more obvious in fig. 4.7(b) where $E - p_z$ is plotted for events with $Q_e^2 < 4$ GeV^2 and $y_e > 0.55$. Fig. 4.7(c) depicts the behavior of the $E - p_z > 35$ GeV cut as a function of y_e. The figure shows, first of all, that the selection cut is highly efficient against γp background. Furthermore, the cut rejects DIS events with QED initial state radiation and thus helps to reduce the magnitude of the acceptance corrections due to radiative effects (see also fig. 5.3). At the same time the number of non-radiative events rejected is small.

4.7 Measurement of the Electron Scattering Angle using the BDC

The Backward Drift Chamber BDC is described briefly in section 2.2. A detailed detector description can be found in [33]. The BDC provides precise information about the position of the impact point of the scattered electron. The scattering angle θ is measured as the opening angle between the measured beam axis and the line connecting the radial position R of the selected electron track in the BDC with the interaction vertex[7]. The beam axis is determined individually for each run using the distribution of reconstructed vertices measured in the CJC.

In this section a brief account of the angular measurement is given. It closely follows [27], where the complete description of the use of the BDC for the measurement of F_2 with the 1995 data can be found. In section 4.7.1 the selection of the electron track is described. Values for the angular resolution are given in section 4.7.2. The

[7] Note that in the following the radial distances are calculated in the z-plane of the center of gravity of the corresponding shower in the Spacal.

selected track is used for the event selection imposing BDC–Spacal matching criteria and for a fiducial cut on the detector volume (section 4.7.3). The final radial distribution reveals a peculiar behavior of the data in a region of 25 cm from the beam axis. In section 4.7.4 possible reasons are discussed and a phenomenological prescription for the treatment of the Monte Carlo simulation in this region is given.

4.7.1 Electron Track Selection

The hits measured in the eight layers of the BDC are combined to track candidates by using a so called Kalman filter [33, 87]. A track hypothesis is accepted if hits in at least three out of eight BDC layers fulfill a set of reconstruction criteria (see below).

In a large fraction of events (60%-70%) the scattered electron interacts with the dead detector material situated between the interaction point and the BDC causing preshowering processes. In these events the number of reconstructed tracks in the BDC is substantially increased. To find the electron track in the BDC is therefore somewhat difficult. The reconstruction algorithm used in this analysis typically reconstructs up to about 30 tracks within a cylinder of 3 cm around the impact point of the electron. Only in about 40% of the events the number of reconstructed tracks in the BDC is less than five. The latter events are called non-preshowering in the following. The second reason for the large number of reconstructed tracks is the BDC geometry itself. The eight layers are situated within an overall distance of only 6.8 cm in z and provide little redundancy to resolve ambiguities of the hit positions[8]. The usual χ^2 criterion using the distance of closest approach between tracks and hits is therefore not sufficient for an unambiguous track selection.

The solution used in this analysis is a generalized χ^2 selection criterion [27]. The idea is to quantify the reliability of a given track but to avoid a sharp cut on pure BDC information. The definition of χ^2_{sel} is

$$\chi^2_{sel} = \chi^2_{BDC} + \left(\frac{\Delta\theta}{\sigma_\theta}\right)^2 + \left(\frac{\Delta(d\phi/dz)}{\sigma_{(d\phi/dz)}}\right)^2 . \tag{4.8}$$

A track with a small χ^2_{BDC} is selected if the track also points to the interaction zone. The difference $\Delta\theta$ between the polar angle of the track measured in the BDC alone and the polar angle of the straight line from the vertex to the measured BDC track coordinate as well as the azimuthal slope $d\phi/dz$ of the track should not exceed the calculated resolutions σ_θ and $\sigma_{(d\phi/dz)}$. The five tracks with minimal χ^2_{sel} are preselected. All other tracks are rejected. Among these five tracks the track with the least distance of closest approach to the Spacal center of gravity is selected as the electron track.

The BDC track finding efficiency, i.e. the probability of finding an electron track within 3 cm around the electromagnetic cluster in the Spacal is investigated [27]. It amounts

[8] Ambiguities (mirror hits) are a characteristic of drift chambers due to the evaluation of the drift times.

to 98% in the central region within a radius of 25 cm where the distance of the wires is small (1 cm), and 96% in the outer part at radii above 27 cm where the BDC cells are larger (3 cm). The difference is mainly due to HV problems in the outer part which, in the 1995 data taking period, led to dead sectors. In the intermediate region between small and large cells, the data reveal larger inefficiencies of up to 5%. The Monte Carlo simulation has been tuned to reproduce the behavior of the data everywhere to better than 1%. For the intermediate region a ϕ-dependent efficiency correction [27] is applied.

4.7.2 Resolution and Systematic Shift of the Electron Angle

The radial resolution of the BDC was determined using tracks measured in the CJC pointing to the electron cluster in the Spacal. Since the acceptance of the CJC restricts this method to the region of $\theta < 170°$ the results were transferred to the central region of the BDC with the help of Monte Carlo simulations. For non-preshowering events a radial resolution σ_R of 0.8 mm is achieved, for preshowering events the resolution is 1.8 mm [27]. The simulated Monte Carlo resolution was adjusted accordingly.

In general the polar angular resolution σ_θ, is composed of three different sources, namely the uncertainty of the measurement of the z-coordinate of the vertex position, the error on the position of the BDC in z and the radial resolution of the BDC itself. However, in first approximation, the uncertainties in z are small compared to the distance between the vertex and the BDC (140 cm for the nominal vertex data) and can be neglected. The angular resolution can then be estimated as

$$\sigma_\theta \approx \frac{\sigma_R}{z_{\mathrm{BDC}} - z_{\mathrm{vtx}}} \tag{4.9}$$

yielding a minimum value of 0.6 mrad for non-preshowering events with nominal interaction points. Possible systematic shifts of the measured polar angle have been investigated. The uncertainty is estimated to be less than 0.5 mrad [27]. This value is assigned as an experimental uncertainty to the measurement of F_2 with both shifted and nominal vertex data.

4.7.3 BDC Event Selection Criteria

Events are selected if the electron track is found within less than 2 cm in radial distance ΔR and 2.5 cm in azimuthal distance $R \cdot \Delta\phi$ to the center of gravity of the Spacal cluster (cuts # 6 and 7 in table 4.1). The asymmetry of the cut in ΔR and $R \cdot \Delta\phi$ accounts for the difference between the azimuthal and radial resolution (see below). However, it should be emphasized that the limiting factor of these cuts is the spatial resolution of the Spacal.

Fig. 4.8 shows the distributions of ΔR (a) and $R \cdot \Delta\phi$ (b) between the BDC track extrapolated to the Spacal plane and the Spacal center of gravity. The agreement

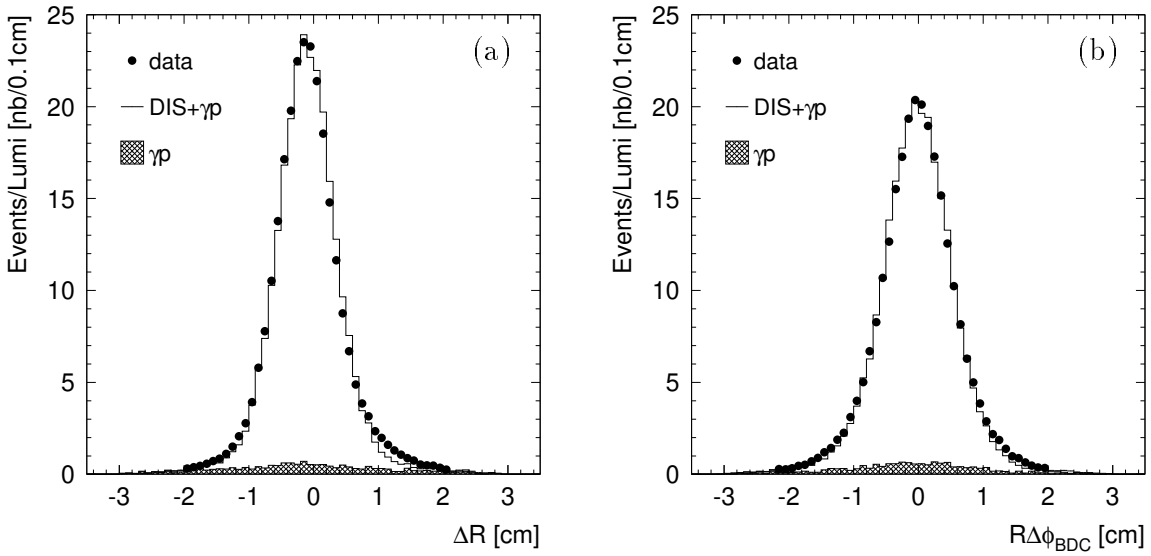

Figure 4.8: (a) Radial and (b) azimuthal distance between the Spacal center of gravity and the BDC track extrapolated to the Spacal plane for the DIS+γp Monte Carlo simulation (solid line) and the data (points). The hatched histogram shows the contribution from γp background events.

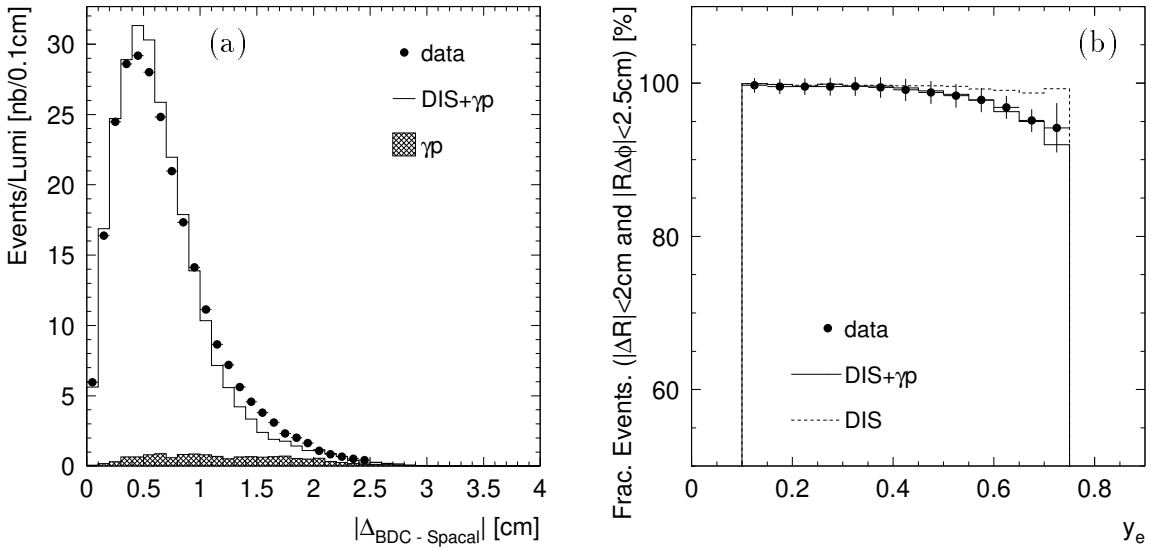

Figure 4.9: (a) The distance between the selected electron track extrapolated to the Spacal plane and the Spacal center of gravity is shown for the data (points) and the Monte Carlo simulation (solid line). The hatched histogram shows the contribution from photoproduction background. In (b) the fraction of events accepted is shown as a function of y for the data (points) and for the DIS+γp (solid line) and DIS (dashed line) Monte Carlo simulation, indicating that the loss of events is due to the rejection of photoproduction events.

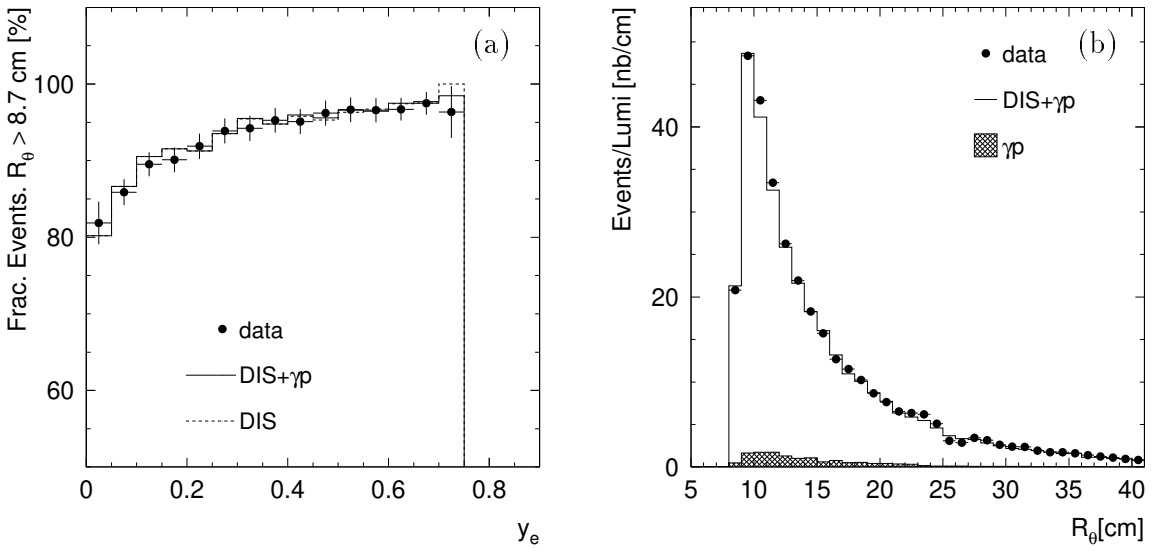

Figure 4.10: (a) Fraction of events accepted by the fiducial cut $R_\theta > 8.7$ cm for the data (points) and the DIS+γp Monte Carlo simulation (solid line). The dashed line shows the same distribution for the DIS Monte Carlo simulation only. (b) Radial distribution of selected events for the data (points) and the Monte Carlo simulation (solid line). The hatched histogram shows the contribution from photoproduction background.

between the data and the Monte Carlo simulation indicates that the angular measurement is well controlled. Furthermore, no overall shifts are observed. The distribution of the distance $\sqrt{\Delta R^2 + (R\Delta\phi^2)}$ is shown in Fig. 4.9(a). Here the cuts $\Delta R < 2$ cm and $R\Delta\phi < 2.5$ cm are imposed. In addition to the angular measurement the track-cluster matching requirement is useful for the suppression of photoproduction background since uncharged particles (e.g. photons) which do not produce a track in the BDC are not accepted as electron candidates. The background rejection is illustrated in fig. 4.9(b) where the fraction of events accepted by the track-cluster matching cuts is plotted as a function of y_e. Both the data and the DIS+γp Monte Carlo simulation decrease towards high y to the level of 90% while the DIS Monte Carlo simulation shows full efficiency ($> 99\%$) everywhere.

Events are rejected if the distance between the electron track and the beam axis, R_θ, is smaller than 8.7 cm (cut # 8 in table 4.1). The value of this fiducial cut roughly corresponds to a polar angle of to 177.0° (178.0°) in the nominal (shifted) vertex data, respectively. The main goal of this cut is to minimize energy leakage into the beam pipe. In addition the spatial resolutions of both Spacal and BDC significantly deteriorate very close to the beam pipe due to edge effects. Monte Carlo simulation and data are treated consistently with respect to the kinematic acceptance if the fiducial cut is based on the beam coordinates which are measured with the central jet chamber CJC1 (see also section 4.3). It should not be based on detector coordinates. In this analysis the

fiducial circular cut is not exactly centered on the beam axis but shifted relative to the beam axis by -0.25 cm in x and -0.2 cm in y. The shift accounts for the offset of the averaged beam position relative to the detector acceptance and for inhomogeneities in the Insert of the Spacal (fig. 2.7).

The behavior of the cut is investigated using a sample of DIS events with $Q_e^2 < 2.5\ \mathrm{GeV}^2$ above a radius of 8.25 cm. The fraction of events with $R_\theta > 8.7$ cm is depicted in fig. 4.10(a) as a function of y_e. Fig. 4.10(b) shows the distribution of R_θ for the final event sample where all selection cuts as listed in table 4.1 are applied. In the region of 22 cm to 28 cm the data and the Monte Carlo simulation can be seen to deviate from the expected monotonic dependence. In the following section the reason for this behavior is investigated.

4.7.4 Investigation of the Measured Radial Dependence of Rate

The measured rate behavior at radii between 25 and 27 cm shown in fig. 4.10(b) is not a property of the physics processes, but has to be traced back to detector and/or track reconstruction problems. In this context former analyses can be referred to in which such effects were also observed in a similar region using data recorded with the proportional chamber BPC and the BEMC calorimeter in the year 1994. Indications of poorly understood – and hence inappropriately simulated – dead material effects are reported [88]. In this section the problem is reviewed. It is found that various effects given by the spatial variation of the dead material in the H1 Detector as well as the BDC geometry play a role. The discussion motivates a phenomenological prescription for a more appropriate treatment of the Monte Carlo simulation in the problematic radial region.

Fig. 4.11(a) shows the radial distribution as measured in the Spacal not using the BDC. The distributions in the data and in the Monte Carlo simulation show no significant deviation. The fluctuations of the slope can be explained by the limited spatial resolution of the Spacal due to the finite granularity of the Spacal cells. This granularity effect is more pronounced in fig. 4.11(b) where the difference between the number of events reconstructed in the Spacal and in the BDC is depicted as a function of the radius. Below a radius of 20 cm and above 28 cm the data and the Monte Carlo simulation show good agreement. The structure at small radii reflects the migrations due to the cell granularity of the Spacal. They are correctly reproduced in the Monte Carlo simulation. At large radii (in the region above 28 cm) the granularity effect disappears. It is averaged out over more cells of the Spacal. However, clear disagreement is visible in the intermediate region. The fluctuations of the data around the expectation from Monte Carlo simulation, shown in fig. 4.11(b), indicate that migrations of events rather than losses are responsible for the observed deviation in the data. Non-negligible losses of events would appear in this distribution as a depletion of the rate distribution in the Spacal, fig. 4.11(a). From fig. 4.11(a) and (b) one may conclude that in a large

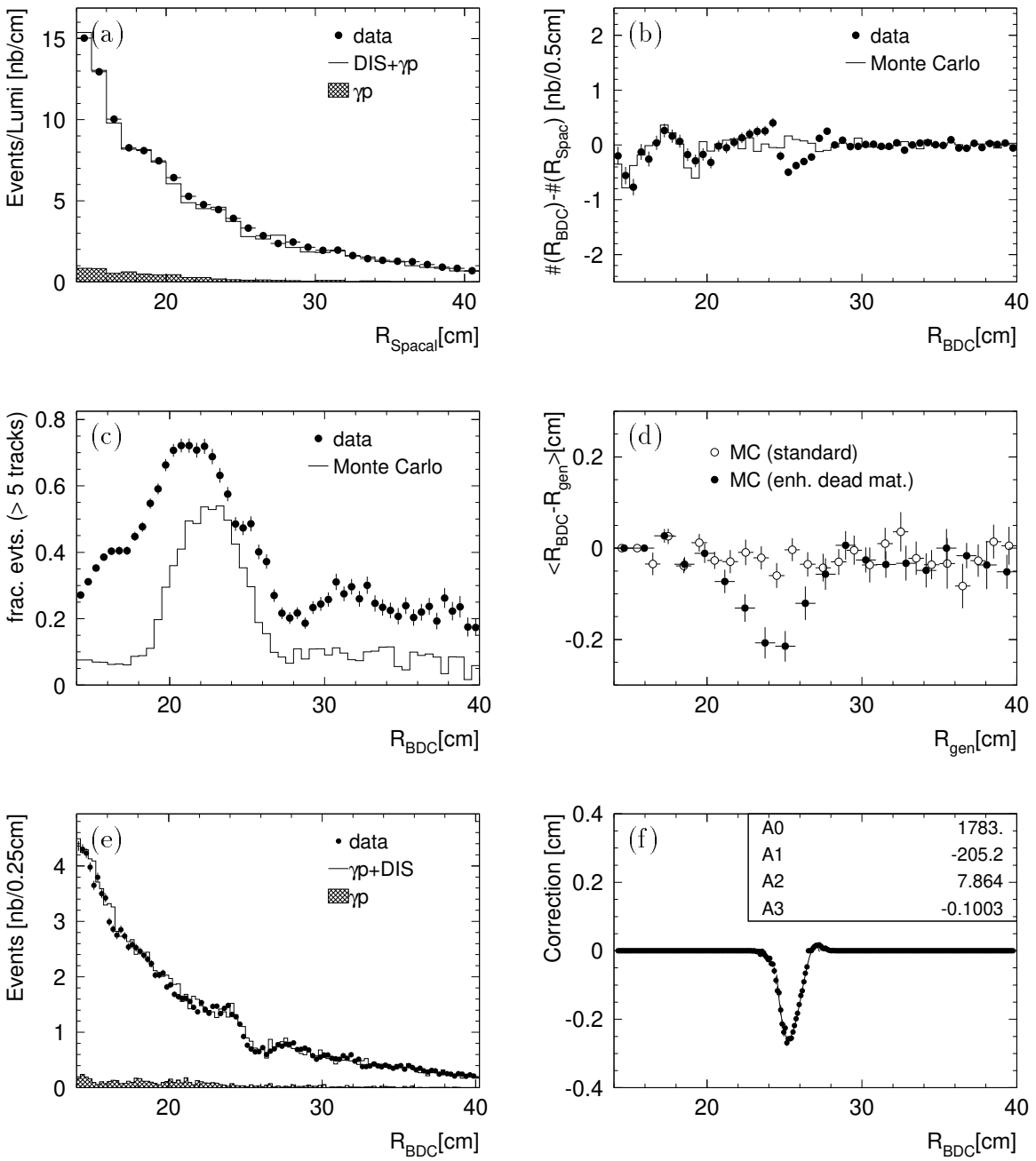

Figure 4.11: (a) Radial rate dependence of the final event sample measured in the Spacal. (b) Difference between the number of events measured in the Spacal and in the BDC at a given radius. (c) Fraction of events with more than 5 reconstructed tracks as a function of the radius measured in the BDC. (d) Average difference between generated and reconstructed radius for the standard Monte Carlo simulation (open points) and a Monte Carlo simulation with increased CIZ end-flange density (full points). (e) Radial rate dependence of the final sample after correction of the simulation as measured in the BDC. (f) Correction function (see text). In (a), (b), (c) and (e) the data (Monte Carlo simulation) are indicated by points (solid lines), respectively. The hatched histogram shows the contribution from photoproduction background.

number of events the selected electron track in the BDC is reconstructed unexpectedly far away from the impact point in the Spacal.

In fig. 4.11(c) the fraction of events with more than five reconstructed tracks is plotted as a function of the BDC radius for the data and for the Monte Carlo simulation. The figure shows that the Monte Carlo simulation does not only globally underestimate the number of reconstructed tracks, but also fails to reproduce the shape of the distribution. While the data show a certain structure, the simulation predicts a flat behavior at the level of 10% outside the region 18 cm $\leq R \leq$ 28 cm, increasing to a level of 50% at the radii between 20 and 25 cm. In this region the end-flange electronics of the tracking devices CIZ and CIP are situated.

A test simulation is performed increasing the simulated density of the CIZ end-flange electronics to yield an increase of the simulated radiation length by a factor of 3. The cut-off energy of photons (electrons) in the simulation is 2 (10) MeV, respectively. Particles with smaller energies are not simulated. Fig. 4.11(d) shows the comparison between the standard Monte Carlo simulation and the simulation with enhanced CIZ end-flange density plotting the difference between the radial impact point on generator level and after detector simulation and reconstruction as a function of the generated radial impact point. Apparently, the increase of the density leads to a shift of the selected electron track towards smaller radii. The average position of the center of gravity in the Spacal was found insensitive to the amount of dead material (not shown).

An explanation for the observed effect can presently only be given in a qualitative way. A quantitative study is still going on.

1. The migrations are due to preshowering processes. The interaction of the scattered electron with the dead material leads to preshowering processes producing a large number of particles with low energy (e^+, e^-, γ). In the Spacal these secondary particles are contained in the electron cluster. Since the position of the cluster is dominated by the high energy primary electron (center of gravity) the Spacal is largely insensitive to preshowering effects. In contrast, the present BDC track reconstruction and selection scheme separates single particle tracks independently of the particle energy. Consequently, the probability to correctly select the track of the primary electron decreases as the number of tracks increases.

2. The event migration is probably due to the geometry of the dead material and of the BDC. One should separate three possible sources:

   Moving from larger to smaller radii the amount of dead material sharply increases around the radius of 25 cm leading to a strongly increased number of tracks (fig. 4.11(c)). As a consequence the spatial resolution drastically degrades with decreasing radius leading to migrations of events predominantly towards larger radii.

   Another influence is given by the presence of the magnetic field which bends low energy ($\mathcal{O}$(10 MeV)) particles produced in preshowering processes towards lower

radii. This effect – together with the deterioration of the resolution described above – leads to a depletion of the rate in the edge region in connection with increased rates towards both smaller and larger radii. The Monte Carlo simulation presented above can not account for the full effect since photons with an energy of less than 2 MeV are not simulated.

As a third source of migrations the geometry of the BDC should be mentioned. At a radius of about 25 cm the wire distance of the BDC changes from 3 cm at larger radii to 1 cm at smaller radii. The transition is mediated by a cell of 2 cm size. The track reconstruction efficiencies as well as the quality of the tracks (in terms of χ^2_{BDC}) may vary considerably between the inner and the outer region. Thus, the probability to select a track through one of the inner cells may be enhanced.

In summary, the radial distribution measured in the BDC shows migrations of the selected electron track towards smaller radii in the region between 25 and 27 cm where the intermediate BDC cell is situated. The present explanation for this effect is preshowering in combination with the BDC track reconstruction and selection algorithm which is sensitive to geometry effects of the dead material. In the Monte Carlo simulation the amount of dead material appears to be underestimated significantly.

Motivated by the above findings a correction function for the application to the Monte Carlo simulation is determined. For impact points measured in the Spacal at a radius between 24.75 and 27.0 cm a shift of the radial position of the electron track by up to 4 mm is performed. The size of the shift is described by a third order polynomial. depicted in fig. 4.11(f). The coefficients can be read off the figure caption. The radial distribution of the corrected Monte Carlo simulation shows reasonable agreement with the data (fig. 4.11(e)).

For the measurement of F_2 the Monte Carlo simulation is corrected following the above prescription. The influence of the correction on the measurement of F_2 amounts to 2% at maximum and is included in the systematic error. It mainly affects the region in Q^2 between 12 and 20 GeV^2. In the shifted vertex data analysis the Q^2 region above 3.5 GeV^2 is affected and is therefore not included in the analysis.

4.8 Photoproduction Background

Photoproduction (γp) processes form the main background source to the DIS event sample due to their huge cross section of ~ 165 μb [70]. The total cross section of DIS events, above $Q^2 \gtrsim 1$ GeV^2 is smaller by roughly a factor of 100. A comprehensive review on photoproduction can be found in [68]. In γp events electron and proton interact with very small momentum transfer $Q^2 < 10^{-2}$ GeV^2, i.e. by exchange of an almost real photon with low virtuality. At small Q^2 the transverse momentum of the

scattered electron is negligible compared to the longitudinal component[9] and the electron passes down the backward beam pipe. However, a fraction of the photoproduction events satisfies the electron selection criteria when the electron signature is faked in the detector by particles from the hadronic final state.

Typical fake electrons can be produced by high energy photons, for instance from π^0 decays ($\pi^0 \to \gamma\gamma$), converting into charged particles ($e^{\pm}$) in the dead material (preshowering). Furthermore the overlap of charged hadrons with photons, for instance $\pi^{\pm}$ and γ, can produce an electron signature in the detector. Also, purely hadronic showers can be classified as electromagnetic due to statistical fluctuations in the shower development.

In this analysis the event generator PHOJET [59], described in section 2.5, is used to simulate the photoproduction background. The aim will be to use the simulated events to subtract statistically the photoproduction background from the data. A good description of the background is important since it directly affects the final result of the cross section measurement. It will be found that it is necessary to apply a set of corrections to the PHOJET simulation of the photoproduction background in order to describe the data.

This section is organized as follows: In section 4.8.1 the data are compared to the Monte Carlo simulation of the photoproduction background using events with electrons detected in the electron tagger. Agreement between the data and the Monte Carlo simulation is achieved after application of a set of corrections to the Monte Carlo simulation (section 4.8.2). A consistency check between the data and the corrected Monte Carlo simulation is performed and an estimate on the uncertainty of the γp background subtraction is given (section 4.8.3).

4.8.1 Tagged Electron Events

About 10% of the photoproduction background events in the DIS sample can be identified unambiguously as background when the true scattered electron is detected in the electron tagger of the luminosity system situated at -33 m in the HERA tunnel (see section 2.2). Since tagged electrons are bent by the magnetic field of the HERA machine the acceptance of the electron tagger strongly depends on the electron momentum and thus on the inelasticity y. In fig. 4.12(a) the y dependence of the tagger acceptance is shown. It is restricted to a narrow range of $0.3 \lesssim y \lesssim 0.6$.

Events are called tagged in the following if a minimum energy of 2 GeV is detected in the electron tagger within the region of good containment of the electron shower. This condition is supported requiring the trigger element 115. All DIS event selection criteria as listed in table 4.1 are imposed except the cut on $E - p_z$ (cut # 9 in table 4.1). In addition to the DIS event selection criteria it is required that the energy in the photon detector be less than 2 GeV and that the value of $(E - p_z)_{\rm tot}$ be less than 68 GeV.

[9] This statement holds for scattered electrons above energies of a few hundred MeV only.

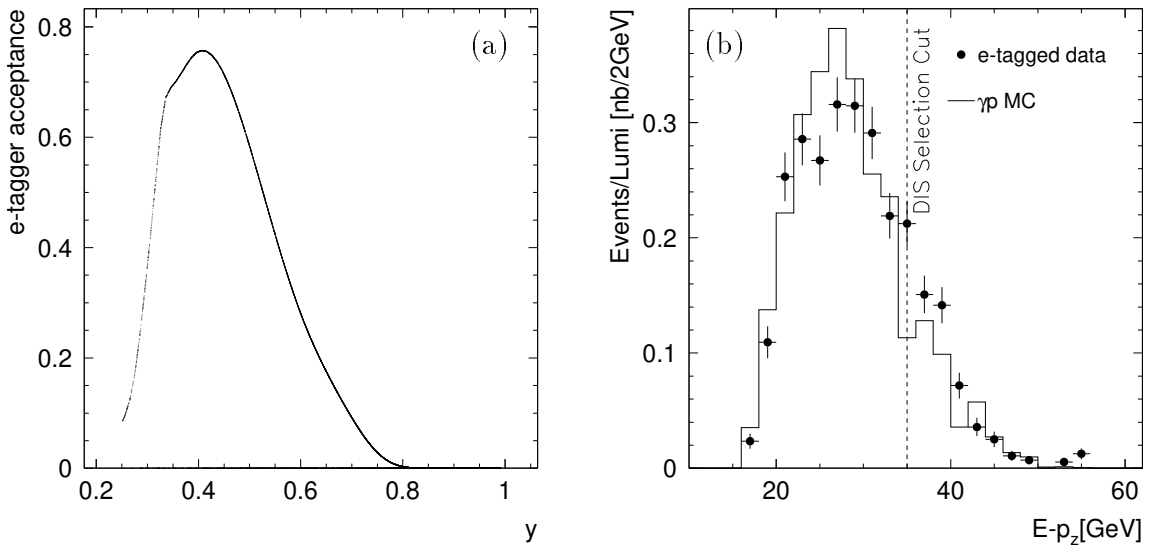

Figure 4.12: (a) Acceptance of the electron tagger as a function of y. (b) Distribution of $E - p_z$ for tagged events summing all energies in the central H1 calorimeters. The energy measured in the electron tagger is not included.

$(E - p_z)_{\rm tot}$ is given by the value of $E - p_z$ measured in the central detector adding the contribution from the energy measured in the electron tagger, i.e.

$$(E - p_z)_{\rm tot} = E - p_z + 2 \cdot E_{\rm e-tagger}. \tag{4.10}$$

These additional cuts serve for the rejection of Bethe-Heitler DIS overlap events which form a background to the tagged photoproduction sample (see below).

In fig. 4.12(b) the distribution of $E - p_z$ for tagged events is shown for data and corrected PHOJET Monte Carlo simulation. For events where the electron is not measured in the central detector but escapes through the backward beam pipe the relation $\sum(E - p_z) = 2 \cdot E_e \cdot y_{\rm JB}$ holds (section 2.4). The distribution thus directly reflects the tagger acceptance[10]. It shows that the bulk of tagged electron events is situated at relatively small values of $E - p_z$ and would be rejected by the cut $E - p_z >$ 35 GeV applied to the DIS event sample. Since the region with finite tagger acceptance and the signal region are kinematically somewhat separated, the background to the F_2 measurement can not directly be determined from the selected sample of tagged photoproduction events in the data, but must be extrapolated from the region of tagged events at small values of y, i.e. small $E - p_z$, into the signal region at $E - p_z > 35$ GeV. The extrapolation is performed with the help of the Monte Carlo simulation.

In fig. 4.13(a) the distribution $(E - p_z)_{\rm tot}$, as defined in equation (4.10), is shown. The distribution has a maximum around 55 GeV as expected for events where the energy

[10] Note that for the exact calculation of the tagger acceptance from the photoproduction data the y dependence of the photoproduction cross section has to be taken into account.

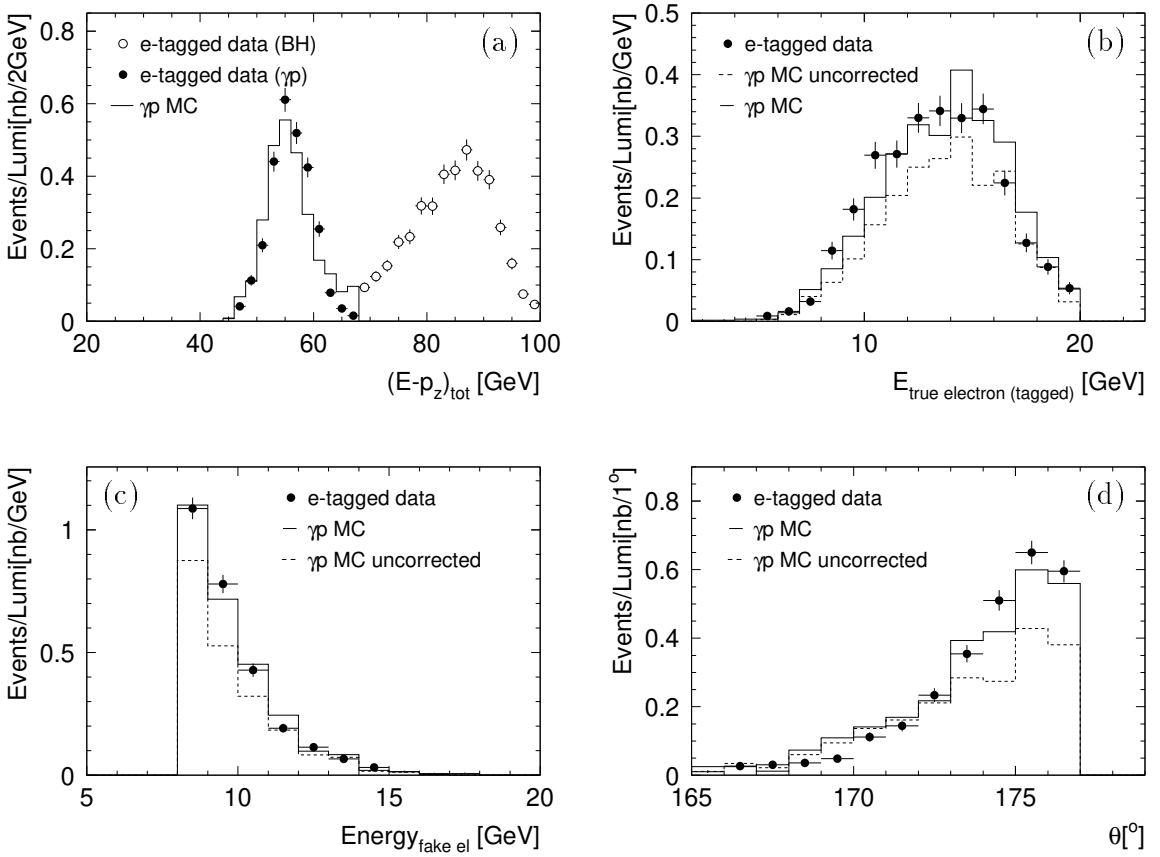

Figure 4.13: Tagged electron data (full points) and corrected PHOJET Monte Carlo simulation (solid line) are compared. (a) distribution of $(E-p_z)_{\rm tot}$ where the sum includes the energy in the electron tagger. For events with $(E-p_z)_{\rm tot} > 68$ GeV (open points) the photon detector requirement is removed. In (b) the energy in the electron tagger, in (c) the energy of the fake electron candidate in the Spacal and in (d) the polar angular distribution of the fake electron candidate are shown. The dashed histogram represents the behavior of the PHOJET Monte Carlo simulation before any correction.

of all particles is contained in the detector. The entries with $(E-p_z)_{\rm tot} > 68$ GeV are due to Bethe-Heitler (BH) events ($ep \to ep\gamma$) which overlap with DIS events and thus fulfill the electron selection criteria as given in table 4.1 (for BH events see section 4.9). Here, for events with $(E-p_z)_{\rm tot} > 68$ GeV no requirement on the energy in the photon detector is imposed. Due to the large cross section of BH processes the overlap rate with DIS events is of the order of $\sim 0.3\%$. The figure shows that the single event values of $(E-p_z)_{\rm tot}$ in overlap events add to a value of $(E-p_z)_{\rm tot}$ of ~ 90 GeV on average. For the study of the photoproduction background using tagged events the BH DIS overlap events are rejected by imposing the above described requirements, that $(E-p_z)_{\rm tot} < 68$ GeV and that the energy in the photon detector is less than 2 GeV.

In fig. 4.13(b) the energy distribution of tagged electrons is compared between the data and the PHOJET Monte Carlo simulation. The simulated energy of the electron

is recalculated using the generated electron energy and smearing it by a Gaussian of $15\%/\sqrt{E}$ according to the energy resolution of the electron tagger. The tagger acceptance (fig. 4.12(a)) is accounted for using a y-dependent event weighting. Fig. 4.13(c) and (d) depict the energy and angular distribution of the (fake) electron candidate in the Spacal, respectively. The corrected Monte Carlo distributions match reasonably with the data. The angular distribution reveals that the discrepancy between the data and the uncorrected Monte Carlo simulation mainly originates from the region of $\theta > 174°$. In this region no measurement of the hadronic final state in photoproduction has been performed so far. The corrections applied in this analysis to the PHOJET simulation are described in the following section.

4.8.2 Corrections to the PHOJET simulation

The simulation of the fake electron candidate and the subsequent shower development in the Spacal is only one aspect of the description of the hadronic final state in photoproduction processes. The background sample of tagged events presented above is not at all suitable for an investigation of photoproduction processes. However, for the purpose of the F_2 measurement the simulation is only required to effectively describe the data distributions relevant for the statistical background subtraction. Therefore a phenomenological treatment of the background simulation which may or may not average over the possibly different sources of any discrepancy is justified.

Various combinations of event selection cuts have been applied to investigate the discrepancy between the simulated PHOJET photoproduction background and the data. The most striking effect is found when the requirement that a reconstructed vertex exists is removed. In fig. 4.14(a) the angular distributions of fake electrons in the data and in the uncorrected PHOJET Monte Carlo simulation are compared. Here all selection criteria for tagged events are imposed except the vertex requirement. The fact that the distributions agree as soon as the vertex requirement is removed indicates discrepancies in the vertex reconstruction efficiency. The overall normalization, i.e. the absolute number of simulated events for a given integrated luminosity, is reasonably described. The comparison with the number of events in fig. 4.13(d) where the vertex requirement is imposed shows that in the data almost all events have a reconstructed vertex while in the simulation a large fraction of events is rejected by the vertex requirement.

The total photoproduction cross section can be decomposed into four classes of diffractive processes and a non-diffractive part [70] (see section 2.5). This classification scheme is also used in the PHOJET generator. In rough agreement with [70] the simulation used in this analysis assumes the following relative contributions to the total photoproduction cross section:

$$\sigma_{ND} : \sigma_{EL} : \sigma_{PD} : \sigma_{GD} : \sigma_{DD} = 53.6 : 11.2 : 6.2 : 20.0 : 9.0$$

However, the experimental uncertainties of these numbers are large (20% to 50% depending on the type of process). Results achieved in the framework of a more recent

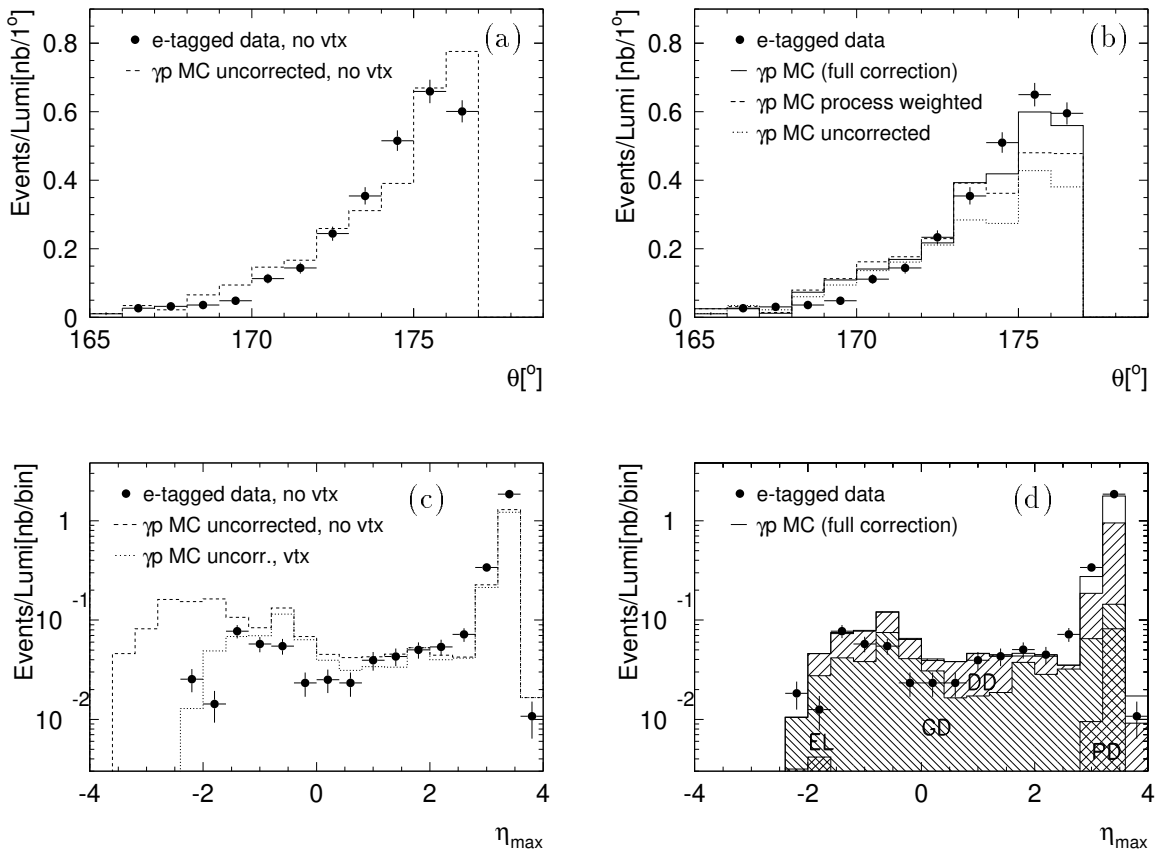

Figure 4.14: (a) Data (points) and PHOJET Monte Carlo simulation (dashed line) are compared with respect to the angular distribution of fake electrons for tagged events without vertex requirement. (b) The same distribution with vertex requirement in the data (points), the uncorrected PHOJET (dotted line) as well as the process weighted (dashed line) and the fully corrected PHOJET (solid line). (c) Distribution of $\eta_{\max}$ in the laboratory frame for the data (points) without vertex requirement and PHOJET with (dotted line) and without (dashed line) vertex requirement. (d) Composition of simulated subprocesses as a function of $\eta_{\max}$ after correction. EL, DD, GD, PD stand for elastic processes, double dissociation, photon dissociation and proton dissociation, respectively.

analysis [89] motivate a modification of the simulated cross sections. According to the recommendations process dependent weights are applied to the simulated PHOJET events, resulting in the following ratios of cross sections:

$$\sigma_{ND} : \sigma_{EL} : \sigma_{PD} : \sigma_{GD} : \sigma_{DD} = 48.4 : 10.1 : 5.7 : 15.7 : 20.1$$

The overall normalization remains unchanged. The angular distribution of the fake electrons obtained for the reweighted simulation is shown in fig. 4.14(b). Here, the vertex requirement is imposed. The corrected distribution agrees significantly better with the data than the uncorrected distribution. This suggests that at large polar angles ($\theta \gtrsim 174°$) the description of the photoproduction background is very sensitive to the choice of the relative magnitudes of the subprocesses of photoproduction.

The behavior of the different subprocesses is briefly investigated as a function of the maximum pseudorapidity $\eta_{\max}$, defined as

$$\eta_{\max} = -\ln \tan \frac{\Theta_{\min}}{2}, \tag{4.11}$$

where $\Theta_{\min}$ is the minimum measured polar angle of significant energy deposit in the detector (> 200 MeV for clusters in the Spacal). Diffractive and non-diffractive processes have different $\eta_{\max}$ distributions. In photon diffraction (GD) and elastic processes (EL) the proton stays intact and the forward region is devoid of energy ('rapidity gap'). Thus, the measured values of $\eta_{\max}$ are small or negative. In proton dissociation (PD) and double diffractive (DD) processes the proton breaks up, forming the proton remnant measured in the forward detectors and the value of $\eta_{\max}$ is large. Non-diffractive processes, in general, have larger values of $\eta_{\max}$ since there is no rapidity gap between the scattered quark jet and the proton remnant.

Fig. 4.14(c) shows the $\eta_{\max}$ distribution in the laboratory frame for tagged events without vertex requirement compared with the uncorrected Monte Carlo simulation. Contrary to the simulation the distribution of the data does not contain events with extreme values of $\eta_{\max} < -2.5$. The vertex requirement can be seen to reject all events with a large rapidity gap ($\eta_{\max} < -2.5$, i.e. $\Theta_{\min} > 170°$). This value roughly corresponds to the acceptance of the central jet chambers of the H1 detector. In the data events with a fake electron candidate at $\theta > 174°$ still have a vertex, while in the simulation this is not the case. The conclusion at this point is that the description of the hadronic final state and the different subprocesses of photoproduction and/or the tracking chamber acceptance is not fully understood in the extreme backward region.

The above investigations show that the choice of the relative subprocess cross sections has a large influence on the distribution of simulated tagged events, fig. 4.14(b). However, a satisfactory description of the data has not been achieved yet. The remaining discrepancy is effectively removed by a simple weighting of the non-diffractive component. This appears justified because a lack of events in the simulation is visible in particular at large values of $\eta_{\max}$ (fig. 4.14(c)) where the non-diffractive contribution is dominant. The chosen weights W are described as a linear function of the angle of the fake electron as $W = 1 + (\theta_{\text{fake electron}} - 173°) \cdot 0.35$. The maximum (minimum) applied weights are limited to a value of 1.7 (0.8), respectively. Since the non-diffractive contribution to the total cross section is of the order of $\sim 50\%$ an increase of the number of events by 35% is expected at large values of θ. The effect of the correction is displayed in fig. 4.14(b). The solid line shows the angular distribution of the fake electron in the PHOJET Monte Carlo simulation including both the process dependent reweighting of the diffractive components and the correction of the non-diffractive events. Reasonable agreement between the data and the simulation is achieved. In fig. 4.14(d) the decomposition of the different diffractive and non-diffractive processes is shown as a function of $\eta_{\max}$ for the corrected simulation. All selection criteria, including the vertex requirement are imposed. Comparisons of the corrected distributions with the data are also shown in fig. 4.12(b) and fig. 4.13.

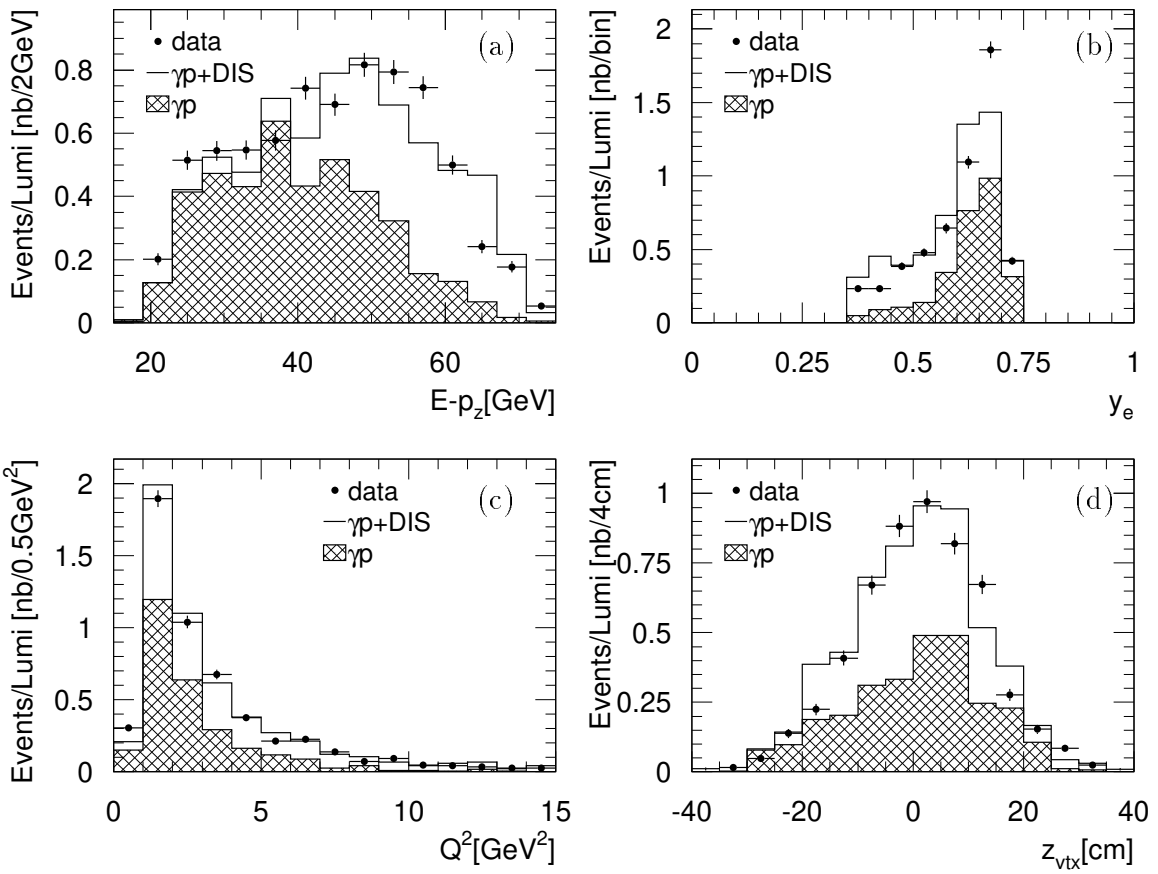

Figure 4.15: DIS events with inverted cut on the cluster radius 3.5 cm $< R_{cl} <$ 4 cm for the data (points) and the DIS+γp Monte Carlo simulation (open points). The corrected γp background simulation is represented by the hatched histogram. In (a) the distribution of $E - p_z$ is shown, (b) and (c) depict the distributions of y_e and Q_e^2. (d) shows the z-position of the reconstructed vertex.

4.8.3 Consistency Check with Rejected Events

So far, the normalization of the Monte Carlo simulation has been investigated using tagged events. The main uncertainty in the determination of the photoproduction background is given by the extrapolation from the region of the tagger acceptance at moderate values of y to the signal region corresponding to high y using the Monte Carlo simulation. In this analysis, additional uncertainties arise from the discrepancies and corrections of the Monte Carlo simulation. In the following a consistency check independent of the electron tagger requirement is performed.

An event sample with a large contamination from photoproduction background is selected by demanding that the cluster radius R_{cl} be larger than 3.5 cm and less than 4 cm. All DIS selection criteria except the cut on $E - p_z$ and the cluster radius R_{cl} (cuts # 9 and # 3 in table 4.1) are imposed. As shown in section 4.6 the fraction of DIS events with $R_{cl} > 3.5$ cm is small, thus the photoproduction contribution is enhanced. The cluster radius is to first order independent of the event kinematics or

topology. Consequently, the events selected here have properties very similar to other photoproduction events in the DIS sample.

Data and corrected DIS+γp Monte Carlo simulation are compared in the range of $y_e > 0.35$ where the photoproduction background becomes significant. Fig. 4.15(a) shows the distribution of $E - p_z$ to which the data and the γp+DIS Monte Carlo simulation agree reasonably well. The simulated contribution from photoproduction amounts to more than 50% of the event sample and thus provides good sensitivity to mismatches between the photoproduction background in the data and the Monte Carlo expectation. In fig. 4.15(b) and (c) the distributions y_e and Q_e^2 are shown, respectively, and in (d) the distribution of the reconstructed event vertex is shown.

In general the Monte Carlo simulation agrees very well with the data. The most prominent discrepancy is visible in fig. 4.15(b) in the bin of $0.65 \leq y_e \leq 0.7$. Here the simulation undershoots the data by approximately 30%. For the measurement of F_2 an uncertainty of 30% is therefore assigned to the normalization of the subtracted photoproduction background.

4.9 Radiative Corrections

The Born cross section from which the structure function F_2 is extracted describes ep scattering to lowest order perturbation theory as shown in fig. 1.1. In contrast, the experimentally measured cross section includes all orders of electroweak interaction diagrams. For the correct extraction of the structure function F_2 from the measured cross section it is therefore necessary to correct for contributions from higher order processes. A detailed description of radiative corrections can be found in [90].

4.9.1 Outline of QED Radiation

The largest contributions to the correction arise from QED processes to first order in α, where a bremsstrahlung photon is radiated from the electron or the proton, and from QED vertex corrections. Depending on whether the photon is radiated from a quark in the proton or from the electron one can distinguish between 'quarkonic' and 'leptonic' photon radiation. Relative to leptonic radiation quarkonic radiation is suppressed by the quark charge squared and the inverse of the quark mass squared. Interference terms including also box diagrams of γ and Z^0 exchange, contribute less than 1% to the correction. Self energy corrections due to vacuum polarizations are usually absorbed in the running of the QED coupling constant α. At low and moderate values of $Q^2 < 100$ GeV^2 (as in this analysis) weak interaction diagrams can be neglected since their matrix element is suppressed by the squared masses of the interaction bosons Z^0 and $W^{\pm}$ in the propagator term.

The leptonic photon radiation processes significantly dominate the corrections. They are described in the leading logarithmic approximation by the two Feynman diagrams

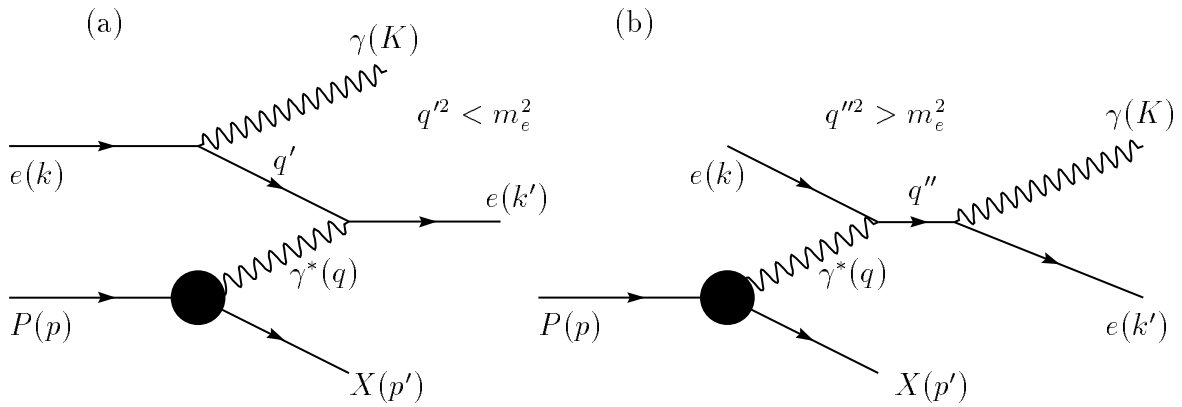

Figure 4.16: The most relevant Feynman diagrams of the process $ep \to ep\gamma$. (a) initial state radiation, (b) final state radiation. $P(p)$, $e(k)$ denote the four-momenta of the incident particles. $X(p')$, $e(k')$, $\gamma(K)$ refer respectively to the hadronic final state, the scattered electron and the radiated photon. q^2 (q'^2, q''^2) give the four momentum squared of the virtual photon (electron).

in fig. 4.16 (a) and (b) commonly called initial state radiation (ISR) and final state radiation (FSR) respectively. p, k, p' and k' denote the four-momenta of the incoming proton and electron, and the outgoing hadronic final state and the electron. q is the four-momentum transfer carried by the virtual interaction photon and q', q'' refer to the four-momenta of the inner electron lines. The four-momentum of the radiated photon is denoted by K. The cross section of photon radiation becomes particularly large for collinearly radiated photons due to singularities in the kinematic limits of the four-momentum distribution. Experimentally one distinguishes between different event classes in the detector [91]:

- **Bethe-Heitler Processes:** Due to the singularity of the matrix element in the limit of $q^2 \to 0$, $q'^2, q''^2 \to m_e^2$ most radiative events have both electron and radiated photon scattered at very small angles. The case of elastic scattering (in the limit of $y \to 0$) is called the Bethe-Heitler process (BH) [34]. Due to the small scattering angles, both electron and radiated bremsstrahlung photon as well as the proton disappear through the beam pipe. The BH cross section is very large – the part visible in the acceptance of the luminosity system amounts to $\sim$ 70 mb [35] – and can be calculated within QED in the relativistic limit to very high accuracy. For this reason BH events are used as the reference for the H1 luminosity measurement using the electron and photon detectors in the HERA tunnel (see also sections 2.2 and 4.8).

- In **QED Compton Processes** the negative momentum transfer squared $-q^2$ of the virtual photon is small compared to $|q'^2|$ and q''^2 of the radiated (real) photon – electron system. The QED Compton signature is given by two electromagnetic

clusters in the backward region which are coplanar ($\Delta\phi \approx 180°$). In elastic and most inelastic QED Compton events the rest of the detector is empty so that no tracks are reconstructed. Since in this analysis a reconstructed vertex is required the background from QED Compton events is negligible.

- In **Radiative DIS Events** a photon of high energy is radiated from the incoming or outgoing electron. Due to the singularities of the matrix element at $q'^2 = 0$ and $q''^2 = 0$ photons are dominantly radiated collinear with the electrons. The four-momentum transfer, Q^2, of the virtual photon is large enough ($-q^2 = Q^2 \gg 0$) for the electron to be detected in the main detector. Radiative DIS events are therefore contained in the selected DIS event sample. For the Born diagram the kinematics calculated at the electron-photon vertex (leptonic) and the proton-photon vertex (hadronic) are equal. In contrast, the kinematics of radiative events are reconstructed differently depending on the chosen reconstruction method (see section 2.4). Since leptonic radiation is dominant the electron method has the largest corrections to the measured cross section ($\delta_{RC} \sim 50\%$ at $y_e \sim 0.7$). The loss of electron energy due to the radiation of an (undetected) photon results in an overestimation of y_e and thus in the migration of the event towards larger values of y and Q^2 compared to the true underlying event kinematics. Hadronic reconstruction methods are mainly affected by the quarkonic corrections which are at the level of 4%. In this analysis the Monte Carlo generator program DJANGO [58] is used to correct the measured cross section to the Born level. DJANGO accounts for the radiation of a real photon to lowest order in α in both ISR and FSR processes (see section 2.5).

Experimentally, radiative events can be defined as ISR or FSR on the grounds that the radiated photon is predominantly collinear with the electron. In initial state radiative events the bremsstrahlung photon typically escapes through the backward beam pipe and is not detected in the central detector. The definition used in the context of the investigation presented in section 4.9.2 follows the information about the 'mother' particle of the photon available on the generator level of DJANGO. An event is classified as ISR (FSR) if the radiated photon originates from the incident (scattered) electron, respectively. The cut-off energy for the simulation of radiated photons is 20 keV.

Analytical programs, in particular the package HECTOR [92], have been used [93] to investigate the description of radiative processes and the resulting radiative corrections implemented in DJANGO. The total systematic error amounts to 2% due to theoretical uncertainties in the influence from higher order processes which are not implemented in DJANGO as well as quarkonic corrections. At $Q^2 \leq 0.65$ GeV^2 (measured in the shifted vertex data analysis) an error of 5% is assigned due to uncertainties of the structure function F_2 and R at very small Q^2 and the absence of soft photon exponentiation in DJANGO [94].

4.9.2 Investigation of QED Final State Radiation

While in ISR processes the radiated photon escapes from the detector, final state radiated photons typically appear in the vicinity of the scattered electron in the electron detector. Former analyses, using the BEMC calorimeter, have neglected the influence of FSR events. Due to the granularity of the BEMC electron and photon were generally measured in the same cluster. Separation of the two clusters was only feasible above an opening angle between electron and photon of 6°, corresponding to a distance in the BEMC of roughly 16 cm [95]. In contrast, the granularity of the Spacal and the cluster algorithm used allows to separate clusters above a distance of 7 cm. This is shown in fig. 4.17(a), where the fraction of simulated events with two electromagnetic clusters classified as FSR is plotted as a function of the distance between scattered electron and radiated photon in the Spacal plane. At 7 cm the onset of the cluster separation is visible. This value roughly corresponds to the minimum distance between the centers of non-neighboring cells in the electromagnetic Spacal. The fraction of events below 7 cm is due to events where electron and photon appear in the same cluster and the second cluster is produced by the hadronic final state. With the improved single particle separation of the Spacal the fraction of measurable FSR processes is significantly increased compared to former measurements. Since the kinematic reconstruction of the events is based on the electron identification, the separation of the electron and the FSR photon leads to migrations to smaller values of Q^2 and x. It is therefore necessary to investigate whether the Monte Carlo simulation correctly describes the distribution of events with separated electron and photon candidates.

Events are selected with at least two electromagnetic clusters in the Spacal. In addition all standard DIS selection criteria as given in table 4.1 are imposed. The cluster with the second highest energy is assumed to belong to the radiative photon. The photon candidate must have an energy of at least 2 GeV and a cluster radius of less than 3.5 cm. No track requirements are imposed. Apart from the two electromagnetic clusters the Spacal is required to be empty, events are therefore rejected if the total energy in the Spacal (Electromagnetic + Hadronic section) outside the two electromagnetic clusters is larger than 1.5 GeV. The contribution from initial state radiative events is reduced by applying a cut on $E-p_z > 45$ GeV. The contamination from backward hadronic energy flow is suppressed selecting events in the kinematic region of moderate inelasticities $0.05 < y_{\mathrm{JB}} < 0.4$. In this region photoproduction background is negligible. In FSR, contrary to QED Compton, electron and photon are typically situated in the same azimuthal hemisphere. In the framework of this technical study events with $\Delta\phi > 90°$ are rejected. Note that most QED Compton events are rejected due to the vertex requirement. Fig. 4.17(b) depicts the distribution of the energy sum of the electron and photon clusters for the selected events. The contribution from non-radiative events in the selected sample where at least one of the two electromagnetic clusters is produced by the hadronic final state is very small. The energy distribution of the second cluster is shown in fig. 4.17(c). Finally in fig. 4.17(d) the distance between the electron and

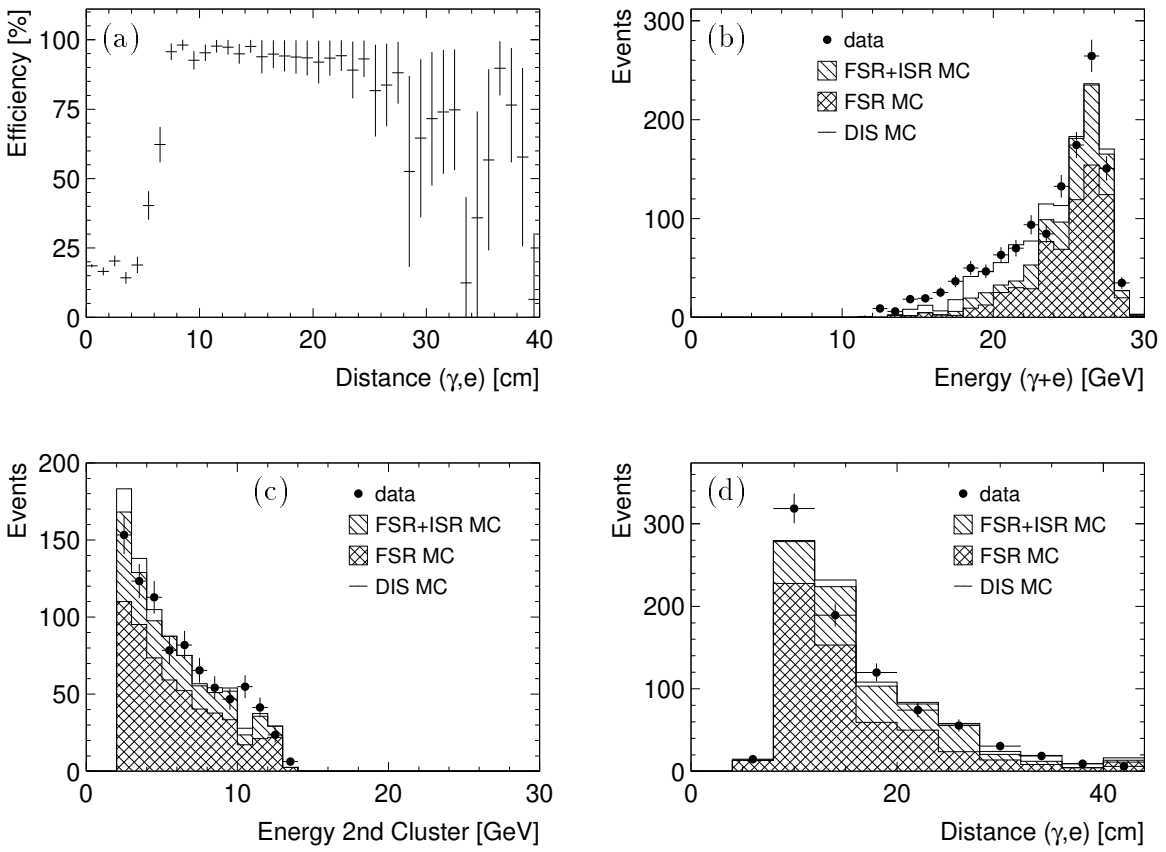

Figure 4.17: (a) Fraction of FSR events with two separate electromagnetic clusters in the Spacal as a function of the distance between the photon and the electron as determined from the Monte Carlo simulation. (b) The sum of the electron and the photon energy in the data (points) and in the Monte Carlo simulation (solid line). The dark hatched histogram shows the true FSR contribution as classified on Monte Carlo generator level. The light hatched histogram refers to events classified as ISR. (c) Energy distribution of the second electromagnetic cluster. (d) Distribution of the distance between the electron and the photon candidate.

the photon in the plane of the Spacal is depicted. In (c) and (d) the sum of the energies of the electron and the photon are required to be larger than 23 GeV.

In summary, it has been shown that the process of QED final state radiation can be resolved with the Spacal. The investigations prove that the Monte Carlo generator DJANGO describes the data within the present level of precision. The fraction of resolved FSR events in the DIS sample is of the order of 0.5%. The total fraction of FSR events in the DIS sample amounts to 30% roughly. In the selected region of phase space FSR events form the main contribution to the cross section for events where two electromagnetic clusters are present.

4.10 Kinematic Distributions

In this section the selected event sample is presented by showing the fundamental kinematic distributions used in the measurement of the double differential cross section and the structure function F_2. For the distributions shown all cuts of table 4.1 are imposed. In addition events with $y_{\mathrm{JB}} < 0.05$ are rejected. The latter cut is used to suppress the region where the Monte Carlo simulation does not reproduce the vertex reconstruction efficiency of the data (see section 4.5). Data and Monte Carlo simulation are normalized to the integrated luminosity.

In fig. 4.18(a) the distribution of the energy of the scattered electron is shown, in fig. 4.18(b) its polar scattering angle θ_e. The upper edge of the θ_e distribution is due to the fiducial cut on the detector acceptance at a radius of 8.7 cm (see section 4.7).

One of the reconstruction methods used in this analysis to derive the Lorentz invariant quantities Q^2 and y is the electron method (section 2.4). The distribution of Q_e^2 is shown in fig. 4.18(c). Events with Q_e^2 larger than 25 GeV are accumulated in the overflow bin. The distribution of y_e is presented in fig. 4.18(d). Since events with $y_{\mathrm{JB}} < 0.05$, corresponding to $\log_{10}(y_{\mathrm{JB}}) < -1.3$ are rejected the distribution of y_e rapidly decreases towards smaller values. The long tail is due to the different behavior of y_e and y_{JB}. The sharp edge at a value of -0.15 is due to the energy cut of 8 GeV for the scattered electron.

An alternative reconstruction method used in this analysis is the Σ method. The distributions of Q_Σ^2 and y_Σ are shown in fig. 4.18(e) and (f), respectively. The sharp drop in the distribution of $\log_{10}(y_\Sigma)$ at a value of -1.3 reflects the cut $y_{\mathrm{JB}} < 0.05$. At high values of y_Σ the energy cut of 8 GeV is visible as a comparably soft threshold. In both reconstruction methods x is calculated via $x = Q^2/sy$.

Fig. 4.19(a) shows the distribution of the ratio y_Σ/y_e. The tail at low values mostly contains ISR events where y_e is overestimated. The tail at high values is mainly due to the detector resolution. The agreement between the data and the DIS+γp Monte Carlo indicates that the hadronic final state is reasonably well reproduced in the Monte Carlo simulation. Furthermore, it gives confidence that the resolutions of both y_Σ and y_e are well understood and that the calibrations of electromagnetic and hadronic energies are consistent. This is particularly important for the use of the Σ method. Fig. 4.19(b) shows the ratio of the transverse momenta of the scattered electron and the hadronic final state $p_{\perp,h}/p_{\perp,e}$. Good agreement between the data and the Monte Carlo simulation is found. The large width of the distribution is due to the fact that the data sample is dominated by events with low Q^2. Since the transverse momenta in such events are small on average already small fluctuations of the measured energies can have a large effect on the ratio.

Details of the hadronic final state distributions in the simulation are briefly investigated. The individual share of hadronic energy between the different detector components is measured and the relative contribution to the measured value of y_Σ is plotted.

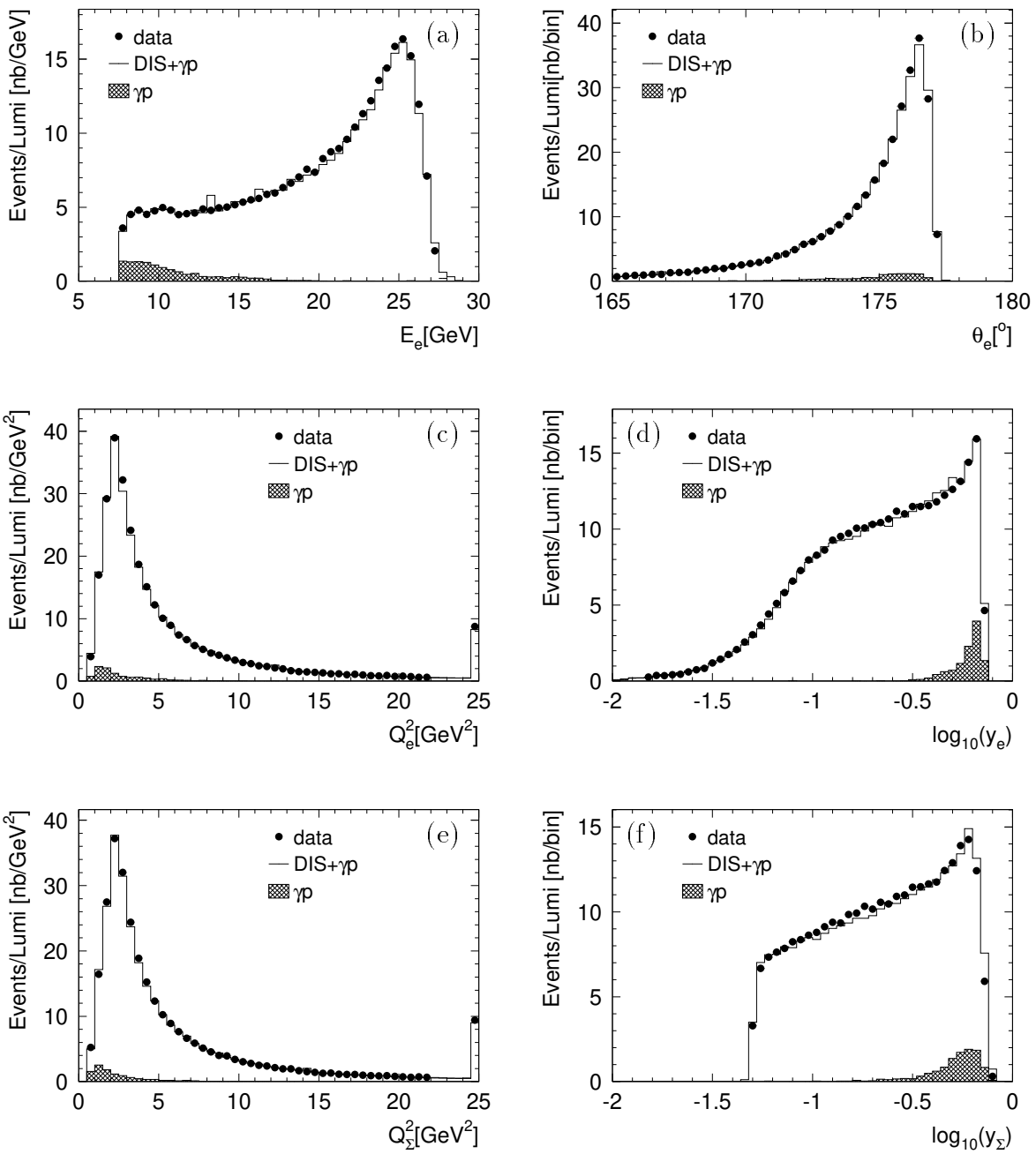

Figure 4.18: Data (points) and DIS+γp Monte Carlo simulation (solid line) are compared using different kinematic quantities. (a) shows the energy distribution and (b) the polar angle of the scattered electron θ_e. (c) and (d) depict the distributions of Q^2_e and $\log_{10}(y_e)$, respectively, as reconstructed using the electron method. In (e) and (f) the kinematic variables Q^2_Σ and $\log_{10}(y_\Sigma)$ obtained with the Σ method are shown. In all figures the hatched histogram represents the simulated photoproduction background.

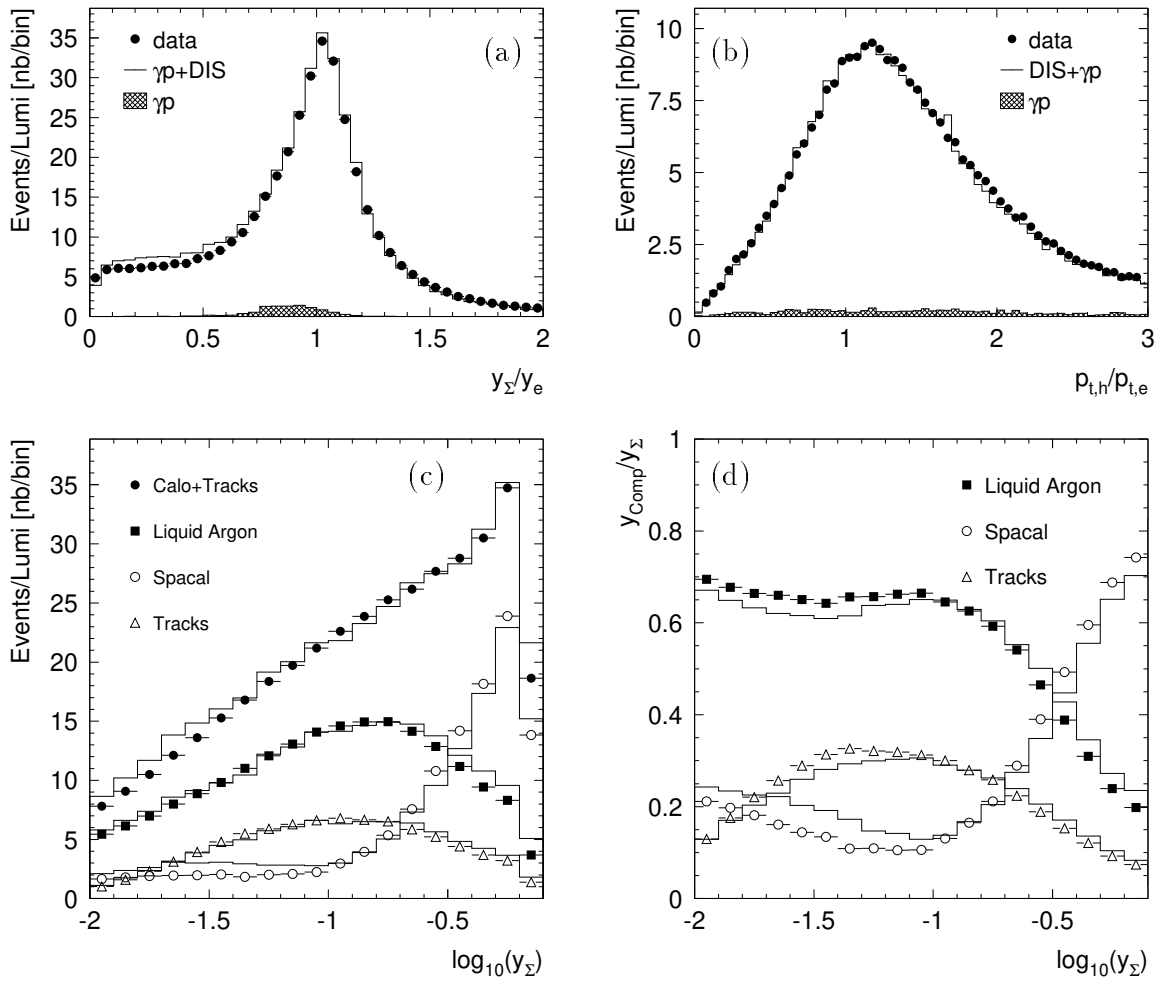

Figure 4.19: Data (points) and Monte Carlo simulation (solid lines) are compared with respect to the measurement of the hadronic final state. (a) shows the ratio y_Σ/y_e. (b) depicts the ratio of the transverse momenta of the hadronic final state and the scattered electron $p_{\perp,h}/p_{\perp,e}$ as determined using the calorimeters. The hatched histogram represents the simulated photoproduction background. In (c) and (d) the contribution to the measured value of $\log_{10}(y_\Sigma)$ is shown. (c) The overall distribution is shown by (full points). Also shown are the contributions from the different detector components, namely the Liquid Argon Calorimeter (full squares), the Spacal (open points) and the track chambers (triangles). In (d) the relative contribution of the Liquid Argon Calorimeter (full squares), the Spacal (open points) and the track chambers (triangles) are shown. The solid lines in (c) and (d) represent the respective distributions obtained by the Monte Carlo simulation.

Fig. 4.19(c) shows the distributions of $\log_{10}(y_\Sigma)$ from the different detector components. Note that here the cut on $y_{\rm JB} < 0.05$ is removed. The contributions measured in the Liquid Argon Calorimeter, in the Spacal and in tracks are obtained by weighting each event according to the fractions of y_Σ measured in the respective detector component. Fig. 4.19(d) shows the relative fractions of y_Σ in the Liquid Argon Calorimeter, the Spacal and tracks. In the Spacal substantial contributions from hadrons are seen at values of $y_\Sigma \gtrsim 0.1$ continuously rising towards larger values. Discrepancies at the few percent level appear in the region of very low y and at high y. Note that discrepancies at this level are to first order not important to this analysis since the measurement depends only on the description of the total distribution of y_Σ. The fact that at high y the measured hadronic energy flow in the Spacal is larger than expected in the simulation is possibly due not only to an imperfect simulation of the hadronic final state on generation and/or simulation level, but also to the underestimation of preshowering processes in the Monte Carlo simulation. The scattered electrons are typically accompanied by a 'halo' of low energy particles which may form clusters in the Spacal separate from the electron cluster. These clusters are counted as hadronic and thus increase the fraction of y_Σ measured in the Spacal. Note that the energy calibration is not directly affected as long as the same cluster algorithm is used in both the calibration procedure and in the analysis.

4.11 Summary

In this chapter the event selection has been presented. The selection criteria, based on the identification of the scattered electron, are discussed in detail and the measurement of the polar angle of the scattered electron is described. Comparisons of the data with Monte Carlo simulations are performed. Substantial corrections to the Monte Carlo simulations are found necessary in particular in the description of the radial distribution measured in the BDC and of the photoproduction background. The tuned Monte Carlo simulation has been proven to agree well with the data. In conclusion, the detector response is well understood, allowing a precise extraction of the structure function $F_2(x, Q^2)$ as presented in the following chapter.

Chapter 5

Measurement of the Structure Function $F_2(x, Q^2)$

In general, the structure function $F_2(x, Q^2)$ is measured by determining the Born cross section in bins of x and Q^2. In section 4.1 the particular method chosen in the present analysis is described. In this method the tuned Monte Carlo simulation is used to describe the properties of the detector and to account for all necessary corrections to the data. The investigations performed in the previous chapter have shown that the corrected Monte Carlo simulation is in good agreement with the data. According to equation (4.6) the structure function F_2 will now be extracted from the data.

In section 5.1 the analysis bins are defined. A summary of the systematic uncertainties is given in section 5.2. The result of the measurement is presented in section 5.3. Finally, the structure function F_2 and the total virtual photon proton cross section are compared with previous results and with model predictions (section 5.4).

5.1 Defining the Analysis Bins

It is necessary to define the binning, i.e. the intervals in the kinematic plane of x and Q^2, in which the measurement of the double differential cross section and F_2 is performed. In general, the binning should be chosen such that the following criteria are optimally satisfied.

- The correlations between different bins should be minimized. In order to limit the number of events migrating in and out of the bin, the bin size should be chosen to be larger than the detector resolutions δQ^2 and δx.
- The number of selected events in a given bin should be large enough to keep the statistical error smaller than the systematic error.
- Most systematic uncertainties (such as the energy calibration of electron and hadrons, the detector resolution, trigger- and vertex reconstruction efficiency

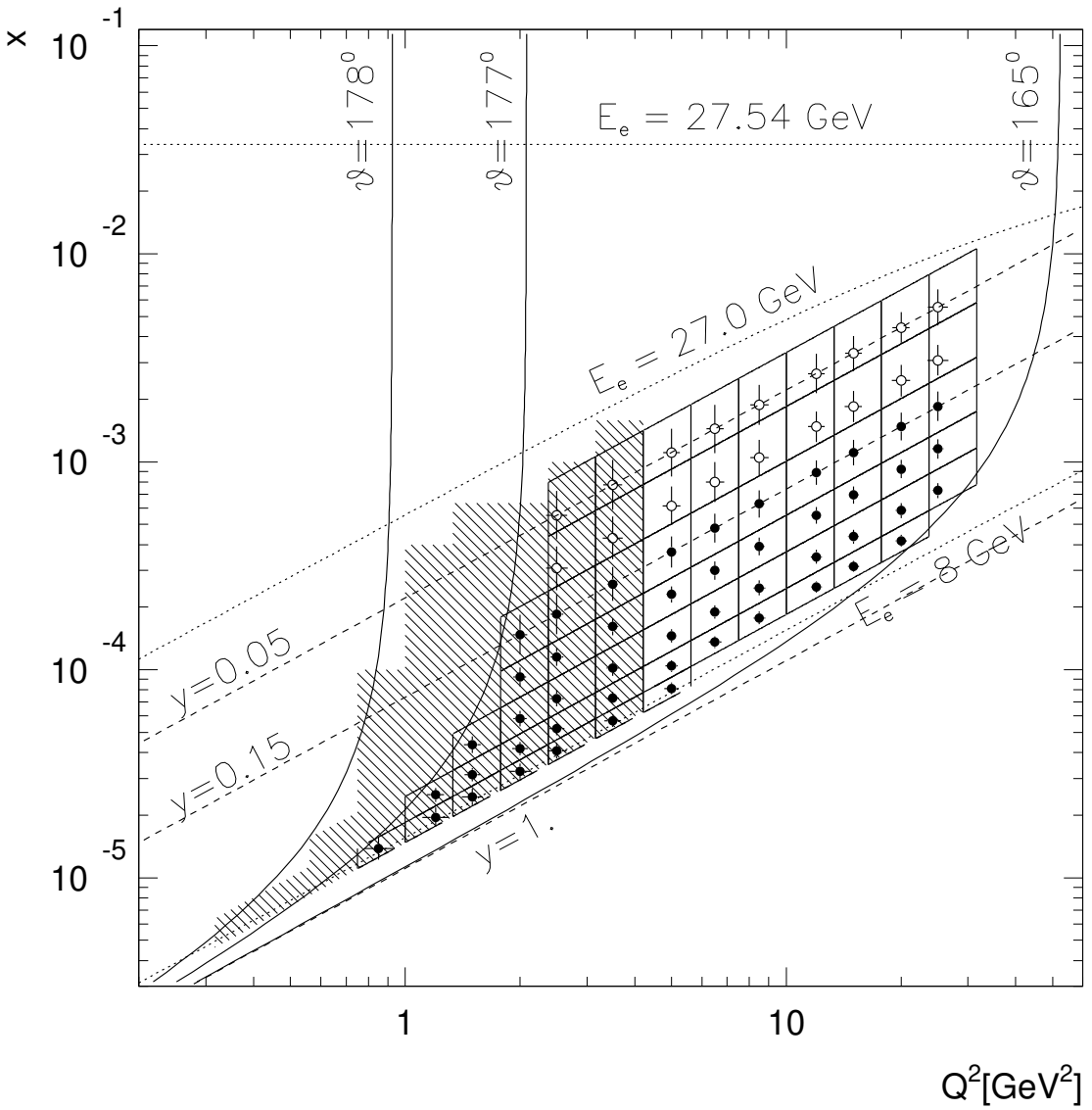

Figure 5.1: Kinematic plane of x and Q^2. The binning used for this measurement is shown by the diamonds. The points denote the chosen central values of the bins. Full (open) points indicate the bins where the electron (Σ method) is used respectively. The hatched histogram shows the region of the measurement with shifted vertex data. Also shown are lines of constant electron energy E'_e, polar angle θ_e and inelasticity y.

etc.) scale with y rather than x. Since the precision of this analysis is dominated by systematic uncertainties it is preferable to choose a $y - Q^2$ binning which allows the width of the bins to be adjusted to suit the experimental conditions.

Consequently, in this analysis a $y-Q^2$ binning is chosen with increased bin size towards smaller values of y according to the deterioration of the y-resolution. The bin width and the central values in Q^2 are chosen as in previous analyses of the H1 collaboration [15, 25] in order to allow for easy comparisons.

Fig. 5.1 shows the kinematic plane as a function of Q^2 and x in a logarithmic scale. The region of detector acceptance for the data recorded in 1995 is illustrated by the lines of constant polar angle. The hatched area indicates the kinematic region explored in the measurement with shifted vertex data which reaches up to polar scattering angles of 178°. The acceptance region for the data with nominal vertex position is limited to polar angles below 177°. The grid indicates the boundaries of the bins used in this analysis. The central values chosen for the measurement are marked by points. Full (open) points refer to bins where the electron (Σ) method is used for the reconstruction of the event kinematics (see section 2.4). In the region with $y \geq 0.15$ the electron method is used while at smaller values of y the Σ method is preferred. No measurement is performed in the region where y at the bin center is smaller than 0.05. In this region the vertex reconstruction efficiency is not completely understood (see section 4.5). The error bars for each bin illustrate the resolutions δQ^2 and δx of the respective reconstruction method as determined using the Monte Carlo simulation of non-radiative events. Towards smaller values of y, i.e. larger values of x, the expected significant deterioration of the resolution δx is visible.

Also shown are lines of constant energy of the scattered electron. Events with an electron energy of 27.54 GeV are situated at a value of $x = 0.0336$ ($= E_e/E_p$), independent of Q^2. Also shown is the line of 27.0 GeV scattered electron energy. Towards small values of Q^2 the x values corresponding to this energy decrease, thus opening up a large region of phase space between this energy and the beam energy. The projection of this region onto the energy of the scattered electron appears as a prominent enhancement around the electron beam energy, known as the kinematic peak (see section 3.1). In this region a small variation of the electron energy implies a large difference in the value of x. Thus, the resolution $\delta x/x$ of the electron method severely deteriorates when approaching the beam energy (see section 2.4).

The magnitude of the migrations of events between different bins can be quantified by the 'acceptance' and the 'stability'. The calculation of these quantities is performed using the Monte Carlo simulation of non-radiative DIS events.

- The stability denotes the fraction of simulated events which are reconstructed in the same bin as they were generated in. In fig. 5.2 the stability is shown as a function of y. At large y the stability of the electron method is clearly superior, rapidly deteriorating towards low y, i.e. large x. At small values of y the Σ method is in general more stable. Here, also bins are shown which are excluded from the measurement of F_2. The combination of the two reconstruction methods for the measurement ensures that the stability is larger than 50% in all analysis bins.

- The acceptance is defined as the ratio between the number of events actually measured (reconstructed) in a given bin and the number of events generated according to the cross section in this bin. The acceptance can become larger than unity due to migration effects. Fig. 5.3 depicts the acceptance as a function

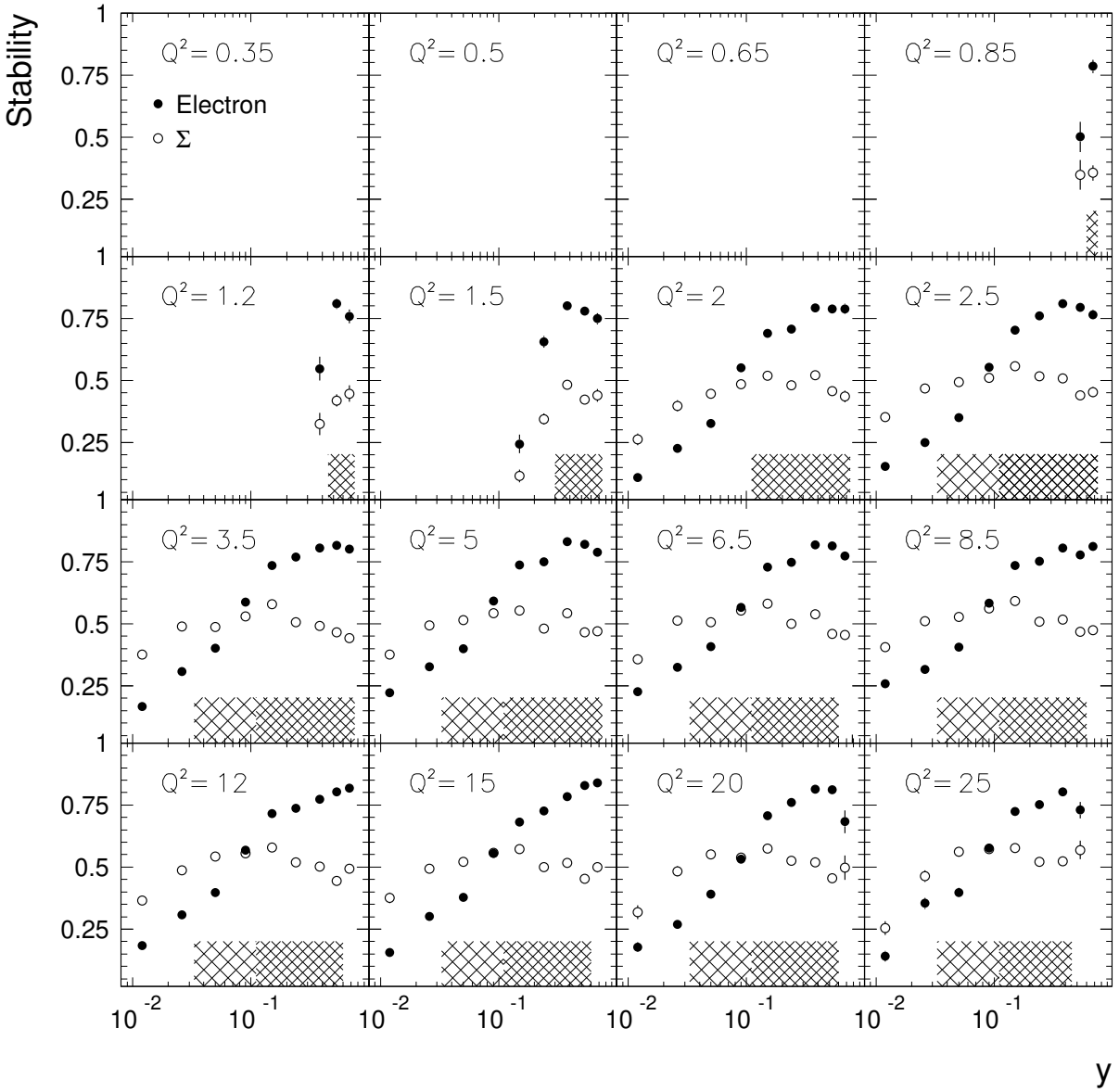

Figure 5.2: The 'stability' (definition see text) as a function of y in different bins of Q^2 for the electron method (full points) and the Σ method (open points). The dark (light) hatched area indicates the region of y where the electron (Σ) method is used for the measurement. The bins outside the hatched area are not included in the final result.

of y for the two reconstruction methods, the electron and the Σ method. A flat behavior is observed for both methods. In the bins used in the measurement the acceptance deviates by less than 10% from unity. This behavior is mainly due to the cut on $E - p_z > 35$ GeV (Cut # 9 in table 4.1). By removing this cut the fraction of events with initial state radiation in the event sample is strongly increased (see also fig. 4.7(c)). For ISR events the reconstructed value of y_e, as

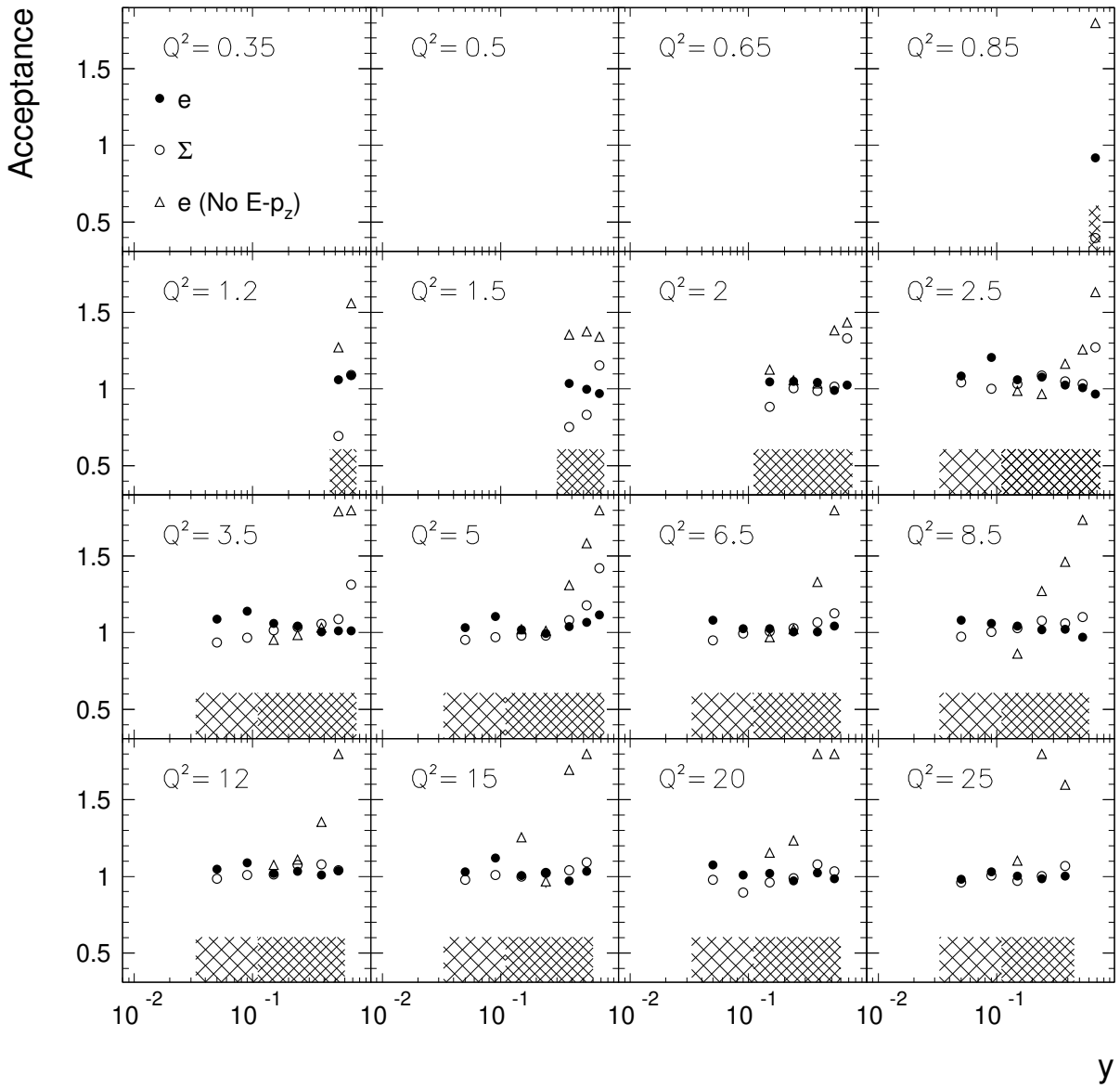

Figure 5.3: The 'acceptance' (definition see text) as a function of y in different bins of Q^2 for the electron method (full points) and the Σ method (open points). The dark (light) hatched area indicates the region of y where the electron (Σ) method is used for the measurement. For the bins where the electron method is used the acceptance is shown for a sample of simulated events with the cut $E - p_z > 35$ GeV removed (triangles). In the figure points with an acceptance of larger than 1.8 are manually set to 1.8.

reconstructed using the electron method, is overestimated, leading to an increased acceptance in the region of the measurement rising towards large values of y.

5.2 Systematic Errors

The different sources of systematic uncertainty, which have been discussed in detail in the sections 4.4 – 4.8, are summarized.

1. **The absolute energy scale of the scattered electron** is known to the level of 0.7% for electrons scattered with 27.5 GeV and 2.5% at 8 GeV (section 3.3.3). For the shifted vertex data the uncertainty is 1% at 27.5 GeV and 3% at 7 GeV. The resulting uncertainty on the measurement of the structure function F_2 is estimated by increasing and decreasing the absolute energy scale of the electron assuming a linear behavior of the energy scale uncertainty between 2.5% at 8 GeV and 0.7% at 27.5 GeV. Fig. 5.4(a) shows the influence of a downward miscalibration within the energy scale uncertainty on the measured cross section as a function of y_e. In the medium y_e-range the uncertainty is at the level of 1 to 2% rising sharply to the level of 7% at the smallest values of y_e. Note that at $y < 0.15$ the Σ method is used for the measurement which is less sensitive to miscalibrations of the electron energy.

2. **The hadronic energy scale** of the Spacal is calibrated to better than 7% (section 3.6). The energy scale of hadrons in the Liquid Argon Calorimeter is known to 4% [31]. Fig. 5.4(b) shows the influence of a potential overestimation of hadronic energies in the Spacal by 7% on the measurement of F_2 using the electron method. It is less than 1% and mainly arises from the selection cut on $E - p_z > 35$ (cut # 9 in table 4.1).

3. **The trigger efficiency** is determined from the data (section 4.4). In general it is above 99%. Small extra corrections at the level of 2% are applied for some of the bins at high values of y, especially at small Q^2, corresponding to the very inner region of the Spacal. The losses due to the ToF veto conditions used on the first trigger level L1 amount to $1\% \pm 0.5\%$. Inefficiencies due to potential problems of the event filtering software at the trigger levels L4 and L5 are found negligible ($\ll 0.1\%$).

4. **The vertex reconstruction efficiency** is measured. The Monte Carlo simulation reproduces the data to better than 2% (section 4.5) in the region above $y_e \gtrsim 0.06$. This value of 2% is assigned as a systematic error to the result of F_2 in all bins of the measurement.

5. **The BDC electron track finding efficiency** is larger than 98% (96%) in the inner (outer) region. This behavior is reproduced in the Monte Carlo simulation to better than 1% (section 4.7.1) [27].

6. **Potential angular misalignments** leading to shifts of the measured polar scattering angle of the electron θ_e are smaller than 0.5 mrad (section 4.7) [27]. The resulting uncertainty of the measurement of F_2 is illustrated in fig. 5.4(c).

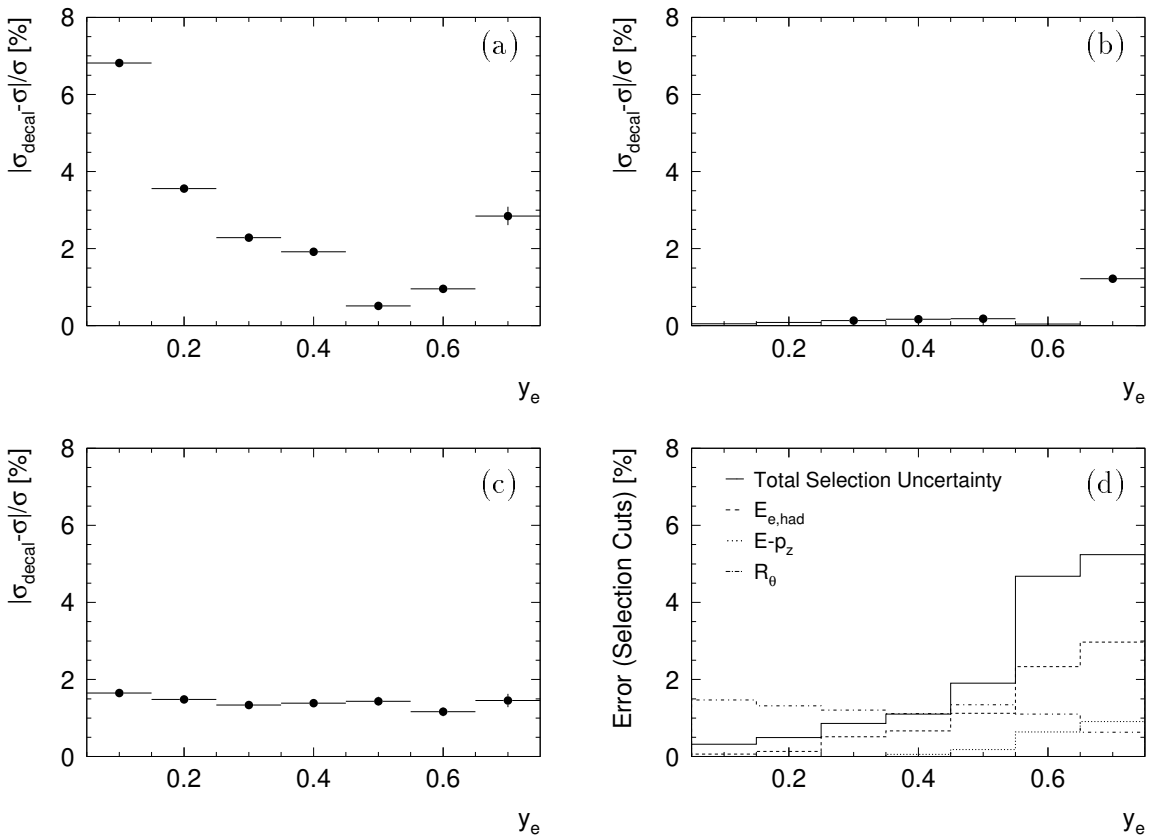

Figure 5.4: Deviation of the measured cross section as a function of y_e if (a) the electron energy is miscalibrated within the energy scale uncertainty by -0.7% at 27.5 GeV and -2.5% at 8 GeV, (b) the hadronic energy scale in the Spacal is miscalibrated by -7%, (c) the polar angle of the scattered electron is shifted by +0.5 mrad. (d) Uncertainty introduced by the selection cuts. Explicitly shown are the influences of the selection cuts $E_{e,had}$ (dashed line) and $E - p_z$ (dotted line). Separately shown is the effect of the fiducial cut (dashed-dotted line).

7. **In the radial region between 22 cm $<$ R $<$ 28cm** additional uncertainties on the scattering angle arise due to spatial variations of the dead material and/or BDC detector problems in the transition region of the BDC (section 4.7.4). The systematic error is estimated using the difference of the F_2 result obtained with the corrected and the uncorrected Monte Carlo simulation. It amounts to 2% at maximum and affects the bins with $Q^2 \geq 12$ GeV^2 only.

8. **The uncertainty of the electron selection efficiency** is determined for the selection cuts # 3 – 9 as listed in table 4.1 (see also section 4.6 and 4.7). It is calculated using the DIS Monte Carlo simulation as 30% of the fraction of events lost due to the respective cut. For the $E-p_z$ cut only the non-radiative events are taken into account. Fig. 5.4(d) shows the combined uncertainty from all electron selection cuts. The largest contributions to the uncertainty come from the cut on the hadronic energy behind the electron candidate in the Spacal $E_{e,had} < 0.5$ GeV

and the cut on $E - p_z > 35$ GeV. Separately shown is the influence of the fiducial cut $R_\theta > 8.7$ cm. This cut is relevant only for the Q^2 bins below 2 GeV^2.

9. **The uncertainty on the photoproduction background** subtraction is estimated to 30% (section 4.8). Only the bins at large y are contaminated by photoproduction background of more than 5%. In no bin is the contribution larger than 20% of the DIS signal. The resulting uncertainty of the measurement of F_2, consequently, is smaller than 6% everywhere.

10. **The beam induced background** in the final event sample is estimated to be less than 1%.

11. **The theoretical uncertainty on the amount of QED radiative corrections** is below 2% (section 4.9). For bins with $Q^2 \leq 0.65$ GeV^2, measured in the shifted vertex analysis, a systematic error of 5% is assigned due to uncertainties of hadronic as well as higher order corrections which are not simulated in DJANGO. The error also accommodates possible influences from the region of very low Q^2 where the structure function is unknown [93] (section 4.9).

12. **A global normalization uncertainty** arises from the error on the measurement of the integrated luminosity and the correction for the rejection of proton satellite bunches. In this analysis it is 1.5% (3.0%) for the nominal (shifted) vertex data [35] (see also section 4.5).

The systematic uncertainties of each analysis bin can be divided into a correlated and an uncorrelated component. The distinction is relevant in particular for the use of the results in QCD analyses and phenomenological parametrizations of the data. In general, the correlation of the systematic errors between different bins is difficult to estimate. However, since possible miscalibrations affect different bins in a similar way the uncertainty of the absolute energy scale (listed above in the paragraphs 1 and 2) and potential shifts of the angular measurement (paragraph 6) are assigned to the correlated systematic error while all other systematic uncertainties are taken to be uncorrelated. The total systematic error is obtained by adding the correlated and the uncorrelated components in quadrature.

The statistical error includes both the data and the Monte Carlo simulation. The number of events which satisfy the full set of selection cuts as given in table 4.1 is 344590 (1287) in DJANGO (PHOJET), respectively, compared to 221017 in the data. The figures indicate that the statistical uncertainty could be reduced by the use of a larger number of simulated events[1]. In particular the lack of simulated photoproduction events is an important source to the uncertainty of the measurement in particular at large values of y.

The total experimental uncertainty is obtained by adding the systematic and the statistical errors in quadrature.

[1]The corresponding values of integrated luminosity are given in the sections 2.5 and 4.4.

5.3 Results

The proton structure function F_2 is evaluated at the central values x and Q^2 of each bin using equation (4.6). Fig. 5.5 shows the result of the measurement. F_2 is presented as a function of x in different bins of Q^2 between 0.85 GeV^2 and 25 GeV^2, separately for the electron and for the Σ method. The error bars represent the statistical error only. The agreement of the two systematically different methods shows that the experimental uncertainties of the measurement are well controlled. The comparison is in particular sensitive to possible miscalibrations of the energy scale and wrong estimations of the radiative corrections. The curves show the parametrization of F_2 obtained from the global H1 QCD fit [15] (see also section 1.4). This parametrization is used for the description of the structure function in the Monte Carlo simulation. For very small values of x ($x < 10^{-5}$) and for $Q^2 \leq 1$ GeV^2 the F_2 values of the parametrization are set constant. Due to the excellent agreement of the data with the assumed parametrization further iterations are not necessary.

The final result is obtained using the electron method for the region with $y \geq 0.15$ and the Σ method for the bins with $0.15 > y \geq 0.05$. The division of the bins between the two methods are shown in fig. 5.1. Points with $y < 0.05$ are not displayed since at low y the vertex reconstruction efficiency is not sufficiently well described in the Monte Carlo simulation (see section 4.5).

Fig. 5.6 shows the final result of the measurement of F_2. The error bars represent statistical and systematic errors added in quadrature. The global normalization uncertainty of 1.5% is not included. Also shown are the results of the H1 Collaboration from the measurements of the 1995 shifted vertex data [25] and of the data recorded in 1994 [15, 80]. In the region with $Q^2 \leq 6.5$ GeV^2 the 1994 result was obtained from the data with shifted vertex and with radiative events. The measurement with the 1995 shifted vertex data covers the Q^2 range between 0.35 and 3.5 GeV^2, extending the kinematic reach compared to the 1994 measurement by roughly a factor of 5 in Q^2. In the region of overlap the results of the three measurements are in general in very good agreement. However, in the low Q^2 region this analysis tends to yield smaller values of F_2 than the measurement with the 1995 shifted vertex data but is in good agreement with the H1 QCD fit (see fig. 5.5). At the largest values of y the measurement is dominated by the uncertainty of the photoproduction background determination. In the region of Q^2 between 2.5 GeV^2 and 6.5 GeV^2 the experimental uncertainty of the results of this analysis is reduced by up to a factor of 2 compared to previous measurements. The improvement is mainly due to a reduced uncertainty of the energy scale and of the angular measurement achieved with the new backward detector components BDC and Spacal and an increase of integrated luminosity by roughly a factor of 10 (4) compared to the 1994 (1995) measurement with the shifted vertex data respectively. With the improved precision the measurement provides a powerful constraint for further development of low Q^2 models (see section 5.4) and for the determination of the parton densities and the coupling constant α_S from QCD fits [14, 93].

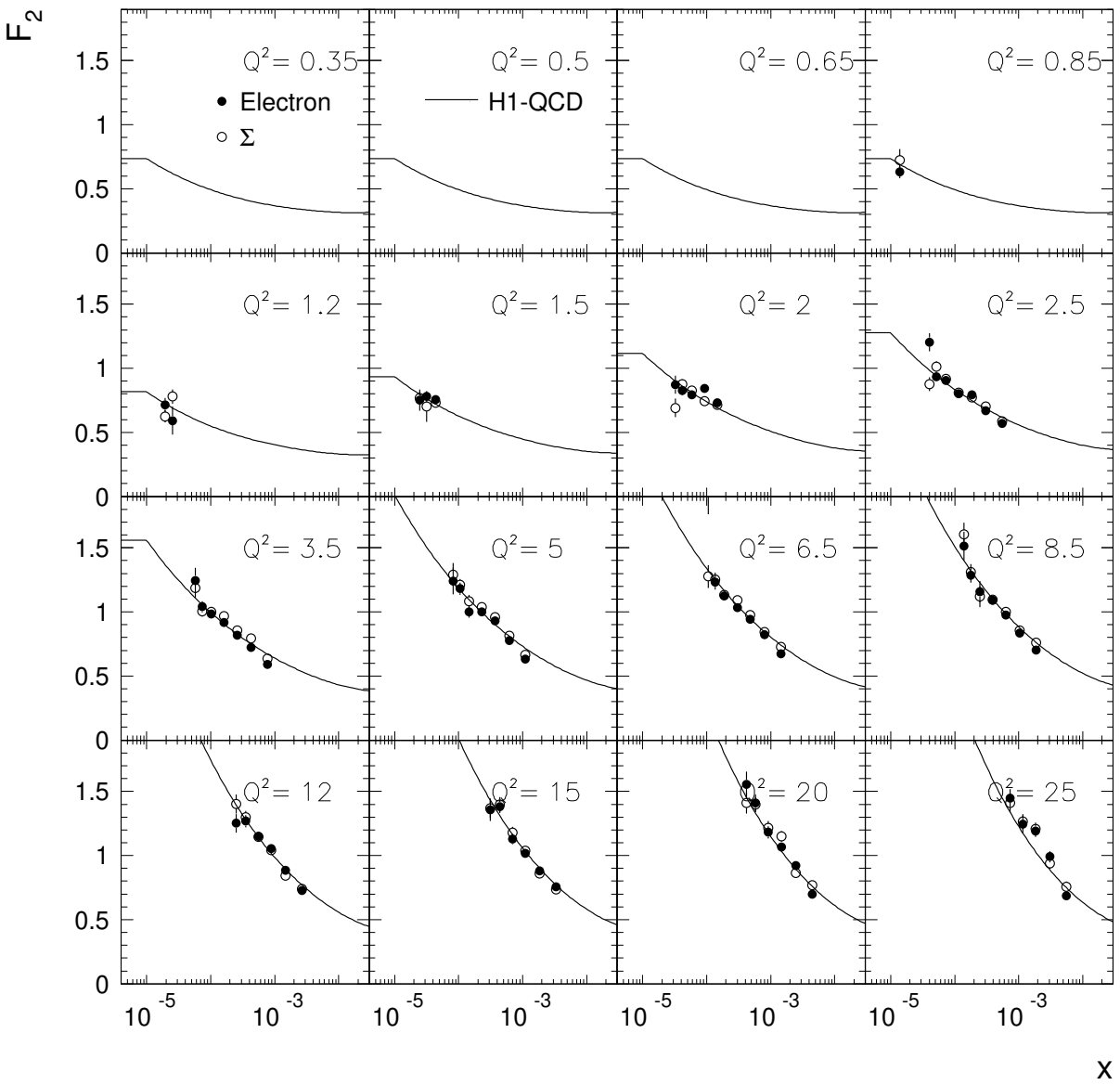

Figure 5.5: The structure function F_2 as a function of x in different bins of Q^2 measured from the nominal vertex data recorded in 1995. Compared are the results obtained with the electron method (full points) and with the Σ method (open points). The error bars represent the statistical error only. The solid line shows the H1 QCD fit [15].

Fig. 5.7 shows the ratio between the result of the present measurement and the H1 QCD fit [15]. The figure allows to directly compare the statistical and the systematic uncertainties between different bins in x and Q^2. Furthermore, it demonstrates the agreement between the present measurement and the H1 QCD fit. The precision is particularly high in the region of Q^2 between 2.5 and 8.5 GeV^2 at moderate values of x. Towards the lowest x values the uncertainty increases. This is mainly due to the uncertainty in the determination of the photoproduction background.

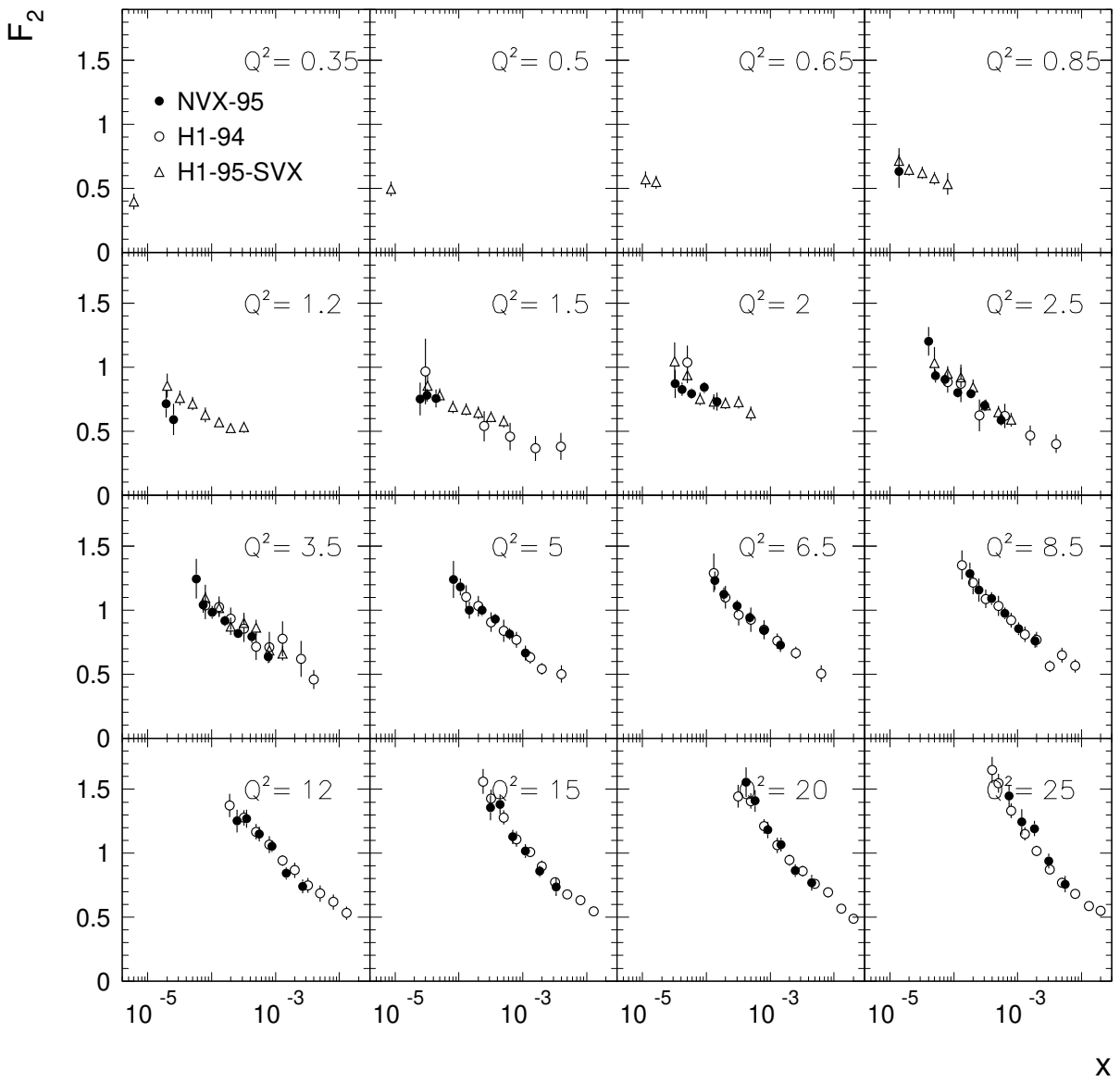

Figure 5.6: The proton structure function F_2 as a function of x in different bins of Q^2. The result of this analysis (full points) is compared with previous H1 analyses with the shifted vertex data recorded in 1995 (triangles) [25] and the nominal vertex data recorded in 1994 (open points) [15, 80]. The error bars represent statistical and systematic errors added in quadrature. A global normalization uncertainty of 1.5% is not included.

The result is tabulated in table 5.1. The proton structure function $F_2(x, Q^2)$ and the effective virtual photon proton cross section $\sigma^{\text{eff}}_{\gamma^* p}$ (see equation (1.14)) are given for the central values Q^2 and x. The corresponding values of y and W are listed also. The points with $W < 100$ GeV are obtained with the Σ method. $\sigma^{\text{eff}}_{\gamma^* p}$ is scaled by the kinematic factor $k = Q^2/(4\pi^2\alpha)$. Thus, the difference between F_2 and $k\sigma^{\text{eff}}_{\gamma^* p}$ directly demonstrates the influence of R the values of which are also listed. The values of R

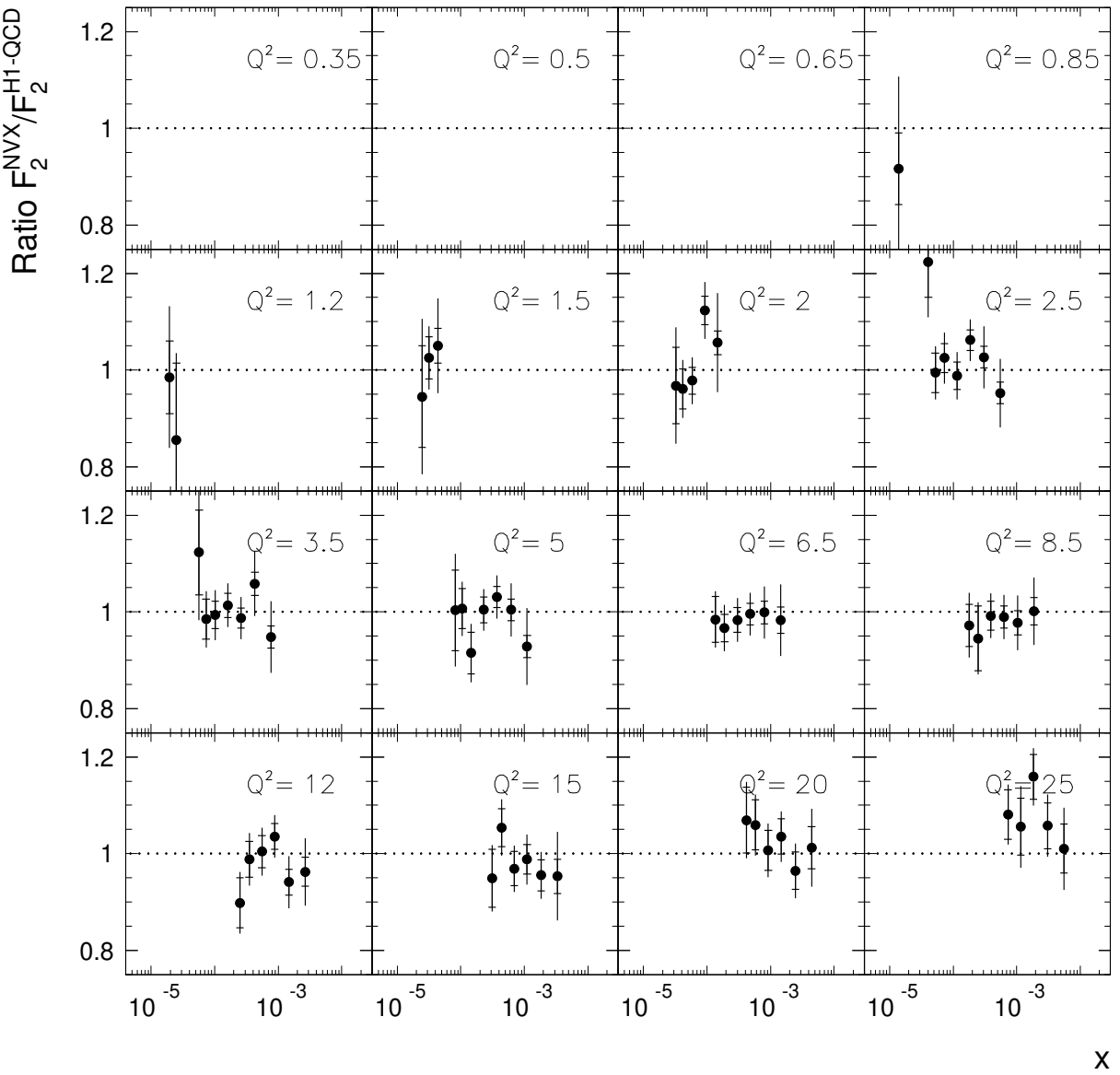

Figure 5.7: Ratio between the result of the present measurement and the H1 QCD fit [15]. The inner error bars denote the statistical uncertainty, the full error bars correspond to the systematic and the statistical errors added in quadrature.

are taken from the model given in [82]. The statistical error δ_{stat}, the uncorrelated systematic error δ_{uncor} and the total systematic error δ_{sys} are listed together with the total experimental error δ_{tot} which contains statistical and systematic errors added in quadrature. Not included in the error is the normalization uncertainty of 1.5% of the luminosity measurement (see section 5.2).

Q^2 [GeV^2]	x	y	W [GeV]	$k\sigma^{\rm eff}_{\gamma^* p}$	F_2	R	$\delta_{\rm stat}$ [%]	$\delta_{\rm uncor}$ [%]	$\delta_{\rm sys}$ [%]	$\delta_{\rm tot}$ [%]
0.85	0.000014	0.680	248	0.591	0.633	0.192	8.1	8.9	19.2	20.8
1.20	0.000025	0.530	219	0.567	0.592	0.229	18.6	8.0	9.6	20.9
1.20	0.000020	0.680	248	0.656	0.713	0.233	7.6	5.7	12.8	14.9
1.50	0.000044	0.380	185	0.741	0.756	0.248	3.4	7.2	8.7	9.3
1.50	0.000031	0.530	219	0.745	0.782	0.254	4.3	3.8	4.8	6.4
1.50	0.000024	0.680	248	0.688	0.753	0.259	11.1	5.1	12.9	17.0
2.00	0.000148	0.150	116	0.728	0.730	0.260	2.3	7.8	9.4	9.7
2.00	0.000092	0.240	147	0.835	0.841	0.267	2.6	4.3	4.5	5.2
2.00	0.000058	0.380	185	0.776	0.794	0.275	2.9	3.2	4.0	4.9
2.00	0.000042	0.530	219	0.785	0.827	0.282	4.3	3.4	4.5	6.2
2.00	0.000033	0.680	248	0.789	0.871	0.288	8.2	4.7	9.4	12.5
2.50	0.000554	0.050	67	0.588	0.588	0.264	2.3	4.6	7.0	7.4
2.50	0.000308	0.090	90	0.701	0.701	0.269	2.2	3.7	5.9	6.3
2.50	0.000185	0.150	116	0.792	0.794	0.276	2.0	3.1	3.5	4.1
2.50	0.000115	0.240	147	0.797	0.803	0.284	2.9	3.0	4.1	5.0
2.50	0.000073	0.380	185	0.884	0.905	0.293	2.9	3.1	4.3	5.2
2.50	0.000052	0.530	219	0.884	0.933	0.301	4.1	3.4	3.8	5.6
2.50	0.000041	0.680	248	1.085	1.203	0.307	6.0	3.9	7.2	9.4
3.50	0.000775	0.050	67	0.636	0.636	0.276	2.5	3.5	7.5	7.8
3.50	0.000431	0.090	90	0.793	0.794	0.284	2.3	3.5	5.9	6.3
3.50	0.000258	0.150	116	0.814	0.817	0.292	2.1	3.0	3.9	4.4
3.50	0.000161	0.240	147	0.910	0.918	0.302	2.5	3.1	3.7	4.5
3.50	0.000102	0.380	185	0.959	0.984	0.313	2.9	3.1	4.3	5.2
3.50	0.000073	0.530	219	0.982	1.041	0.321	4.2	3.5	4.1	5.9
3.50	0.000057	0.680	248	1.116	1.246	0.328	7.8	3.8	9.8	12.5
5.00	0.001107	0.050	67	0.665	0.665	0.277	2.5	3.5	8.2	8.6
5.00	0.000615	0.090	90	0.813	0.813	0.288	2.2	3.5	5.0	5.5
5.00	0.000369	0.150	116	0.926	0.929	0.299	2.1	3.0	3.8	4.3
5.00	0.000231	0.240	147	0.990	0.999	0.310	2.6	3.0	3.4	4.3
5.00	0.000145	0.380	185	0.977	1.002	0.323	4.7	3.1	4.6	6.6
5.00	0.000104	0.530	219	1.114	1.181	0.332	4.1	3.3	3.8	5.6
5.00	0.000082	0.680	248	1.109	1.240	0.340	8.3	3.9	8.1	11.6
6.50	0.001439	0.050	67	0.728	0.729	0.271	2.8	3.5	7.0	7.5
6.50	0.000800	0.090	90	0.843	0.844	0.285	2.4	3.5	4.9	5.4
6.50	0.000480	0.150	116	0.939	0.942	0.297	2.2	3.1	3.8	4.4
6.50	0.000300	0.240	147	1.024	1.033	0.310	2.7	3.0	3.8	4.6
6.50	0.000189	0.380	185	1.095	1.124	0.323	2.9	3.1	4.0	4.9
6.50	0.000136	0.530	219	1.161	1.232	0.334	4.8	3.2	3.5	5.9
8.50	0.001882	0.050	67	0.761	0.761	0.262	2.8	3.5	6.4	6.9
8.50	0.001045	0.090	90	0.853	0.854	0.277	2.5	3.5	5.3	5.8
8.50	0.000628	0.150	116	0.972	0.975	0.292	2.3	3.0	4.0	4.6
8.50	0.000392	0.240	147	1.082	1.091	0.306	3.0	3.1	3.6	4.7
8.50	0.000248	0.380	185	1.128	1.158	0.320	7.1	3.3	3.4	7.9
8.50	0.000177	0.530	219	1.213	1.286	0.331	4.5	3.6	5.3	6.9
12.00	0.002657	0.050	67	0.741	0.742	0.245	3.1	3.5	6.6	7.3
12.00	0.001476	0.090	90	0.841	0.841	0.264	2.8	3.6	5.0	5.7
12.00	0.000886	0.150	116	1.051	1.054	0.280	2.6	3.1	3.4	4.3
12.00	0.000553	0.240	147	1.141	1.150	0.295	3.3	3.2	3.7	4.9
12.00	0.000350	0.380	185	1.237	1.269	0.312	3.8	3.1	4.0	5.5
12.00	0.000251	0.530	219	1.181	1.252	0.323	5.7	3.2	4.2	7.1
15.00	0.003321	0.050	67	0.734	0.734	0.233	3.7	3.6	8.8	9.6
15.00	0.001845	0.090	90	0.859	0.859	0.253	3.4	3.5	3.8	5.1
15.00	0.001107	0.150	116	1.014	1.017	0.271	3.1	3.1	4.2	5.2
15.00	0.000692	0.240	147	1.119	1.128	0.287	3.6	3.2	3.4	5.0
15.00	0.000437	0.380	185	1.349	1.383	0.304	3.7	3.4	4.1	5.5
15.00	0.000314	0.530	219	1.281	1.356	0.316	6.3	3.1	3.5	7.2
20.00	0.004429	0.050	67	0.769	0.770	0.216	4.3	3.7	6.8	8.0
20.00	0.002460	0.090	90	0.862	0.863	0.238	4.0	4.1	4.3	5.9
20.00	0.001476	0.150	116	1.065	1.068	0.257	3.5	3.3	3.6	5.1
20.00	0.000923	0.240	147	1.172	1.181	0.274	4.1	3.3	3.6	5.5
20.00	0.000582	0.380	185	1.376	1.409	0.291	4.9	3.1	3.4	6.0
20.00	0.000418	0.530	219	1.472	1.556	0.304	6.4	3.3	3.7	7.4
25.00	0.005535	0.050	67	0.758	0.758	0.202	5.0	3.7	6.7	8.4
25.00	0.003075	0.090	90	0.939	0.939	0.225	4.5	3.5	4.1	6.1
25.00	0.001844	0.150	116	1.190	1.193	0.245	4.0	3.1	3.2	5.1
25.00	0.001154	0.240	147	1.234	1.243	0.263	5.5	5.4	5.8	8.0
25.00	0.000729	0.380	185	1.417	1.450	0.281	4.7	3.0	3.4	5.8

Table 5.1: Table of the results of the F_2 measurement using data with nominal vertex recorded in 1995. $k = Q^2/(4\pi^2\alpha)$. The experimental error $\delta_{\rm tot}$ is split into the statistical error $\delta_{\rm stat}$ and the systematic error $\delta_{\rm sys}$. The points with $W < 100$ GeV have been analyzed using the Σ method. Further details are explained in the text.

5.4 Comparison with Models

In this section the F_2 data measured with the H1 Detector that have been presented in the previous section are discussed and comparisons with results from other measurements, namely results from fixed target experiments at larger values of x and results obtained with the Beam Pipe Calorimeter (BPC) of the ZEUS collaboration are performed. Furthermore, different parametrizations and models are shown which have been proposed to predict the F_2 data in the HERA regime at small values of x. A recent review of the models can be found in [3]. Each of the three models, chosen here, represents a specific theoretical ansatz which is briefly described in the following.

- The model by Donnachie and Landshoff (DOLA) [21] has already been mentioned in chapter 1. Following a Regge type ansatz it successfully describes the energy behavior of the photoproduction data at $Q^2 = 0$ (see also fig. 1.3). The same x-behavior ($\propto x^{-\lambda}$) is assumed for all values of Q^2 below 10 GeV^2. The DOLA cross section can be interpreted as the contribution from non-perturbative processes at non-zero Q^2.

- The model of Glück, Reya and Vogt (GRV) [20] is exclusively based on perturbative QCD and the assumption that at a scale of $Q_0^2 = 0.34$ GeV^2 the parton distributions are valence-like. Valence-like means that the probability of finding a parton in the proton with a momentum fraction x vanishes towards small values of x. The dynamical behavior of the DGLAP evolution equations in NLO is used to predict the structure function F_2 at larger values of Q^2 (see also section 1.4). The model is valid in a Q^2 region with sufficiently large evolution distance from the starting scale Q_0^2. The model is compared to the data for values of Q^2 larger than 0.65 GeV^2.

- The model of Badelek and Kwiecinski (BK) [96] combines the concept of vector meson dominance [97] with perturbative QCD. Assuming a smooth transition from the perturbative to the non-perturbative regime the prediction of the structure function F_2 is parametrized as

$$F_2(x,Q^2) = F_2^{\mathrm{VMD}}(x,Q^2) + \frac{Q^2}{Q_0^2+Q^2} F_2^{\mathrm{QCD}}(\overline{x}, Q^2+Q_0^2) \tag{5.1}$$

  where $F_2^{\mathrm{VMD}}(x,Q^2)$ contains the sum of the vector meson production cross sections for the light mesons with masses $M_V^2 < Q_0^2$. Q_0^2 defines the boundary between VDM behavior and perturbative QCD. Q_0^2 is set to 1.2 GeV^2. Thus, the sum runs over the three lightest vector mesons ρ, ω and ϕ. $F_2^{\mathrm{QCD}}(\overline{x}, Q^2+Q_0^2)$ is taken from perturbative QCD models such as that of GRV at a rescaled value of $\overline{x} = (Q^2+Q_0^2)/(W^2+Q^2-M^2+Q_0^2)$. At small Q^2 the perturbative contribution is suppressed with $Q^2/(Q_0^2+Q^2)$.

Fig. 5.8 shows the F_2 data as a function of x in different bins of Q^2. In addition to the H1 data results from the fixed target experiment E665 [98] are displayed in

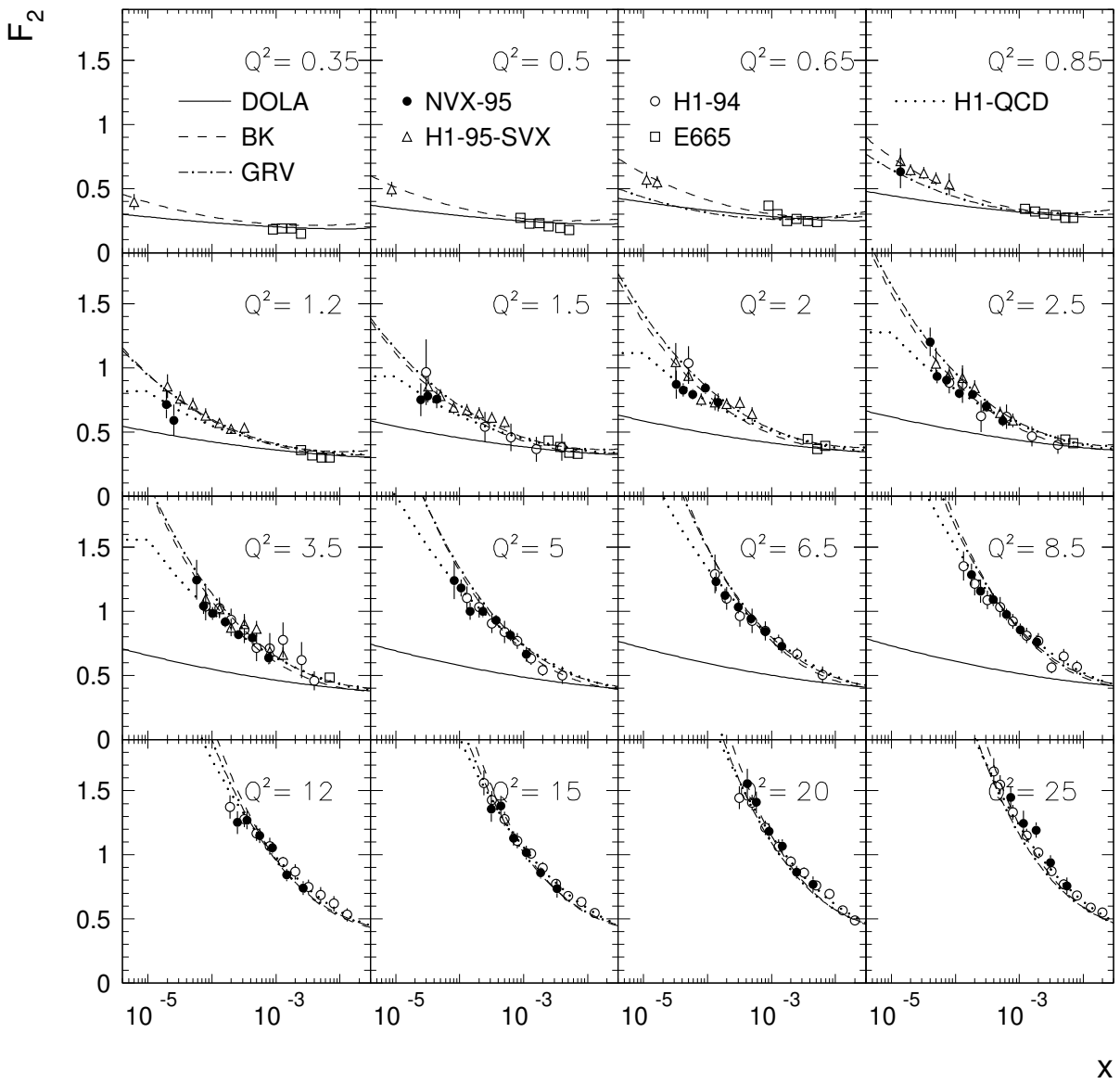

Figure 5.8: The proton structure function F_2 as a function of x in different bins of Q^2. The result of this analysis (full points) is shown together with the H1 measurements using the 1995 shifted vertex data (triangles) [25], the 1994 data (open circles) [15, 80] and results from the fixed target experiment E665 (squares) [98]. The curves represent the parametrizations by DOLA [21] (solid line), BK [96] (dashed line) and GRV [20] (dashed-dotted line) and the H1 QCD fit [15] (dotted line).

the figure. All models consistently describe the fixed target data at high values of x. However, differences arise towards small values of x. The DOLA model assumes a weak x dependence of F_2 and undershoots the HERA data in all bins of Q^2. Towards the lowest Q^2 the discrepancy becomes smaller as the x-dependence of the data weakens. The GRV model describes the data in the region with $Q^2 \gtrsim 1$ GeV^2 acceptably, showing

that in this region perturbative QCD is well applicable. Towards smaller values of Q^2 approaching the starting scale $Q_0^2 = 0.34$ GeV^2 the GRV model fails to describe the data. In this region the valence-like behavior becomes dominant, forcing F_2 to be small at small values of x.

In contrast to GRV and DOLA the BK model describes the behavior of the data reasonably well in the full kinematic range between 0.35 and 25 GeV^2. The fig. 5.8 shows that at 1 GeV$^2 \lesssim Q^2 \lesssim 8.5$ GeV^2 both GRV and BK are very similar. Both models slightly overestimate the data at the smallest values of x. Here, the parametrization obtained with the H1 QCD fit to the 1994 data [15] gives a more realistic description of the data than the model predictions. Towards values of Q^2 below 1 GeV^2 the GRV model is seen to deviate from the data while the BK model continues to give a reasonable description. In this region in the BK model the contribution from perturbative QCD to the cross section decreases and the VDM component becomes dominant. The comparison of the models with the data suggests that, at the present level of theoretical understanding and experimental precision, the onset of the transition region to the non-perturbative regime can be localized in the region of $Q^2 \sim 1$ GeV^2.

In order to allow a direct comparison of the DIS data with photoproduction measurements at $Q^2 = 0$ the F_2 results are expressed as a total virtual photon proton cross section $\sigma^{\mathrm{tot}}_{\gamma^* p}$ according to equation (1.17). Fig. 5.9 shows the behavior of $\sigma^{\mathrm{tot}}_{\gamma^* p}$ as a function of W in different bins of Q^2. The low energy data and the data from the ZEUS Beam Pipe Calorimeter (BPC) [28] are given by the authors at slightly different Q^2 values. For the direct comparison the results are propagated to the values indicated in the fig. 5.9 using the phenomenological parametrization of Abramowicz, Levin, Levy and Maor (ALLM) [99] which has been designed to describe all HERA data including the photoproduction measurements. The fig. 5.9 illustrates the increased kinematic reach achieved with the new low-Q^2 data which essentially cover the gap between the former DIS data (at $Q^2 \geq 1.5$ GeV^2) and the photoproduction measurements (compare with fig. 1.3). The slope of the cross section decreases in a continuous way as the photoproduction limit at $Q^2 = 0$ is approached, corresponding to the flattening of the x dependence of F_2. In the fig. 5.9 the same model predictions as in the previous fig. 5.8 are compared with the data. In addition, comparisons of the BK model and the DOLA model with the photoproduction measurements at $Q^2 = 0$ are performed. The BK model, describing the data with $Q^2 \geq 0.35$ GeV^2, is seen to overshoot the data in the photoproduction limit while the DOLA model which underestimates the data with $Q^2 \geq 0.35$ GeV^2 is in perfect agreement with the data at $Q^2 = 0$.

The Q^2 dependence of the data is investigated in fig. 5.10 showing the effective virtual photon proton cross section $\sigma^{\mathrm{eff}}_{\gamma^* p}$ as given in equation (1.15) in different bins of W. All data are corrected to the W values given in the figure using the ALLM parametrization. Also shown are the photoproduction data at $Q^2 = 0$ and the measurement made with the ZEUS BPC which covers the Q^2 range between 0.11 and 0.65 GeV^2. As already seen in the previous fig. 5.9 the BK model does not describe the data in the photoproduction limit but predicts a cross section which is too large by roughly 30%. In comparison,

the DOLA model undershoots all data with non-zero Q^2 while at $Q^2 = 0$ it describes the data well. The BPC points with 0.11 and 0.65 GeV^2 appear to lie between the two model predictions.

The difference of the nature of scattering processes in the DIS regime – governed by perturbative QCD – and photoproduction – as described by Regge type parametrizations – can be illustrated particularly well when considering the behavior of the total virtual photon proton cross section $\sigma^{\mathrm{tot}}_{\gamma^* p}$ scaled with Q^2 as a function of Q^2 (shown in fig. 5.11). According to equation (1.17) $\sigma^{\mathrm{tot}}_{\gamma^* p} \cdot Q^2 = 4\pi^2\alpha \cdot F_2$. At sufficiently large Q^2 the structure function F_2 is scale invariant, i.e. to first order constant with Q^2, and only depends on x (see chapter 1). In the region of scale invariance the proton appears as composed of point like free partons. At small Q^2 scale invariance breaks down. Here the strong coupling constant α_S becomes large and non-perturbative effects become dominant. In the limit of $Q^2 \to 0$ F_2, and thus $\sigma^{\mathrm{tot}}_{\gamma^* p} \cdot Q^2$, decreases as Q^2. Fig. 5.11 shows the scaled cross section as a function of Q^2. The photoproduction data are plotted at an arbitrarily chosen Q^2 value of 0.0014 GeV^2. In the region of $Q^2 \gtrsim 1$ GeV^2 the scaled cross section is, to first order, independent of Q^2 and only depends on W. In this region QCD perturbation theory holds, as explained above. Towards smaller Q^2 the scaling of the cross section breaks down. In this region non-perturbative effects become dominant.

In summary, the data have been compared to three qualitatively different models. The GRV model, representing perturbative QCD, describes the data at Q^2 values above ~ 1 GeV^2. The DOLA model, based on Regge theory, correctly describes the photoproduction cross section at $Q^2 = 0$. However, it fails to reproduce the data in the DIS region with non-zero Q^2. The BK model, assuming a smooth transition between the perturbative and non-perturbative regime does describe the DIS data but is not correct in the photoproduction limit where it grossly overestimates the cross section. In conclusion, presently, no model describes the data in the full kinematic range including the photoproduction measurements[2].

[2] After this thesis was completed a parametrization was published [100] which, based on the generalized vector dominance model, appears to describe all HERA data between $Q^2 = 0$ and $Q^2 \lesssim 350$ GeV^2.

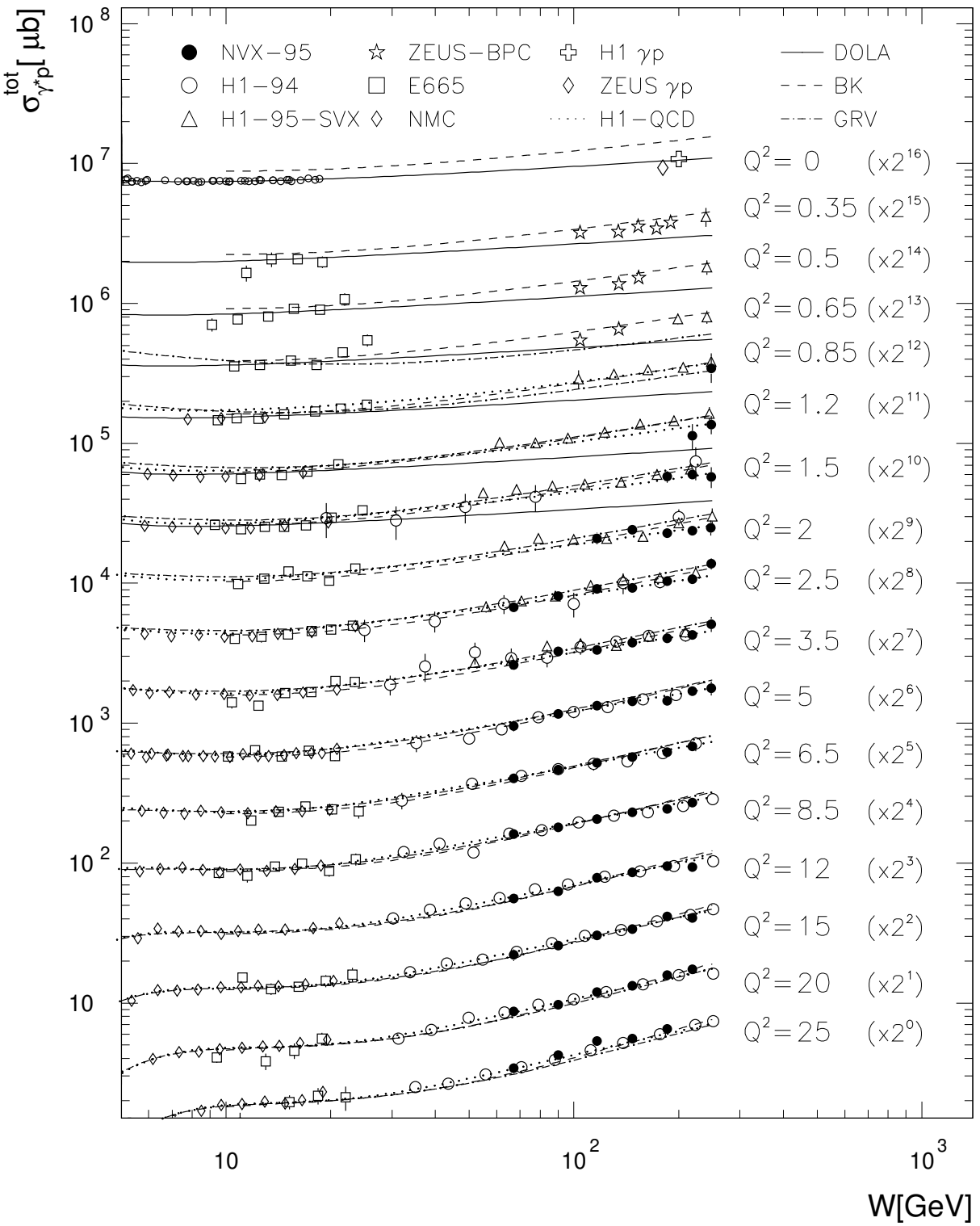

Figure 5.9: The total photon proton cross section $\sigma^{\rm tot}_{\gamma^* p}$ as a function of W in different bins of Q^2. The cross sections are multiplied with the factors indicated in the figure. The results of this analysis are shown by full points. Open points (triangles) refer to results by the H1 Collaboration with the 1994 (1995 shifted vertex) data respectively. Also shown are results from E665 (squares) [98] and NMC (diamonds) [18] as well as the measurements of the total γp cross section by the Collaborations H1 (cross) [23] and ZEUS (diamond) [24]. The data measured with the ZEUS Beam Pipe Calorimeter (BPC) [28] are shown by stars. The curves represent the models by DOLA (solid line), BK (dashed line) and GRV (dashed-dotted line) and the H1 QCD fit (dotted line).

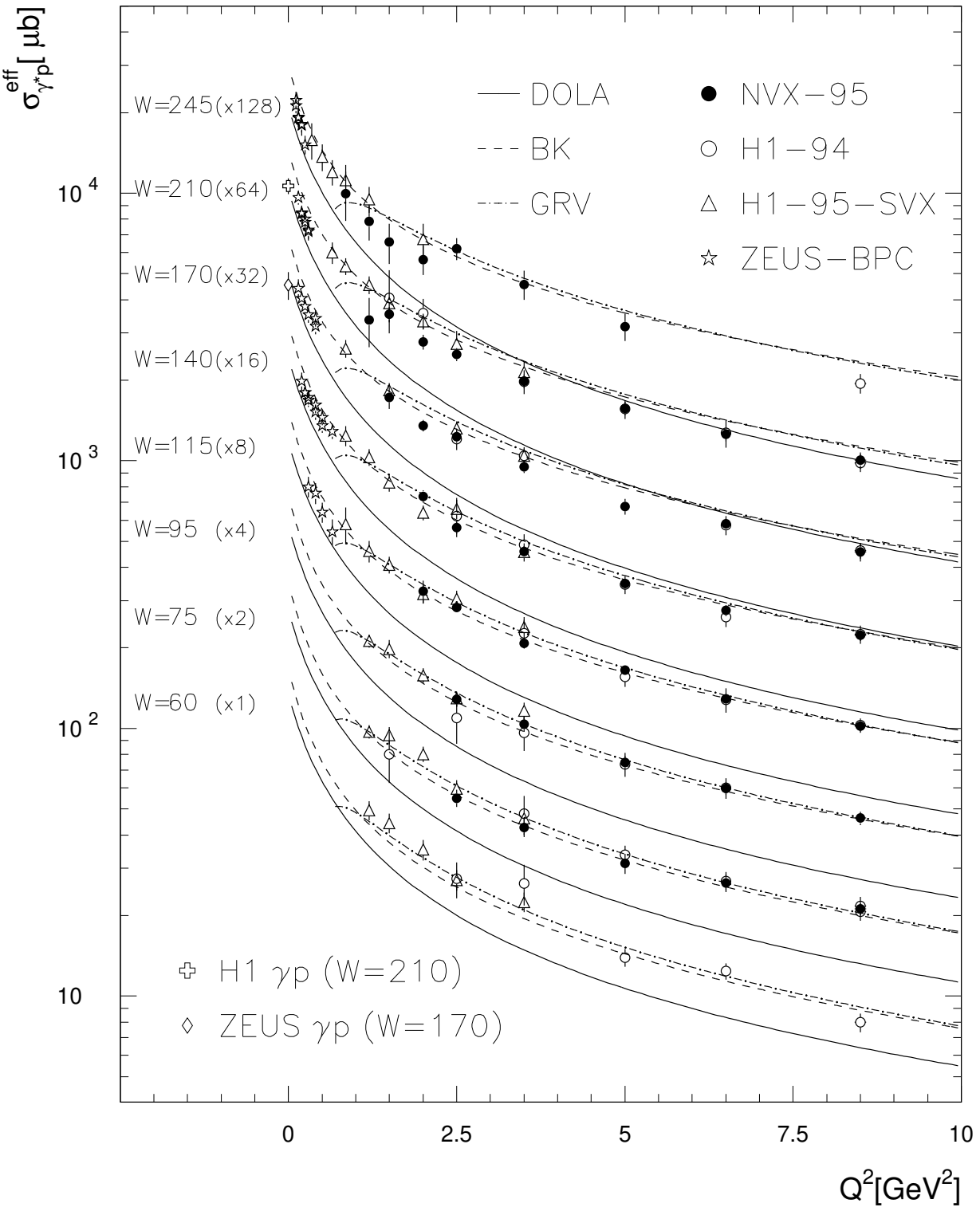

Figure 5.10: The effective photon proton cross section $\sigma^{\rm eff}_{\gamma^* p}$ as a function of Q^2 in different bins of W. Also shown are the photoproduction results at $W = 170$ GeV by the ZEUS Collaboration (diamond) and at $W = 210$ GeV by the H1 Collaboration (cross). The ZEUS BPC data points are also depicted (stars). The curves refer to the models DOLA (solid), BK (dashed) and GRV (dashed-dotted).

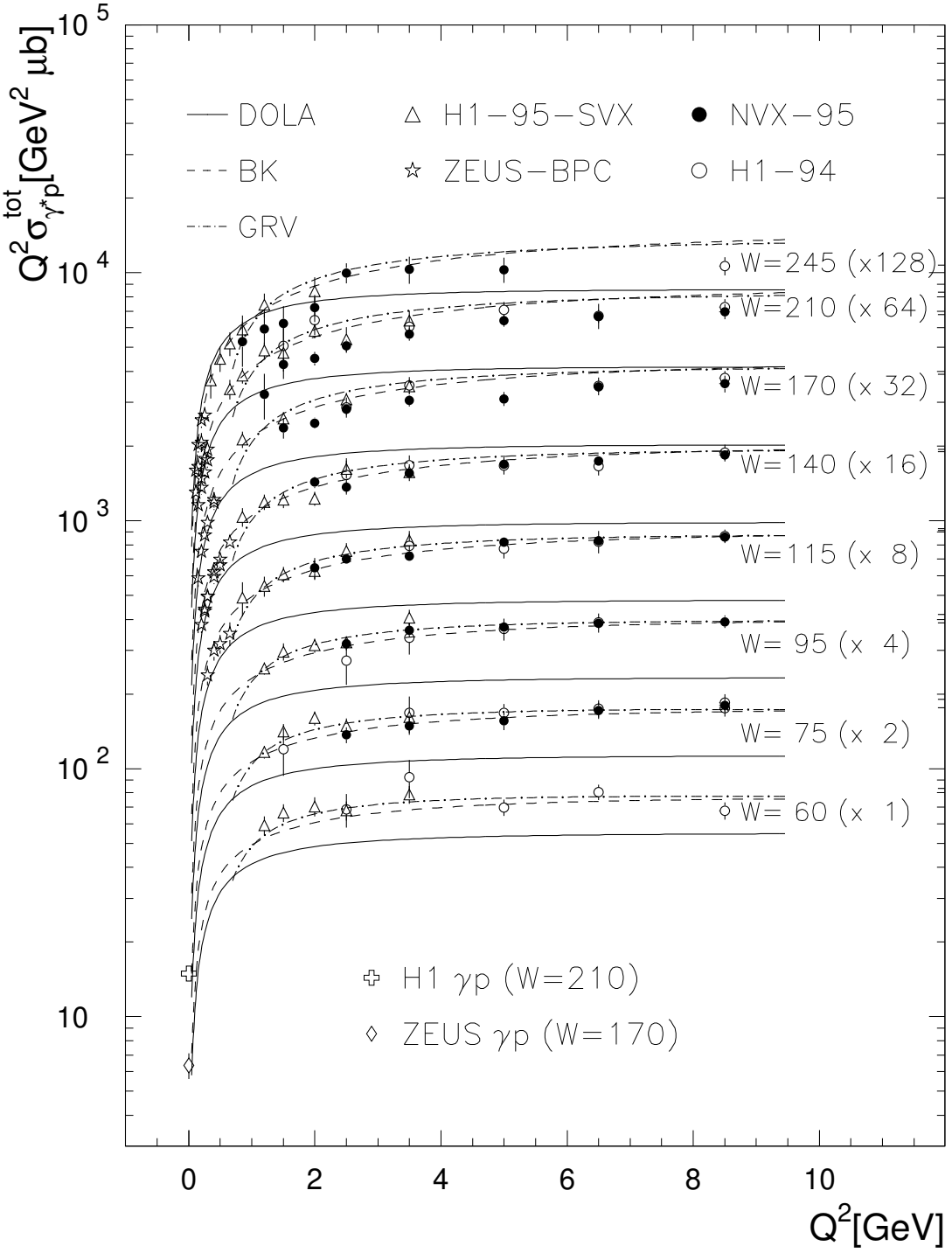

Figure 5.11: The total photon proton cross section $\sigma^{\rm tot}_{\gamma^* p}$ scaled with Q^2 as a function of Q^2 in different bins of W. Also shown are the photoproduction results by H1 (cross) [23] and ZEUS (diamond) [24] and the ZEUS BPC data points (stars) [28]. The curves refer to the models DOLA (solid), BK (dashed) and GRV (dashed-dotted).

Summary

A measurement has been presented of the proton structure function $F_2(x, Q^2)$ in the Q^2 region between 0.85 and 25 GeV^2. The analysis uses data recorded with the H1 detector in 1995, the commissioning year of the new backward detector components Spacal and BDC. In the region of Q^2 between 2.5 and 6.5 GeV^2 the experimental uncertainty is reduced compared to previous measurements by roughly a factor of 2.

The energy calibration of the new Spacal calorimeter is described in detail. The electromagnetic energy scale is determined from scattered electrons using two independent methods. The resulting uncertainty on the electromagnetic energy scale of the Spacal is estimated to be less than 0.7%. An energy resolution of 3% is found for electrons with an energy of 27.5 GeV as compared to the Spacal design value of 2%. The absolute energy scale for the measurement of the hadronic final state in the Spacal is determined to a precision of 7%. It is expected that these values can be improved further using future data.

The event selection criteria used for the measurement of the structure function F_2 are presented. The behavior of each cut is investigated in detail comparing the data with Monte Carlo simulations. Discrepancies are detected in particular in the description of the development of electromagnetic showers in the Spacal and of the dead material in front of the BDC. Problems also arise in the region of very low $y < 0.05$ where the Monte Carlo simulation does not reproduce the vertex reconstruction efficiency measured in the data. The sources of the discrepancies as well as the impact on the measurement of F_2 are discussed. Corrections are introduced where possible.

A detailed study of the photoproduction background is performed comparing the data with PHOJET Monte Carlo simulations. It is found that the PHOJET simulation presently available considerably underestimates the photoproduction background in DIS events at small values of $Q^2 \lesssim 4$ GeV^2. A set of corrections is applied in order to reduce the influence on the result of F_2. The uncertainty on the background determination is estimated to be 30%.

A first investigation of events with QED Final State Radiation in the Spacal shows that the DJANGO Monte Carlo reproduces the data well within the present experimental uncertainties.

The structure function F_2 is measured using two different methods to reconstruct the kinematic variables x and Q^2, namely the electron and the Σ method. The results

obtained with the two systematically different methods are in good agreement with each other and with the H1 QCD fit to previous data.

The results of the present analysis are compared to previous H1 measurements, to fixed target data as well as data obtained with the Beam Pipe Calorimeter of the ZEUS Collaboration, showing good overall agreement. The strong rise of F_2 with decreasing x observed in the previous HERA measurements is seen to flatten towards the smallest values of Q^2 ($\gtrsim$ 0.35 GeV^2) but is still significant.

Finally, comparisons of the F_2 data with model predictions and with photoproduction measurements are made. It is demonstrated that perturbative QCD (as represented by the GRV model) describes the data with $Q^2 \gtrsim 1$ GeV^2 but fails towards lower values of Q^2. A Regge type parametrization by Donnachie and Landshoff agrees with the photoproduction data but does not succeed to describe the data with $Q^2 > 0$. A model by Badelek and Kwiecinski, combining perturbative and non-perturbative approaches, describes all F_2 data presently available. However, it fails to describe the data in the photoproduction limit of $Q^2 = 0$. In conclusion, presently, no model describes the HERA data in the complete kinematic range[3].

[3] After this thesis was completed a parametrization was published [100] which, based on the generalized vector dominance model, appears to describe all HERA data between $Q^2 = 0$ and $Q^2 \lesssim 350\,\mathrm{GeV}^2$.

Bibliography

[1] J. D. Bjorken, Phys. Rev. **148** (1966) 1467;
J. D. Bjorken, Phys. Rev. **179** (1969) 1547.

[2] J. D. Bjorken, E. A. Paschos, Phys. Rev. **185** (1969) 1975.

[3] A. Levy, *Proceedings of the Workshop on Deep Inelastic Scattering*, Rome 1996, Eds. A. Negri and G. D'Agostini, Tel-Aviv preprint TAUP-2349-96 (1996);
A. Levy, DESY preprint 97-013 (1997).

[4] R.G. Roberts, *The Structure of the Proton*, Cambridge University Press 1990.

[5] L. N. Hand, Phys. Rev. **129** (1963) 1834.

[6] F. Halzen, A.D. Martin, *Quarks and Leptons*, Wiley 1984;
CTEQ Coll., R. Brock, et al, *Handbook of perturbative QCD*, FERMILAB-PUB-94-316, Sep 1994, submitted to Rev. Mod. Phys.

[7] Review of Particle Properties, Phys. Rev. **D 54** (1996) 77.

[8] G. Altarelli, *Partons in Quantum Chromodynamics*, Phys. Rep. **81 C**, (1982) 1.

[9] V. N. Gribov and L. N. Lipatov, Sov. J. Nucl. Phys. **15** (1972) 438;
L. N. Lipatov, Sov. J. Nucl. Phys. **20** (1975) 96.

[10] G. Altarelli and G. Parisi, Nucl. Phys. **B126** (1977) 298.

[11] Y. J. Dokshitzer, Sov. Phys. JETP **46** (1977) 641.

[12] Y. Balitzki, L.N. Lipatov, Phys. Rev. Lett. **28** (1978) 822;
E.A. Kuraev, L.N. Lipatov, V.S. Fadin, Phys. Rev. Lett. **44** (1976) 443 and Phys. Rev. Lett. **45** (1077) 199.

[13] M. Froissart, Phys. Rev. **123** (1961) 1053.

[14] M. Botje, M. Klein, C. Pascaud, *Proceedings of the Workshop on HERA Physics 1995/1996*, eds. G. Ingelman, A. De Roeck and R. Klanner, DESY preprint 96-198.

[15] H1 Coll., S. Aid et al, Nucl. Phys. **B 470** (1996) 3.

[16] ZEUS Coll., M. Derrick et al, Z. Phys. **C 72** (1996) 399.

[17] BCDMS Coll., A.C. Benvenuti et al, Phys. Lett. **B 223** (1989) 485, CERN preprint CERN-EP/89-06.

[18] NMC Coll., M. Arneodo et al, Phys. Lett. **B 364** (1995) 107;
NMC Coll., M. Arneodo et al, Nucl. Phys. **B 483** (1997) 3.

[19] C. Pascaud, F. Zomer, DESY preprint 96-266, Nov 1996.

[20] M. Glück, E. Reya and A. Vogt, Z. Phys. **C 67** (1995) 433.

[21] A. Donnachie and P. V. Landshoff, Z. Phys. **C 61** (1994) 139.

[22] P.D.B. Collins, A.D. Martin, *Hadron Interactions*, Adam Hilger, 1984.

[23] H1 Coll., T. Aid et al, Z. Phys. **C 69** (1995) 27.

[24] ZEUS Coll., M. Derrick et al, Z. Phys. **C 63** (1994) 408.

[25] H1 Coll., C. Adloff et al, Nucl. Phys. **B 497** (1997) 3.

[26] R. Barschke, Ph.D. Thesis (in German), Hamburg 1997, in preparation.

[27] J. Katzy, Ph.D. Thesis (in German), Heidelberg 1997.

[28] ZEUS Coll., J. Breitweg et al, DESY preprint 97-135, 1997.

[29] B.H. Wiik, *Proceedings of the HERA Workshop*, vol.1, eds. W. Buchmüller and G. Ingelman, Hamburg 1991.

[30] H1 Coll., I. Abt et al, Nucl. Instr. and Meth. **A 386** (1997) 310 and **A 386** (1997) 348.

[31] J. Gayler , Minutes of H1 ESCALE meeting, 5. 2. 1996.

[32] H1 Coll., PRC report 93/02 March 8, 1993.

[33] B. Schwab, Ph.D. Thesis (in German), Heidelberg 1996.

[34] H. Bethe, W. Heitler; Proc. Roy. Soc. **A 146** (1934) 83.

[35] H1 Coll., *Proceedings of the International Conference on High Energy Physics*, Warsaw 1996, ICHEP96-pa17-026;
N. Gogitidze, S. Levonian, Internal Note H1 - 02/96-471 (1996).

[36] R. Wallny, Diploma Thesis (in German), Heidelberg 1996.

[37] F. Sefkow, E. Elsen, H. Krehbiel, U. Straumann, Internal Note H1 - 11/94-407 (1994).

[38] H1 Spacal Group, Nucl. Instrum. Meth. **A 386** (1997) 397.

[39] H1 Spacal Group, Nucl. Instrum. Meth. **A 382** (1996) 395.

[40] S. Tapprogge, *Proceedings of the Workshop on Deep Inelastic Scattering*, Chicago 1997, eds. J. Repond and D. Krakauer, to be published.

[41] R. Poeschl, Private Communication.

[42] H1 Spacal Group, Nucl. Instr. Meth. **A 374** (1996) 149.

[43] R. Barschke, A. Walther, Proceedings of SCIFI93 workshop 1993.

[44] H1 Spacal Group, R.D. Appuhn, et al, DESY preprint 97-070 (1997) , submitted to Nucl. Instr. and Methods.

[45] H1 Spacal Group, T. Nicholls et al, DESY preprint 96-013 (1996).

[46] S. Spielmann, Ph.D. Thesis (in French), Paris 1996.

[47] H1 Spacal Group, T. Nicholls et al, "Electronics for the H1 Spacal Detector", in preparation.

[48] E. Eisenhandler et al, IEEE Transactions on Nuclear Science, 42 (1995) 688.

[49] S. Schleif, H1 Software Note 56, March 1996.

[50] J. Janoth, Ph.D. Thesis (in German), Heidelberg 1997.

[51] R. Poeschl, Diploma thesis (in German), Dortmund 1996.

[52] C. Pfeiffer, M. Dirkmann, Internal Note H1 - 01/97-512 (1997).

[53] S. Bentvelsen, J. Engelen, P. Kooijman, vol.1, p23, M. Klein, vol.1, p71, *Proceedings of the HERA Workshop*, eds. W. Buchmüller and G. Ingelman, Hamburg 1991.

[54] U. Bassler and G. Bernardi, Nucl. Instr. and Meth. **A 361** (1995) 197.

[55] F. Jaquet, A. Blondel, *Proceedings of the Study of an ep Facility for Europe* , vol.1, p391 ed. U. Amaldi, DESY 79/48, Hamburg 1979.

[56] H1 Coll., S. Abt et al, DESY preprint 93-103 (1993).

[57] R. Brun et al, GEANT3 User's Guide, CERN-DD/EE 84-1, Geneva (1987).

[58] G.A. Schuler, H. Spiesberger, *Proceedings of the Workshop Physics at HERA*, eds. W. Buchmüller and G. Ingelman, vol.3, DESY (1992).

[59] R. Engel and J. Ranft, Phys. Rev. **D 54** (1996) 4244.

[60] A. Kwiatkowski, H. Spiesberger and H.-J. Möhring, Comp. Phys. Comm. **69** (1992) 155.

[61] G. Ingelman, *Proceedings of the Workshop 'Physics at HERA'*, vol. 3, Eds. W. Buchmüller and G. Ingelman, DESY (1992) 1336.

[62] H. Plothow-Besch, User's Manual, CERN W5051.

[63] L. Lönnblad, Comp. Phys. Comm. **71** (1992) 15.

[64] H1 Coll., I. Abt et al, Z. Phys. **C59** (1994) 377.

[65] T. Sjöstrand and M. Bengtsson, Comp. Phys. Comm. **43** (1987) 367;
M. Bengtsson and T. Sjöstrand, Comp. Phys. Comm. **46** (1987) 43;
T. Sjöstrand, CERN-TH-6488 (1992).

[66] H. Jung, Comp. Phys. Comm. **86** (1995) 147.

[67] A. D. Martin, W. J. Stirling, and R. G. Roberts, Phys. Lett. **B 306** (1993) 145; **B 309** (1993) 492.

[68] M. Erdmann, DESY preprint 96-090, May 1996.

[69] I. Abt, Manual to IJRAY, Internal Note H1 - 05/93-290 (1993).

[70] H1 Coll., C. Adloff et al, Z. Phys. **C 69** (1995) 27.

[71] A. Meyer, Internal Note H1 - 08/96-486 (1996).

[72] M. Dirkmann, Internal Note H1 - 05/96-477 (1996).

[73] C. Arndt, Diploma Thesis (in German), Hamburg 1995.

[74] C. Müller, Diploma Thesis (in German), Heidelberg 1997.

[75] P. Verrecchia, Internal Note H1 - 09/95-456 (1995).

[76] J. Janoth, J. Stiewe, A. Meyer, Internal Note H1 - 11/95-464 (1995).

[77] H1 Spacal Group, T. Nicholls et al, Nucl. Instrum. Meth. A 374 (1995) 149.

[78] R. Maracek, Ph.D. Thesis, Kosice 1997.

[79] A. Zhokin, V. Efremenko, Minutes of ELAN DESY Group Meeting, 28.7.1995.

[80] H1 Coll., C. Adloff et al, Phys. Lett. **B 393** (1997) 452.

[81] G. Altarelli and G. Martinelli, Phys. Lett. **B 76** (1978) 89.

[82] B. Badelek, J. Kwiecinski and A. Stasto, Durham preprint DTP-96-16 (1996).

[83] S. Schleif, Minutes of Spacal meeting, 16.10.1995.

[84] ZEUS Coll., M. Derrick et al, Phys. Lett. **B 315** (1993) 481;
H1 Coll., T.Ahmed et al, Nucl. Phys. **B 429** (1994) 477.

[85] V. Shekelyan, Minutes of H1 ELAN meeting, 21.1.1997.

[86] A. Zhokin, Minutes of H1 ELAN meeting, 20.5.1997.

[87] P. Billoir, Comp. Phys. Comm. **57** (1989) 390.

[88] A. Panitch, Ph.D. Thesis, Bruxelles 1996.

[89] H1 Coll., C. Adloff et al, Z. Phys. **C 74** (1997) 221.

[90] H. Spiesberger et al, p.798 *Proceedings of the HERA Workshop*, Hamburg 1991.

[91] H1 Coll., T. Ahmed et al, Z. Phys. **C 66** (1995) 529.

[92] A. Arbuzov et al, Comp. Phys. Comm. **94** (1996) 128.

[93] F. Lehner, Ph.D. Thesis (in German), Hamburg 1997, in preparation.

[94] D.Yu. Bardin et al, *Proceedings of the Workshop on HERA Physics 1995/1996*, ed. by G. Ingelman, A. De Roeck and R. Klanner, vol.1, DESY preprint 96-198.

[95] U. Obrock, Ph.D. Thesis (in German), Dortmund 1994.

[96] B. Badelek, J. Kwiecinski, Phys. Lett. **B 295** (1992) 263.

[97] J.J. Sakurai and D. Schildknecht, Phys. Lett. **40 B** (1972) 121.

[98] E665 Coll., M. R. Adams et al, Phys. Rev. **D 54** (1996) 3006.

[99] H. Abramowicz, E.M. Levin, A. Levy and U. Maor, Phys. Lett. **B 269** (1991) 465.

[100] D. Schildknecht, H. Spiesberger, BI-TP 97/25, hep-ph/9707447, Bielefeld, July 1997.

Acknowledgments

I would like to acknowledge the stimulating interest and motivation I have received from many of my colleagues during the time in the H1 Collaboration.

The work in the SPACAL group has been a rich and unique experience especially during the commissioning year 1995. In particular I want to thank Herb Steiner for his encouragement and great support during this time.

The ELAN Group has been the framework for many fruitful discussions concerning the physics topics and data analysis and I am indebted to many of my colleagues. Special thanks go to Vladimir Shekelyan. Thanks also to R. Barschke, U. Bassler, G. Bernardi, J. Gayler, J. Katzy and F. Lehner. This work would not have been possible without their substantial contributions.

Finally, I would like to thank Prof. Naroska for her reliable advice and support throughout my entire time at DESY.